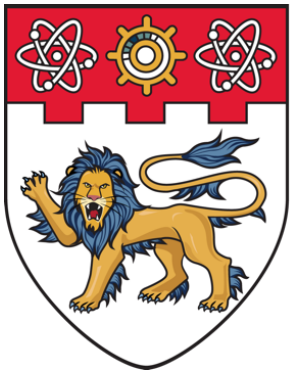

NANYANG TECHNOLOGICAL UNIVERSITY

SINGAPORE

BISMUTH HALIDE SEMICONDUCTORS – A COMBINED THEORETICAL AND EXPERIMENTAL APPROACH FOR PHOTOVOLTAICS

BIPLAB GHOSH

Interdisciplinary Graduate School

Energy Research Institute @ NTU (ERI@N)

2019

BISMUTH HALIDE SEMICONDUCTORS – A COMBINED THEORETICAL AND EXPERIMENTAL APPROACH FOR PHOTOVOLTAICS

BIPLAB GHOSH

INTERDISCIPLINARY GRADUATE SCHOOL

A thesis submitted to the Nanyang Technological University in partial fulfilment of the requirement for the degree of

Doctor of Philosophy

2019

Statement of Originality

I hereby certify that the work embodied in this thesis is the result of original research and has not been submitted for a higher degree to any other University or Institution.

23/01/2019 . . . . . .

(Date) Biplab Ghosh

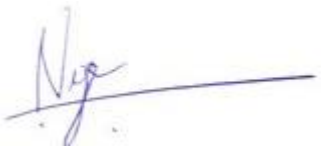

Supervisor Declaration Statement

I have reviewed the content and presentation style of this thesis and declare it is free of plagiarism and of sufficient grammatical clarity to be examined. To the best of my knowledge, the research and writing are those of the candidate except as acknowledged in the Author Attribution Statement. I confirm that the investigations were conducted in accord with the ethics policies and integrity standards of Nanyang Technological University and that the research data are presented honestly and without prejudice.

. . . 23/01/2019. . . . .

(Date)   A/Prof. Nripan Mathews

Authorship Attribution Statement

This thesis contains material from papers published in the following peer-reviewed journals where I was the first author.

Chapter 4 is published as Biplab Ghosh, Bo Wu, Hemant Kumar Mulmudi, Claude Guet, Klaus Weber, Tze Chien Sum, Subodh G. Mhaisalkar, and Nripan Mathews. Limitations of $Cs_3Bi_2I_9$ as lead-free photovoltaic absorber materials. *ACS Applied Materials and Interfaces* 10(41), 35000-35007 (2018). DOI: 10.1021/acsami.7b14735.

The contributions of the co-authors are as follows:

- A/Prof NM provided the initial project direction and edited the manuscript drafts.
- I prepared the manuscript drafts. The manuscript was revised by all the co-authors.
- I co-designed the study with A/Prof NM, Dr. HKM, Prof CG, Prof SGM, and performed all the laboratory work at the Energy Research Institute @ NTU (ERI@N). I also analyzed the data.
- CL characterizations was performed by Dr. HKM, and he, and Prof. KW assisted in the interpretation of the data
- All microscopy, X-ray characterizations, device fabrications, including sample preparation were conducted by me in the Energy Research Institute @ NTU (ERI@N)
- Dr BW performed the PL and TA spectroscopic characterization and he and Prof TCS assisted me in the interpretation of the data.

First part of the Chapter 5 is published as Biplab Ghosh, Sudip Chakraborty, Hao Wei, Claude Guet, Shuzhou Li, Subodh Mhaisalkar, and Nripan Mathews. Poor Photovoltaic Performance of $Cs_3Bi_2I_9$: An Insight through First-Principles Calculations. *Journal of Physical Chemistry C* 121(32), 17062-17067 (2017). DOI: 10.1021/acs.jpcc.7b03501.

The contributions of the co-authors are as follows:

- A/Prof NM provided the initial project direction and edited the manuscript drafts.
- I prepared the manuscript draft and the manuscript was revised by all the co-authors.
- I co-designed the study with A/Prof NM, Prof CG, and Prof SGM
- I performed all the calculations at High Performance Computing (HPC) center (NTU) and analyzed the data.
- Dr. HW and Prof SL provided the license and training for VASP and assisted in the interpretation of the data

Part of Chapter 6 is published as Biplab Ghosh, Bo Wu, Guo Xintong, Padinhare C. Harikesh, Rohit Abraham John, Tom Baikie, Arramel, Andrew T. S. Wee, Claude Guet, Tze Chien Sum, Subodh Mhaisalkar, and Nripan Mathews. Superior performance of Silver Bismuth Iodide photovoltaics fabricated via dynamic hot-casting method under ambient conditions. *Advanced Energy Materials* (2019) 8, 1802051. DOI:10.1002/aenm.201802051

The contributions of the co-authors are as follows:

- A/Prof NM provided the initial project direction and edited the manuscript drafts.
- I prepared the manuscript drafts. The manuscript was revised by all the co-authors.
- I co-designed the study with A/Prof NM, GX, PCH, RAJ, Prof SGM,

Prof. CG, and performed all the laboratory work at the Energy Research Institute @ NTU (ERI@N). I also analyzed the data.

- UPS measurement was performed by Dr. Arramel, and he, and Prof. ATSW assisted in the interpretation of the data
- All microscopy, X-ray characterizations, device fabrications, including sample preparation were conducted by me in the Energy Research Institute @ NTU (ERI@N)
- Dr. TB assisted in analysis of the XRD data.
- Dr BW performed the PL and TA spectroscopic characterization and he and Prof TCS assisted me in the interpretation of the data.

23/01/2019 . . . . . .

(Date) Biplab Ghosh

Abstract

Lead-free halide perovskites have received huge interests lately following the unparalleled success of $MAPbI_3$ in photovoltaics. The non-toxic bismuth-based halide perovskites, which offer good ambient stability compared to Pb-based halide perovskites, remain one of the key areas for the development of lead-free absorber materials. Like Pb-based halide perovskites, Bi-based perovskites also exhibit rich structural varieties and tunable optoelectronic properties. Among various Bi-based perovskites, $Cs_3Bi_2I_9$ was selected for detailed investigations as it shows good atmospheric stability and reasonable optical bandgap for a single-junction solar cell. However, the photovoltaic performance of $Cs_3Bi_2I_9$ was found to be poor, limited by low photocurrent density. To comprehend this unusually poor performance, we carried out in-depth photophysical investigations on $Cs_3Bi_2I_9$ combined with ab-initio calculations. A comparative photoluminescence spectroscopic study between thin-films and single crystals revealed the presence of defects that act as non-radiative recombination centres. This is further supported by the first principle calculations. Based on our theoretical calculations, we demonstrated that synthesizing $Cs_3Bi_2I_9$ in excess BiI_3 environment could passivate some of the defects, resulting in improved of power conversion efficiencies. Nonetheless, further investigations on photophysical properties show that the photovoltaic (PV) performance is not limited by only free carrier generation, but also on the inefficient extraction of carriers. Due to the zero-dimensional crystal structure, as opposed to the three-dimensional (3D) network of lead-based halide perovskites, the extraction of long-lived free carriers is found to be inefficient for Bi-based perovskites. To overcome this problem, we replaced Cs^+ with Ag^+, which promotes a 3D crystal structure. The PV performances of the silver bismuth iodide system are found to be superior compared to any other bismuth-based perovskites reported so far. The highest power conversion efficiency is similar to that of $MAPbI_3$ when the latter was first incorporated in dye-sensitized solar cell (DSSC), but with

improved atmospheric stability. It is worth mentioning that silver bismuth iodide-based solar cells were produced in ambient atmosphere, which itself is a massive advantage over fabrication techniques of lead-based halide perovskites. Overall, our study reveals that a 3D crystal structure is an essential criterion for high-efficiency lead-free perovskites. Our study also demonstrates that the ns^2 electronic configuration is not a sufficient parameter to describe defect-tolerant semiconductor, rather should be considered as one of the necessary variables along with structural dimensionality.

Lay Summary

In 1839, a German mineralogist Gustav Rose discovered a unique crystal of $CaTiO_3$ in the Ural Mountains of Russia. He later named it 'Perovskite' in honor of a famous Russian mineralogist, Lev Perovski. With further development in material engineering, it has been found that many elements can be embedded in the same type of crystal structure, which gave rise to a new class of materials, collectively known as perovskite. After nearly 200 years, a group of researchers from Japan realized that a variant of perovskite (methylammonium lead iodide) is outstanding at harvesting light to efficiently convert into electricity. Thus, a new class of solar cell: perovskite solar cell (PSC) was born. Within the short span of a decade, PSCs surpassed other photovoltaic (PV) technologies in terms of efficiency, with current state-of-the-art PSC devices recording more than 24% efficiency. For comparison, the most widely used Silicon-based solar cells took nearly 60 years of extensive research to achieve more than 22% power conversion efficiencies. Moreover, with PSCs costing less than Si-based counterpart, it is unsurprising that PSCs have been identified as a promising emerging photovoltaic technology. However, the real challenges with PSCs in commercialization are long-term stability and heavy metal toxicity. To address these problems, we replaced lead with bismuth, which is non-toxic and offers excellent stability. However, PV performance of Bi-based perovskites ($Cs_3Bi_2I_9$) are found to be limited due to discontinuous inorganic motifs. To resolve this bottleneck, we replaced Cs with Ag to improve the chemical bonding between the atoms. The solar cells fabricated with silver bismuth iodide (Ag_xBiI_{3+x}) exhibited promising power conversion efficiency and excellent atmospheric stability despite being processed under ambient atmosphere. Hence, our study introduces a novel class of highly-stable materials that offers reasonable efficiency and free from heavy metal toxicity.

Acknowledgements

"If I have seen further than others, it is by standing on the shoulders of Giants"

Sir Isaac Newton

After completing four years in graduate studies, there may not be better words to sum up the experiences. This thesis is the outcome of the interaction with many great personalities I crossed path. Some are deliberate, and some are purely coincidental. Speaking of coincidences, I met Hemant and Dharani, a wonderful loving couple, on the first day I came to ERI@N. I was only an enthusiastic guy who wanted to try something new. They taught me how to do research and how to survive in graduate school. I am thankful for their guidance in the first few years of my research and maybe for after lunch snacks. Then there is Dr. Yin Ting, who is a professor now, helped me immensely in understanding what perovskites are. I am thankful for her time, suggestions and valuable comments. My theoretical understanding of the materials system began when I met Dr. Hao Wei and Prof. Li Shuzhou. Their guidance helped me to overcome one of the steepest learning curves, *i.e.* learning VASP. I am thankful to them for their patience and time and insight on first principle calculations.

I have also had the benefit of tremendous collaborators within ERI@N and beyond, who helped with experiments and discussion. This includes all the people from ERI@N but in particular Saikat, Thiru, Harikesh, Xintong, Chen Yan, Guifang, Wang Hao, Rohit, Xiaoting, Daymond, Abhijit, Bhumika, Herlina, Fadilah, Yan Fong, Asim, Sudhanshu, Stener, Benny, Naveen, Mohit, and Dr. Bahu. In Prof. Tze's lab, I am thankful to Dr. Wu Bo who performed the spectroscopic measurements. From UC Berkeley, Yao Cai and Prof. Mark Asta for their discussion on lead-free perovskites.

I would also like to thank Lily and Minying for helping me with the coursework and other duties as a student. I also acknowledge NTU and ERI@N for funding and providing cutting edge facilities and state of the art for my research.

I got some great friends at NTU who eased my staying here, most notably, Nirmalya, John and my entire football team members.

Lastly, I thank my thesis advisory committee without whom this thesis would neither started nor finished. Prof. Claude and Prof. Subodh were always there for me for a healthy discussion on the research progress. Most importantly, my biggest thank goes to my advisor, A/Prof. Nripan Mathews, for taking me a PhD student with no prior experience in photovoltaics and allowing me boundless freedom in my research. Thank you for giving me the opportunity to work on one of the most challenging problems in the current era.

Table of Contents

Table Captions

Figure Captions

Abbreviations

0D	Zero-dimensional
3D	Three-dimensional
CBM	Conduction Band Minimum
CL	Cathodoluminescence
DACTARI	Database for Chemical Toxicity and Radiotoxicity Assessment of Radionuclides
DFT	Density Functional Theory
DMF	Dimethylformamide
DMSO	Dimethylsulfoxide
DOS	Density of States
EDX	Energy Dispersive X-ray Spectroscopy
EQE	External Quantum Efficiency
ETL	Electron-Transporting Layer
eV	Electronvolt
FF	Fill Factor
FTO	Fluorine-doped Tin Oxide
GGA	Generalized Gradient Approximation
HTM	Hole-Transporting Material

JDOS	Joint Density of States
J_{SC}	Short-circuit Current Density
PCE	Power Conversion Efficiency
PL	Photoluminescence
PSC	Perovskite Solar Cell
PTFE	Polytetrafluoroethylene
PV	Photovoltaics
PXRD	Powder X-ray Diffraction
RH	Relative Humidity
SEM	Scanning Electron Microscopy
SOC	Spin-orbit coupling
UV	Ultraviolet
VASP	Vienna Ab-initio Simulation Package
VBM	Valence Band Maxima
Vis	Visible
V_{OC}	Open-circuit Voltage
XRD	X-ray Diffraction

Chapter 1

Introduction

Pb-based halide perovskites, in particular, methylammonium lead iodide ($CH_3NH_3PbI_3$) as a thin-film absorber material, have already surpassed other thin-film technologies with power conversion efficiencies (PCEs) over 23% at laboratory scale. Nevertheless, toxicity and stability remain critical issues for the widespread application of Pb-based halide perovskites. In this context, this chapter addresses the strategies for the development of novel perovskite materials that would be stable and non-toxic. Inspired by the excellent optoelectronic properties of Pb-halide perovskites, the screening criteria are established based on similarities in the chemical structure. Based on these criteria, bismuth-based halide perovskites were selected as an alternative PV absorber material. The specific hypotheses underlying the present work are presented in section 1.2. Section 1.3 outlines the objectives of this work that need to be reached. The organization and the key findings of this thesis are also given in the next section of this chapter.

1.1 Background and Broad Context

The advancement of modern civilization relies strongly on the availability of energy due to a strong nexus between economic progress and energy consumption [1]. The population growth creates a massive demand for energy which is forecast to increase by approximately 35% from 2010 to 2040 [2]. Unfortunately, 90% of global energy today comes from fossils fuel. On the one hand, fossils fuel resources are limited because they are not recoverable in the human timescale. On the other hand, burning fossils fuels largely contributes to CO_2 emissions into the atmosphere and subsequent climate changes.

The Sun is the most promising source of renewable energy considering its abundance and cleanliness. Covering about 0.16% of the earth's crust with 10% efficient devices would provide enough energy that would be equivalent to almost twice the global energy consumption rate [3]. The photovoltaic (PV) technology converts solar energy into electricity through solar cells. Since its inception, the PV technology has extended in many directions regarding materials, device architectures, and processing, with the silicon (Si)-based p-n junction solar cells almost completely dominating the market share today. While Si is abundant in the form of SiO_2, the substantial processing costs obtaining electronic grade Si for PV applications remain a significant bottleneck in terms of energy payback. Based on a similar architecture, materials such as CdTe, CuInGaSe, CuZnSnS have been also shown to have great potential as solar cell absorbers to achieve high efficiency. However, they also suffer from high costs, materials scarcity, and toxicity [4]. A breakthrough came in recent years with dye-sensitized solar cells (DSSCs), which is composed of inexpensive organic dyes as absorber materials [5-7]. This technology significantly reduces the materials and processing costs of solar cells. The use of Pb-based halide perovskite as a solar harvesting material was first conceived by Kojima, et al. [8] when they replaced the organic dyes with

$MAPbI_3$ and achieved an efficiency of ~3% using the DSSC configuration. Nevertheless, the use of iodide redox couple for charge transport was a significant challenge due to the instability of the perovskite in the liquid electrolyte environment. This problem was resolved by substituting the liquid electrolyte with a solid-state hole-transporting material (HTM) which improved both the efficiency and stability of the device. The organic-inorganic lead halide perovskites-based solar cells now achieved a remarkable milestone of >23% PCE. Regrettably, the development of perovskite solar cells (PSCs) is mostly focused on lead-based compounds. This impedes their commercial deployment due to the high toxicity of Pb and poor atmospheric stability of Pb-based perovskites. Therefore, there is a dire need to find an alternative material to replace lead while maintaining a comparable PV efficiency.

1.2 Hypothesis/Problem Statement

Over the last decade, PSCs have quickly emerged as one of the most promising third generation photovoltaics. More than thousands of articles on PSCs were published in 2015 alone from a hundred different research groups around the world. However, most of these articles were focused on the optoelectronic and photovoltaic properties of lead-based halide perovskites, especially methylammonium lead iodides ($MAPbI_3$, MA: $CH_3NH_3^+$) and its variants. The race to reach highly efficient PSCs paid limited attention to the lead toxicity and the development of lead-free perovskites. Figure 1.1 depicts the periodic table of elements based on their toxicity level. Lead is one of the most toxic elements in the periodic table with an LD_{50} value of 3-4 mg/kg (database for chemical toxicity and radiotoxicity assessment of radionuclides (DACTARI)). The lethal dose 50 (LD_{50}) of an element is defined as the amount needed to kill one-half of the units in the tested population after a certain period. The effect of lead toxicity on the human body is further described in detail in section 2.7.2 of chapter 2. Moreover, the high solubility of lead-based halide perovskites in

water increases the risk of environmental exposure manifolds; it will be a major obstacle to bring lead-based PSCs to the market considering the risk of leakage through rainwater from the damaged PSCs. Besides, lead-halide perovskites also suffer from instability in the ambient atmosphere. Recently the stability of PSCs has been greatly improved thanks to the multi-cation approach pioneered by the EPFL group [9-11]. However, lead-based halide perovskites continue to require stringent environmental conditions (usually an inert atmosphere with H_2O < 1 ppm) during fabrications, which will be a major impediment to the large-scale fabrications of solar modules. The present work, therefore, attempts to address these two key issues of toxicity and stability of lead-based PSCs.

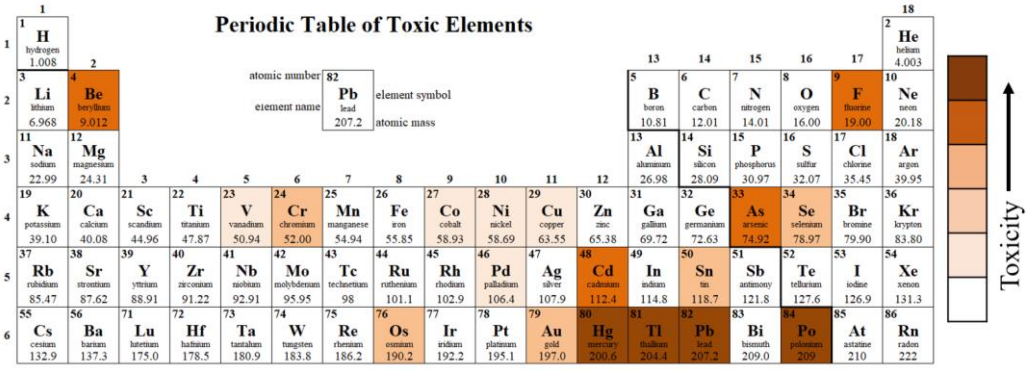

Figure 1.1: Periodic table of elements illustrating the toxicity of elements (the dark red color signifies acute toxicity and white color signifies practically non-toxic nature; the toxicity scale is based on the risk of exposure, the effect on humans and ecology, and LD_{50}). Data are collected from ref. [12-15].

One possible solution to both problems is to replace lead with a non-toxic metal cation in the perovskites structure without compromising the optoelectronic properties. The most common alternatives will be any non-toxic divalent cations, and there are several candidates satisfying these criteria as shown in

Figure 1.1. The Goldschmidt's tolerance factor, which provides a robust framework for the formation of a stable perovskite structure can be an additional criterion [16, 17]. However, even in the case of stable perovskite formation, there is no definite reason to expect excellent functional properties, which mostly depend on the electronic structure. As greater demand is placed on functionality, we followed an inverse design approach in which the electronic structure of $MAPbI_3$ was used as a searching criterion. The underlying principle is to imitate the electronic structure of $MAPbI_3$ with a non-toxic element instead of Pb, thus expecting similar optoelectronic properties. Recent theoretical studies revealed that the outstanding PV properties of $MAPbI_3$ are derived from the cubohedral coordination of Pb and halide atoms [18, 19]. Figure 1.2(a) illustrates the projected density of states for the ideal cubic $MAPbI_3$ perovskite, calculated with the generalized gradient approximation (GGA) within density functional theory (DFT). The A-site cation (MA^+ for $MAPbI_3$) takes no part in the photoactive region. The valence band maxima (VBM) is composed of mostly I(5*p*) orbital with a small contribution from Pb(6*s*) orbital. The conduction band minima (CBM), on the other hand, is dominated entirely by the Pb(6*p*) orbital. The role of each atomic constituent on the band edge is further illustrated by the orbital interaction diagram, as shown in Figure 1.2(b). The bonding type interaction between I(5*p*) and Pb(6*p*) creates the deeper part of the valence band and the antibonding interaction of the same results in the CBM. The VBM is formed by the antibonding interaction between I(5*p*) and Pb(6*s*) orbitals. This *s*-*p* transition is highly favorable during photo-absorption, thereby unraveling the origin of the high absorption coefficient of $MAPbI_3$. As strong absorption coefficient is extremely desirable for thin-film PV, the *s*-*p* transition will be an important parameter for designing lead-free halide perovskites. The defect tolerant nature of $MAPbI_3$ is another exceptional property that makes it an excellent thin-film PV material. The idea of defect tolerance was pioneered by Zhang, et al. [20],

who stated that the antibonding nature of VBM and the bonding nature of CBM can promote the formation of shallow defects, leaving the bandgap free from dangling bonds. For $MAPbI_3$, the antibonding nature of VBM arises from the partially oxidized state of Pb, leading to defect tolerance against acceptor-type defects. As the CBM of $MAPbI_3$ is antibonding in nature, it does not contribute directly to the defect tolerance for donor-type defects. However, the large relativistic effect of Pb pulls down the CBM, resulting in smaller bandgap and forcing the donor-type defects to resonate within the conduction bands. Further details on the defect tolerant properties of $MAPbI_3$ are explained in chapter 2. To summarize here, the excellent PV performance of $MAPbI_3$ which is mainly due to its strong absorption coefficient and defect tolerance nature, can be linked to its electronic structure. The *s-p* transition is responsible for its strong absorption coefficient which results in efficient photon absorption. The defect tolerance nature which is derived from the synergistic effect between antibonding VBM and relativistic spin-orbit coupling of Pb atoms, allows for efficient charge carrier generation and extraction.

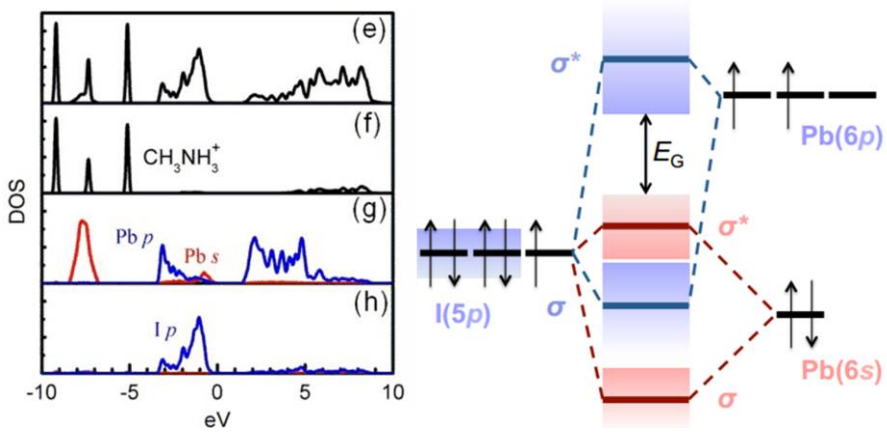

Figure 1.2: Electronic structure of $MAPbI_3$. (left) Density of states plot of ideal cubic $MAPbI_3$. (right) Schematic illustration of orbital interaction diagram in Pb-based iodide perovskites. Figure adapted from ref. [18, 19].

Therefore, post-transition metals with ns^2 electrons are suitable for substitution of lead in the perovskite structure, including In, Tl, Ge, Sn, Sb, and Bi, as illustrated in Figure 1.3. Such metals share similar electronic configuration as lead, thus expecting similar hybridization with halides and similar optoelectronic properties. Direct substitution of Pb with Sn has already attracted much attention as lead-free perovskites [21-23]. However, experimental studies indicate that Sn-based halide perovskites are even more precarious than Pb-based halide perovskites and suffer from severe atmospheric instability [23, 24]. Like Sn-based perovskites, germanium-based halide perovskites are also extremely unstable in ambient atmosphere, leading to limited PV applications [25]. From group 13, thallium-based compounds display very similar optoelectronic properties as lead-based compounds, in particular, the defect tolerant properties of TlBr was reported several years before similar works on $MAPbI_3$ [26, 27]. However, Tl is more toxic than Pb and unsuitable for commercial applications. From the same group, indium offers no toxicity, but its unstable +2 oxidation state and poor solubility in common organic solvents limits its thin-film PV applications.

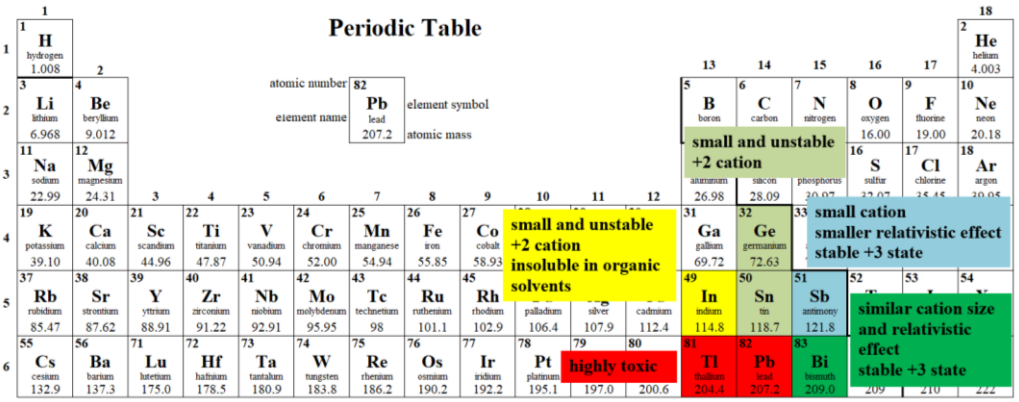

Figure 1.3: Possible replacement of Pb and their properties relating to solution-processed thin-film solar cell absorber materials.

The remaining candidates, antimony and bismuth from group 15 having ns^2 electronic configuration, are highly stable under ambient atmosphere and non-toxic, making them excellent candidates for replacing lead. Among them, bismuth is close to lead regarding its ionic size (easy incorporation into the perovskite lattice), atomic weight (responsible for relativistic effect), and electronegativity (Bi: 2.02, Pb: 2.33). Accordingly, Bi^{3+} will be a better candidate than Sb for replacing lead. Indeed, Bi^{3+} has been used as a non-toxic alternative of Pb for decades, in areas from organic chemistry to surgical procedures [28]. Figure 1.4 schematically illustrates the flow chart of this screening procedure to find alternatives of lead for PV applications.

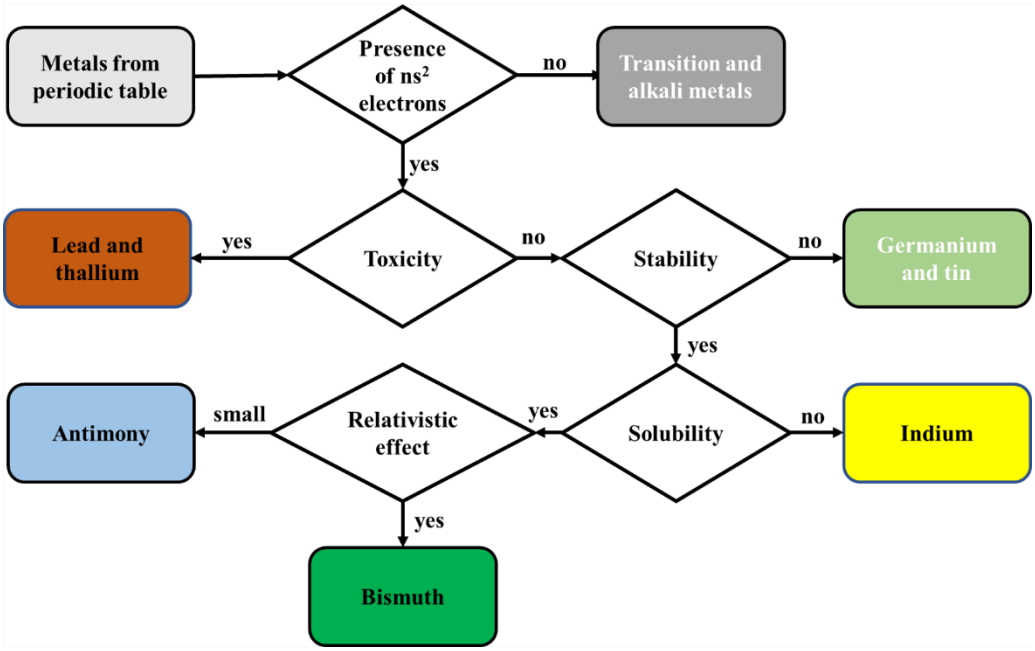

Figure 1.4: Flow chart representing the screening criteria of lead-free perovskites for solution-processed PV applications (see text for details).

Since the late 1990s, bismuth-based hybrid organic/inorganic halide compounds have been deemed as potential semiconductors for optoelectronic applications [29-31]. Most of the works, however, were limited to crystal structure and optical properties. Like Pb-based halide perovskites, Bi^{3+} also exhibits various anionic motifs with halides, ranging from corner-, edge-, and face-sharing octahedra depending on the size of the A- and X-site ions [32, 33]. However, contrary to lead-based halide perovskites, Bi-based halide perovskites tend to adopt vacancy-assisted distorted crystal structure with the chemical formula of $A_3Bi_2X_9$. This structure can be viewed as a defect-assisted perovskite structure with $A_3Bi_2{\square}X_9$, where □ denotes a Bi vacancy. However, the crystal dimensionality of Bi-based halide perovskites can be controlled to some degree by using different A-site cations. For example, large alkali metals such as Cs^+ tend to form a zero-dimensional crystal structure ($Cs_3Bi_2I_9$). Smaller cations such as Rb^+, on the other hand, forms two-dimensional crystal structure ($Rb_3Bi_2I_9$). Replacing alkali cations in the A-site with transition metals such as Cu^+ or Ag^+ generates different structural motifs that deviate from the octahedral perovskite structure. Nevertheless, heterogeneous bonding with transition metal cations can lead to higher dimensional structure [34, 35]. Because of this rich structural diversity and relative ease of fabrication by solution-processing techniques, bismuth-based ternary halides attracted massive attention recently as potential candidates for optoelectronic applications.

1.3 Objectives and Scopes

Although Bi-based halide perovskites exhibit interesting structural and optoelectronic properties, no systematic studies were conducted for PV applications at the time of this work. The primary objective of this dissertation is, therefore, to systematically investigate bismuth-based ternary iodides for photovoltaic applications as an alternative to lead-based halide perovskites. In order to fully accomplish this, a set of objectives were established as follow:

1. **Comparison of various A-site cations for novel bismuth-based perovskites.** Despite their limited role in the optoelectronic properties of Pb-based halide perovskites, the A-site cations heavily influence the stability and symmetry of perovskites. Among the many cations proposed, methylammonium ($CH_3NH_3^+$), formamidinium ($CH_5N_2^+$), and cesium (Cs^+) received the most attention. In order to investigate the effect of these cations on Bi-based perovskites, experiments will be conducted to synthesize phase pure compounds by solution-processing techniques. The role of these cations on the crystal structure of Bi-based perovskites will be analyzed by a comparative study using X-ray diffraction (XRD) and Rietveld refinement methods. Moreover, the stability and optical properties of these Bi-based perovskites will be characterized by XRD and UV-Visible spectroscopy to narrow down the promising candidates for photovoltaics.

2. **Understanding the optoelectronic properties of novel bismuth-based perovskites.** Different spectroscopic techniques will be exploited to understand the optoelectronic properties that will further unravel the excited-state carrier dynamics in bismuth-based perovskites. Photoluminescence and electroluminescence characterizations can be useful to probe the spectroscopic and dynamic radiative recombination within the thin-films which is of paramount importance for the performance of solar cells. Furthermore, transient absorption spectroscopy will assist to uncover the recombination kinetics of excited-state carriers, which will provide more insight into the intrinsic properties of bismuth-based perovskite system. Besides, in-depth optoelectronic studies will also aid in understanding the fundamental properties for the desired applications over a broad spectral range and to identify any fundamental restrictions. These fundamental studies aim to direct future studies on the development of bismuth-based perovskites.

3. **Using first-principle calculations to complement the experimental findings.** The limitations of experimental characterizations due to processing conditions, atmosphere, and uncertainty can be bypassed through a robust theoretical framework. Density functional theory (DFT) has been proven essential in understanding the electronic properties as well as defect characteristics. The optical and transport properties of a semiconductor can be predicted from the electronic bandstructure calculations. A proprietary software, VASP (Vienna Ab-initio Simulation Package) will be used to investigate the electronic structure of the Bi-based perovskite. The usefulness of DFT to accurately calculate the ground-state energy will be utilized in the characterizations of intrinsic defects. Based on the simulation results, a new course of actions will be taken during fabrication of Bi-based perovskite solar cells.

4. **Fabricating lead-free photovoltaics based on mesoscopic solar cell architecture.** The goal of this study is to investigate the Bi-based perovskite as a lead-free solar cell absorber material. For that purpose, the design of experiments for fabricating solar cells will be carried out based on current knowledge associated with Pb-based perovskites and our understanding of the optoelectronic properties of Bi-based perovskites. Optimizations of fabrication route, charge transport layers, and characterizations of solar cells will be of prime importance. Although conventional spin coating techniques yield highly efficient Pb-based halide perovskites, it requires stringent environmental control. An attempt will be made to improve the spin-coating process that can be carried out in ambient atmosphere without deteriorating the performance of solar cells.

1.4 Dissertation Overview

This thesis aims to provide a comprehensive description of Bi-based ternary iodides as lead-based halide perovskites alternatives. The experimental investigations are complemented by first principle calculations to elucidate the role of structure-property relationships for PV applications. A particular goal of this thesis is to demonstrate reasonable PCE from stable lead-free compounds via solution-processing techniques, using various facets of engineering to address some of the technical problems faced by lead-free perovskite solar cells. Each of these avenues will be explored through the following chapters. A brief summary of each chapter is provided below.

Chapter 1 provides the rationale and scope behind the selection of bismuth-based perovskite as a lead-free alternative for PV applications. Although lead-based halide perovskites are highly efficient, the toxicity of lead-based compounds cannot be ignored. Bismuth, on the other hand, is not toxic and possesses a similar electronic configuration as that of lead.

Chapter 2 describes the historical and contemporary literature related to this thesis. This chapter can be subdivided into two parts. The first part describes what perovskites are and what is so special about them. A brief history on perovskite solar cell and its route to the fastest growing thin-film solar cell are also provided. The next part describes the development of lead-free solar cells. Here it should be noted that only full replacement of lead in perovskite solar cell configurations is considered. We focused mostly on the seminal works from various research groups that are relevant to our works.

Chapter 3 discusses the principles underlying various experimental methodologies and theoretical calculations. The first part of this chapter is mostly focused on the experimental instruments that have been used throughout this work. The next part describes the first principle calculations used for

electronic bandstructure calculations and defect properties characterizations in $Cs_3Bi_2I_9$ compounds.

Chapter 4 is devoted to a systematic study on Bi-based iodide perovskites' structure and stability. Initially, three cations (cesium, methylammonium, and formamidinium) were used for fabrications of bismuth iodide perovskites. By comparing stability and optical properties, $Cs_3Bi_2I_9$ was selected as a prototype bismuth-based perovskite for in-depth characterizations by various spectroscopic techniques. Later, performances of $Cs_3Bi_2I_9$-based solar cells are evaluated in mesoscopic architectures.

Chapter 5 describes the first principle investigations on $Cs_3Bi_2I_9$ which was initially thought to be a defect tolerant semiconductor. The electronic bandstructure calculation revealed that $Cs_3Bi_2I_9$ is an indirect bandgap semiconductor in agreement with the experimental results. Further, we investigated the defect characteristics of $Cs_3Bi_2I_9$ which revealed that defects that have low formation energy could create deep bandgap states. Here, the possible remedy was also envisioned for defect passivation in this compound which was then experimentally proven.

Chapter 6 discusses the emergence of silver bismuth iodide semiconductor, the idea of which is based on the studies carried out on Bi-based iodide perovskites. Detailed morphological and optoelectronic characterizations of silver bismuth iodides are presented and discussed. A modified spin-coating technique was developed to fabricate highly efficient lead-free solar cells based on silver bismuth iodide under ambient conditions. Speculations are made on mechanisms that might be responsible for the observed improved PV performance.

Chapter 7 focuses on the future outlook of lead-free perovskites research as a whole. The discussion also comprises the shortcoming of the current bismuth-

based halide perovskites and possible pathways to circumvent the challenges.

1.5 Findings and Outcomes

The research led to several scientific outcomes by:

1. The correlations between structure and optical properties of novel Bi-based perovskites utilizing different A-site cations. The optical bandgaps of bismuth-based perovskites are found to be insensitive towards the size of A-site cations as long as the compound crystallizes into the $A_3Bi_2I_9$ structure.

2. Photovoltaic characterizations on $Cs_3Bi_2I_9$ reveal that solar cell performances are limited by low electronic dimensionality which prevents efficient charge transfer. This study serves to benchmark the PV performances of zero-dimensional Bi-based perovskites while unveiling their optoelectronic properties.

3. Defect tolerant properties of a semiconductor do not only depend on the bonding orbitals as initially thought for Pb-based halide perovskites. First principle calculations reveal the effect of the electronic dimensionality on the bonding environment and their role in low-dimensional perovskites as a whole.

4. Silver bismuth iodide can be a potential solar cell absorber material in thin-film solar cell configurations which offers great atmospheric stability, high absorption coefficient as well long carrier lifetime, properties essential for single junction solar cell.

5. Dynamic hot casting technique was found to be suitable for fabricating thin-film solar cells in the ambient atmosphere which resulted in larger

grains and better coverage as compared to the conventional spin coating technique.

References

[1] I. Ozturk, A. Aslan, and H. Kalyoncu, "Energy consumption and economic growth relationship: Evidence from panel data for low and middle income countries," *Energy Policy,* vol. 38, pp. 4422-4428, 2010.

[2] G. Giorgi, J.-I. Fujisawa, H. Segawa, and K. Yamashita, "Small Photocarrier Effective Masses Featuring Ambipolar Transport in Methylammonium Lead Iodide Perovskite: A Density Functional Analysis," *J. Phys. Chem. Lett.,* vol. 4, pp. 4213-4216, 2013/12/19 2013.

[3] N. Armaroli and V. Balzani, "The Future of Energy Supply: Challenges and Opportunities," *Angew. Chem. Int. Ed.,* vol. 46, pp. 52-66, 2007.

[4] A. Shah, P. Torres, R. Tscharner, N. Wyrsch, and H. Keppner, "Photovoltaic Technology: The Case for Thin-Film Solar Cells," *Science,* vol. 285, pp. 692-698, 1999-07-30 00:00:00 1999.

[5] B. O'regan and M. Gratzel, "A low-cost, high-efficiency solar cell based on dye-sensitized," *Nature,* vol. 353, pp. 737-740, 1991.

[6] M. Grätzel, "Dye-sensitized solar cells," *J. Photoch. Photobio. C,* vol. 4, pp. 145-153, 10/31/ 2003.

[7] A. J. McEvoy and M. Grätzel, "Sensitisation in photochemistry and photovoltaics," *Sol. Energy Mater. Sol. Cells,* vol. 32, pp. 221-227, 1994.

[8] A. Kojima, K. Teshima, Y. Shirai, and T. Miyasaka, "Organometal Halide Perovskites as Visible-Light Sensitizers for Photovoltaic Cells," *J. Am. Chem. Soc.,* vol. 131, pp. 6050-6051, 2009/05/06 2009.

[9] J.-P. Correa-Baena, M. Saliba, T. Buonassisi, M. Grätzel, A. Abate, W. Tress, *et al.,* "Promises and challenges of perovskite solar cells," *Science,* vol. 358, pp. 739-744, 2017.

[10] M. Saliba, T. Matsui, J.-Y. Seo, K. Domanski, J.-P. Correa-Baena, M. K. Nazeeruddin, *et al.,* "Cesium-containing triple cation perovskite solar

cells: improved stability, reproducibility and high efficiency," *Energy Environ. Sci.*, vol. 9, pp. 1989-1997, 2016.

[11] M. Saliba, T. Matsui, K. Domanski, J.-Y. Seo, A. Ummadisingu, S. M. Zakeeruddin, *et al.*, "Incorporation of rubidium cations into perovskite solar cells improves photovoltaic performance," *Science*, vol. 354, pp. 206-209, 2016.

[12] P. Carson and C. Mumford, "5 - Toxic chemicals," in *Hazardous Chemicals Handbook (Second edition)*, P. Carson and C. Mumford, Eds., ed Oxford: Butterworth-Heinemann, 2002, pp. 67-177.

[13] K. S. Egorova and V. P. Ananikov, "Toxicity of Metal Compounds: Knowledge and Myths," *Organometallics*, vol. 36, pp. 4071-4090, 2017/11/13 2017.

[14] Q. Sun and W.-J. Yin, "Thermodynamic Stability Trend of Cubic Perovskites," *J. Am. Chem. Soc.*, vol. 139, pp. 14905-14908, 2017/10/25 2017.

[15] D. B. Mitzi, C. A. Feild, W. T. A. Harrison, and A. M. Guloy, "Conducting tin halides with a layered organic-based perovskite structure," *Nature*, vol. 369, pp. 467-469, 06/09/print 1994.

[16] G. Kieslich, S. Sun, and A. K. Cheetham, "An extended Tolerance Factor approach for organic–inorganic perovskites," *Chem. Sci.*, vol. 6, pp. 3430-3433, 2015.

[17] W. Travis, E. N. K. Glover, H. Bronstein, D. O. Scanlon, and R. G. Palgrave, "On the application of the tolerance factor to inorganic and hybrid halide perovskites: a revised system," *Chem. Sci.*, vol. 7, pp. 4548-4556, 2016.

[18] W.-J. Yin, T. Shi, and Y. Yan, "Superior Photovoltaic Properties of Lead Halide Perovskites: Insights from First-Principles Theory," *J. Phys. Chem. C*, vol. 119, pp. 5253-5264, 2015/03/12 2015.

[19] R. E. Brandt, V. Stevanović, D. S. Ginley, and T. Buonassisi, "Identifying defect-tolerant semiconductors with high minority-carrier lifetimes: beyond hybrid lead halide perovskites," *MRS Communications,* vol. 5, pp. 265-275, 2015.

[20] S. B. Zhang, S.-H. Wei, A. Zunger, and H. Katayama-Yoshida, "Defect physics of the $CuInSe_2$ chalcopyrite semiconductor," *Phys. Rev. B,* vol. 57, pp. 9642-9656, 1998.

[21] F. Hao, C. C. Stoumpos, D. H. Cao, R. P. H. Chang, and M. G. Kanatzidis, "Lead-free solid-state organic–inorganic halide perovskite solar cells," *Nat. Photonics,* vol. 8, p. 489, 05/04/online 2014.

[22] M. H. Kumar, S. Dharani, W. L. Leong, P. P. Boix, R. R. Prabhakar, T. Baikie, *et al.*, "Lead-Free Halide Perovskite Solar Cells with High Photocurrents Realized Through Vacancy Modulation," *Adv. Mater.,* vol. 26, pp. 7122-7127, 2014.

[23] N. K. Noel, S. D. Stranks, A. Abate, C. Wehrenfennig, S. Guarnera, A.-A. Haghighirad, *et al.*, "Lead-free organic–inorganic tin halide perovskites for photovoltaic applications," *Energy Environ. Sci.,* vol. 7, pp. 3061-3068, 2014.

[24] T. M. Koh, T. Krishnamoorthy, N. Yantara, C. Shi, W. L. Leong, P. P. Boix, *et al.*, "Formamidinium tin-based perovskite with low Eg for photovoltaic applications," *J. Mater. Chem. A,* vol. 3, pp. 14996-15000, 2015.

[25] T. Krishnamoorthy, H. Ding, C. Yan, W. L. Leong, T. Baikie, Z. Zhang, *et al.*, "Lead-free germanium iodide perovskite materials for photovoltaic applications," *J. Mater. Chem. A,* vol. 3, pp. 23829-23832, 2015.

[26] A.-V. Mudring, "Thallium Halides – New Aspects of the Stereochemical Activity of Electron Lone Pairs of Heavier Main-Group Elements," *Eur. J. Inorg. Chem.,* vol. 2007, pp. 882-890, 2007.

[27] M.-H. Du, "First-principles study of native defects in TlBr: Carrier trapping, compensation, and polarization phemomenon," *J. Appl. Phys.*, vol. 108, p. 053506, 2010.

[28] R. Mohan, "Green bismuth," *Nat. Chem.*, vol. 2, p. 336, 04/01/online 2010.

[29] G. A. Mousdis, G. C. Papavassiliou, A. Terzis, and C. P. Raptopoulou, "Notizen: Preparation, Structures and Optical Properties of $[H_3N(CH_2)_6NH_3]BiX_5$ (X=I, Cl) and $[H_3N(CH_2)_6NH_3]SbX_5$ (X=I, Br)," in *Zeitschrift für Naturforschung B* vol. 53, ed, 1998, p. 927.

[30] D. B. Mitzi, "Organic−Inorganic Perovskites Containing Trivalent Metal Halide Layers: The Templating Influence of the Organic Cation Layer," *Inorg. Chem.*, vol. 39, pp. 6107-6113, 2000/12/01 2000.

[31] D. B. Mitzi and P. Brock, "Structure and Optical Properties of Several Organic−Inorganic Hybrids Containing Corner-Sharing Chains of Bismuth Iodide Octahedra," *Inorg. Chem.*, vol. 40, pp. 2096-2104, 2001/04/01 2001.

[32] L.-M. Wu, X.-T. Wu, and L. Chen, "Structural overview and structure–property relationships of iodoplumbate and iodobismuthate," *Coord. Chem. Rev.*, vol. 253, pp. 2787-2804, 2009/12/01/ 2009.

[33] N. Mercier, N. Louvain, and W. Bi, "Structural diversity and retro-crystal engineering analysis of iodometalate hybrids," *CrystEngComm*, vol. 11, pp. 720-734, 2009.

[34] W.-X. Chai, L.-M. Wu, J.-Q. Li, and L. Chen, "Silver Iodobismuthates: Syntheses, Structures, Properties, and Theoretical Studies of $[Bi_2Ag_2I_{10}^{2-}]_n$ and $[Bi_4Ag_2I_{16}^{2-}]_n$," *Inorg. Chem.*, vol. 46, pp. 1042-1044, 2007/02/19 2007.

[35] W.-X. Chai, L.-M. Wu, J.-Q. Li, and L. Chen, "A Series of New Copper Iodobismuthates: Structural Relationships, Optical Band Gaps Affected

by Dimensionality, and Distinct Thermal Stabilities," *Inorg. Chem.*, vol. 46, pp. 8698-8704, 2007/10/01 2007.

Chapter 2

Literature Review

A holistic view of the current developments in the field of perovskite solar cells (PSCs) is provided in this chapter, which begins with a short description of the perovskite crystal structure. The emergence of PSCs from dye-sensitized solar cells is highlighted with the current progress in terms of power conversion efficiencies and solar cell architectures. A concise commentary is made on the unique optoelectronic properties of Pb-based halide perovskites and the correlation between the crystal structure and optoelectronic properties. The chapter ends with a short review on lead-free perovskites and their development as absorber materials for photovoltaic applications.

2.1 Crystal Structure of Perovskites

Perovskites represent a wide class of compounds, epitomized by the ABX_3 crystal structure, in which *A*- and *B*-sites are occupied by two different cations, and the *X*-sites are occupied by anions. The structure consists of a continuous network of corner-sharing $[BX_6]^{4-}$ octahedra with A-site cations occupying the cuboctahedral voids as illustrated in Figure 2.1. The crystal structure of perovskites is known to be very flexible, and a large number of perovskite compounds can be formed by varying *A*, *B*, and *X*-site atoms. In addition, several distorted and defect-assisted crystal structures with $[BX_6]^{4-}$ octahedra are also included in the perovskite family. The structural stability of the perovskite structure is strictly controlled by the size of the constituent ions which must follow Goldschmidt's tolerance factor (*t*):

$$t = \frac{r_A + r_X}{\sqrt{2}(r_B + r_X)} \quad (1)$$

where, r_i denotes the ionic radii of the respective ions (*A*, *B*, and *X*). At finite temperature, if *t* falls within the range [0.8–1.0], the compounds are most likely to form a stable perovskite structure. Distorted or non-perovskite phases are observed for $t > 1.0$ or < 0.8. It was later realized that a right *t*-value is necessary, but not a sufficient condition for stable perovskite structure formation. The introduction of octahedral factor ($\mu = {r_B}/{r_X}$) further improves the prediction of perovskite formability [1, 2]. Historically, oxide perovskites (in which the anion is oxygen) have received more attention due to their intriguing ferroelectric, magnetic, and superconducting properties [3]. However, halide perovskites have gained more interest as of late due to their fascinating optoelectronic properties and excellent PV performances. For lead-based halide perovskites, the *B*-sites are essentially occupied by Pb^{2+}, the *A*-sites are occupied by organic/inorganic protonated cations, and the *X*-sites are occupied by one or more types of halide anions (Cl^-, Br^-, I^-). For PV applications, the *A* is

a monovalent organic cation such as methylammonium ($CH_3NH_3^+$, abbreviated MA) or formamidinium (NH_2=$CHNH_2^+$, abbreviated FA), or inorganic alkali metals such as Cs^+. Both *A*-site and *X*-site can be occupied by single or multiple types of ions, but the octahedral and tolerance factors must be followed for a stable perovskite structure, as illustrated in Figure 2.1(b). Based on these criteria, different combinations of organic/inorganic cations and halide atoms have been proposed, synthesized, and characterized. Most interestingly, any combination of cations at the A-site (within tolerance limit) exhibits excellent optoelectronic properties in general.

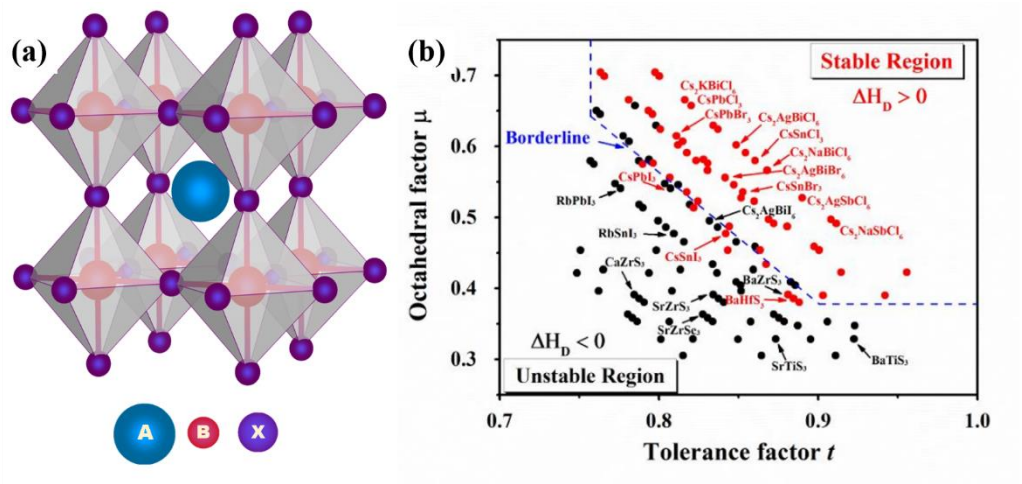

Figure 2.1: Perovskite crystal structure and stability region based on Goldschmidt's tolerance factor and octahedral factor. (a) Schematic illustration of crystal structure of ideal cubic perovskites (ABX_3) showing [BX_6] octahedra. For PV applications, the *A*-site is usually the methylammonium ion ($CH_3NH_3^+$), the *B*-site cation is Pb^{2+} and *X*-sites are occupied by halide ion (usually I^-, but both Cl^- and Br^- are also of interest). The cubic phase of $CH_3NH_3PbI_3$ is stable only above 330 K. (b) The (t, μ) map for 138 perovskite compounds showing stable (red) and unstable (black) compounds based on DFT formation energy calculations. Figure adapted from ref. [4].

2.2 Progress of Perovskite-based Solar Cells

While halide perovskites are known for many decades, studies related to optoelectronic devices were only instigated by Mitzi *et. al.* [5, 6] in the 1990s. Nevertheless, the use of halide perovskites in photovoltaics was not realized until Kojima, *et al.* [7] demonstrated using $CH_3NH_3PbX_3$ (X = Br, I) as a visible light sensitizer in photoelectrochemical cells in 2009. Despite the low power conversion efficiency (~3%) and extreme instability in liquid electrolytes, the devices showed impressive open-circuit voltage (V_{OC} = 0.96 V with $CH_3NH_3PbBr_3$) along with 65% external quantum efficiency (EQE). The efficiency was further improved by Im, *et al.* [8] through optimizing the mesoporous layer and concentration of perovskite precursor. They achieved an efficiency of 6.5% ((J_{SC} = 15.82 mA cm^{-2}, V_{OC} = 0.706 V and FF = 0.586) with $CH_3NH_3PbI_3$. However, the biggest problem was the stability of the devices due to the high solubility of halide perovskites in liquid electrolytes. A breakthrough came in 2012 when Kim, *et al.* [9] replaced the liquid electrolyte with a solid-state hole-conductor, Spiro-OMeTAD. They achieved a record efficiency of 9.7% from $CH_3NH_3PbI_3$ using 0.6 μm thick TiO_2 mesoporous layer as a scaffold. At the same time, Lee, *et al.* [10] revealed that TiO_2 mesoporous layer is not necessary for high-performance perovskite solar cells. They used a mixed halide $CH_3NH_3PbI_{3-x}Cl_x$ system as an absorber layer on both Al_2O_3 and TiO_2 mesoporous layer, and the highest efficiency (10.9%) was achieved with an insulant Al_2O_3 where no charge extraction occurs. These two reports were the main catalyst that triggered the explosive research activity on halide perovskites around the globe.

Later, a combined effort from Gratzel's and Seok II's groups [11] resulted in a record efficiency of 12% utilizing $CH_3NH_3PbI_3$ as the light harvester with a mesoporous TiO_2 as ETL and PTAA as HTM. A further improvement in efficiency was recorded by Burschka, *et al.* [12] when they developed a 2-step

deposition technique in which lead iodide (PbI_2) was first spin-coated on a mesoporous TiO_2 layer, followed by dipping into a CH_3NH_3I solution for conversion into the $CH_3NH_3PbI_3$ absorber layer. Their efficiency was first to be verified by an independent accredited test center which certified an efficiency of 14.1%. In the same year, Snaith's group also reported a planar perovskite solar cell with an efficiency of 15.1% [13]. The planar structure does not contain any mesoporous layer, which allowed a two-source thermal evaporation technique for $CH_3NH_3PbCl_xI_{3-x}$ deposition. Another breakthrough came when Seok II and coworkers developed an antisolvent treatment for the thin-film fabrication and reported a record 16.2% efficient perovskite solar cell [14]. The antisolvent technique eventually became a standard procedure for high-efficiency PSC fabrication. This was followed by 19% (18% certified) [15] and later a landmark value of 20.2% [16] power conversion efficiency at 1 sun illumination. At the end of 2015, the efficiency of perovskite solar cells reached to a record value of 21.1%, which was eventually broken by researchers from KRICT and UNIST with a certified efficiency of 22.7% for a single-junction perovskite solar cell [17]. The graphic representation in Figure 2.2 illustrates the current success of Pb-based halide perovskites as compared to other PV technologies in the last 45 years. Meanwhile, perovskite solar cells also underwent rapid developments in the other vital areas such as stability, device engineering, interface engineering, charge transporting materials, and understanding of the fundamental properties.

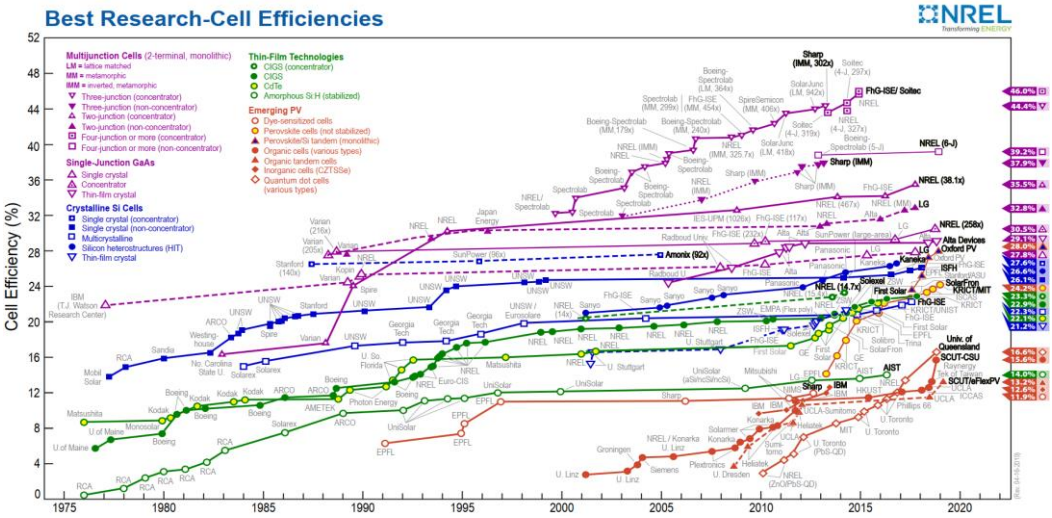

Figure 2.2: Progress of several photovoltaic technologies. Figure adapted from ref. [18].

2.3 Perovskite Solar Cell Architecture

The first perovskite solar cell (PSC) was envisioned as a dye-sensitized solar cell (DSSC) in which $MAPbI_3$ was used as an alternative dye on a mesoporous TiO_2 (mp-TiO_2) layer, and a liquid redox electrolyte was used for charge transfer to the electrode. The electrolyte was subsequently substituted by solid-state hole-transport materials (HTM) which improved the efficiency and stability of the solar cells. Since then, PSCs have progressed into two distinct device architectures: one is mesoscopic, and the other is planar. In both cases, the perovskite layer is sandwiched between selective charge extraction layers. A nanoporous oxide scaffold layer is impregnated with the perovskite absorber in the mesoscopic framework. For better loading and efficient extraction, a perovskite capping layer is usually required on top of the scaffold. The planar structure, on the other hand, avoids the use of mesoporous layers, taking advantage of the long carrier diffusion-length of lead halide perovskites. Depending on the fabrication route, both structures can be viewed as *p*(p-type

selective layer)-*i*(intrinsic absorber layer)-*n*(n-type selective layer) or *n*-*i*-*p* thin-film solar cells. In general, a transparent conducting glass serves as a substrate on which the ETL (for *n*-*i*-*p* configuration) or HTM (for *p*-*i*-*n* configuration) is deposited, followed by a perovskite absorber layer, a hole selective layer (for n-i-p configuration) or an electron selective layer (for p-i-n configuration), and a metal contact subsequently deposited (Figure 2.3). As the mesoscopic scaffold requires high temperature sintering steps (typically 500 ℃ for TiO_2), it excludes the use of low melting point substrates, such as plastics. Planar structure, on the other hand, provides a simplified and low temperature processing route for flexible substrates as well. However, the solar cell performances of both architectures are comparable, with record PCEs of over 20% under 1 sun illumination [17, 19]. More recently, multi-junction PV devices (tandem) have shown promise for their low cost and the potential to exceed the Shockley-Queisser efficiency limit [20-22]. To further reduce the costs of HTMs, triple mesoscopic perovskite solar cells have received considerable attention recently. In triple mesoscopic perovskite solar cells, three different mesoscopic layers are stacked together, followed by deposition of the perovskite layer. The mesoscopic layers are usually made from screen-printed mesoporous TiO_2, a ZrO_2 spacer layer, and a carbon electrode. This type of device structure requires no HTMs or back metal contact, reducing costs further and improving the device stability [23, 24].

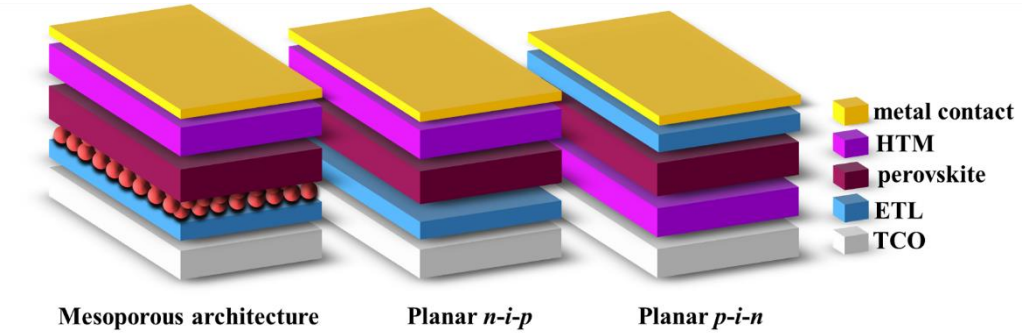

Figure 2.3: Commonly used perovskite solar cells architecture: Schematics of PSCs based on (left) mesoscopic configuration, (middle) planar structure with *n-i-p* configuration, and (right) planar *p-i-n* configuration (commonly referred to as "inverted").

2.4 Working principles

The first perovskite solar cell was built on the exact frame of the dye-sensitized solar cells (DSSCs) or Grätzel cells [25], in which the *n*-type TiO_2 electrode was sensitized with the perovskite quantum dots and placed inside a liquid electrolyte (I^-/I^-_3 redox couple). Currently, several types of perovskite solar cell architecture are used, as discussed in the previous section. While the operating principles of different architectures are almost the same as shown in Figure 2.4, the excited-state carrier dynamics and charge transfer may vary depending upon the PSC architecture. Since the solar cells reported in this thesis are based on the mesoscopic architecture, the working principles of the mesoscopic architecture are discussed here.

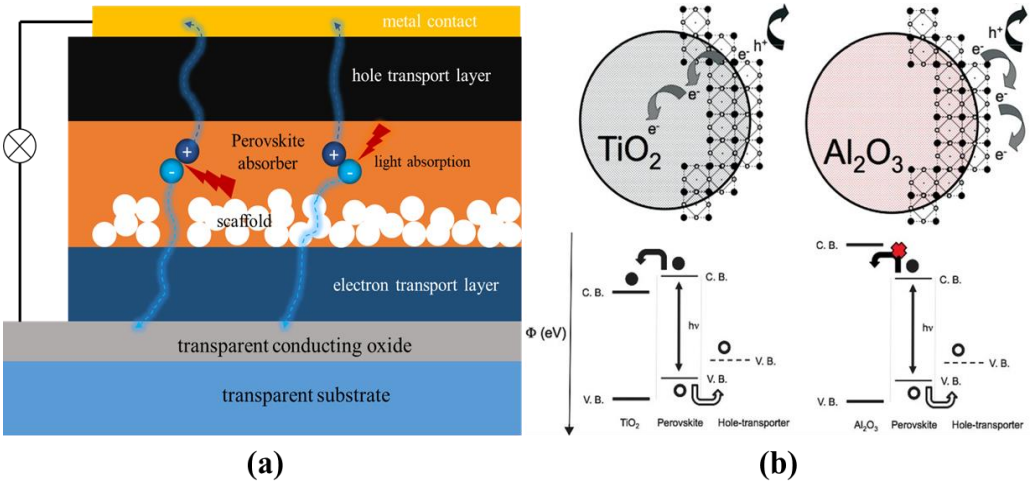

Figure 2.4: Working principle of perovskite solar cells. (a) Schematic illustration of charge generation and transport inside mesoporous PSCs. (b) Charge transfer mechanism in TiO_2 and Al_2O_3 mesoporous layer in perovskite-based solar cells. Figure adapted from ref. [26].

Originally developed from the DSSCs, the mesoscopic architecture is composed of an *n*-type mesoporous scaffold layer (mp-TiO_2), on which the perovskite is deposited. In contrast to single layer absorbers in DSSCs, this perovskite layer can infiltrate pores and form a capping layer on top of the scaffold (Figure 2.4(a)). After photo-absorption, a bound electron-hole pair (exciton) is formed inside the bulk perovskite, which readily converted into free carriers at room temperature due to its low exciton binding energy. Eventually, charge separation occurs by injecting the electrons into the ETL and the holes into the HTM. Both processes occur in ps timescale, which is much faster than the recombination timescale (ns to μs) in bulk or at interfaces, resulting in an efficient charge transfer across the layers [27]. Nevertheless, the presence of *n*-type mp-TiO_2 is not necessary for efficient PSCs. It has been demonstrated that insulating mesoporous layers such as Al_2O_3 or ZrO_2 layer-based devices perform as efficiently. This indicates that the interface is not required for charge

separation in PSCs. Later, Etgar, *et al.* [28], [29] presented HTM-free perovskite devices, indicating that perovskite can also function as an effective HTM. With further progress in this field, the ambipolar nature of $MAPbI_3$ was supported experimentally [30] and computationally [31-33]. In view of the multiple functions of the perovskite layer in PSCs, the possible charge transfer mechanisms along different layers in TiO_2 and Al_2O_3-based solar cells are schematically exemplified in Figure 2.4(b). Although the presence of an n-type mesoporous layer brings no added advantage for $MAPbI_3$-based PSCs, the charge collection efficiency is greatly influenced by the mesoscopic layer for 'not-so-good' semiconductors [34]. Hence, the Bi-based perovskites solar cells, in this thesis, are fabricated based on the mesoscopic solar cell architecture to utilize efficient charge collection mechanism.

2.5 Unique Optoelectronic Properties of $MAPbI_3$

Over a short period, perovskite solar cells (PSCs) exhibited remarkable progress in terms of PCE through rapid development in device architecture, charge transport layer, deposition methods, and compositional engineering. The exponential growth of PSCs is often attributed to the exceptional optoelectronic properties of $MAPbI_3$, which are fittingly tailored to PV applications. However, many of its current achievements are also due to the through ongoing investigations of the fundamental properties. While some crucial issues still remain unanswered [35], the following section highlights the key aspects of $MAPbI_3$ that make it so unique for PV applications.

2.5.1 Broad and Tunable Light Absorption

The most critical parameter of a PV material is the absorption coefficient (α). Methylammonium lead iodide ($MAPbI_3$) has a direct bandgap of ~1.6 eV with high absorption coefficient (~10^5 cm^{-1}) in the visible range [30]. The strong optical absorption allows the required thickness to be extremely thin without

sacrificing the photogenerated carriers. For example, the PSCs only require an absorber layer of 0.3–0.6 μm, while crystalline silicon solar cells need about 300 μm to absorb the visible light fully. Figure 2.5 shows the absorption coefficient spectra of various semiconductor materials used for high performing PV applications. Besides, the thin absorber layer further minimizes open-circuit voltage (V_{OC}) loss by reducing charge recombination induced saturated dark current [36]. The strong absorption coefficient of $MAPbI_3$ can be explained by the presence of large joint density of states (JDOS) near the bandgap and the favorable *s-p* transition [37]. Given the high absorption coefficient and direct bandgap, a 200 nm thin-film of $MAPbI_3$ can achieve a theoretical efficiency up to 21% [38]. Besides, the absorption edge of lead halide perovskites can be easily tuned by partially or fully replacing A-site cations and halogen atoms, without significant changes in optoelectronic properties (Figure 2.5). This would widen the possibility of different types of optoelectronic devices.

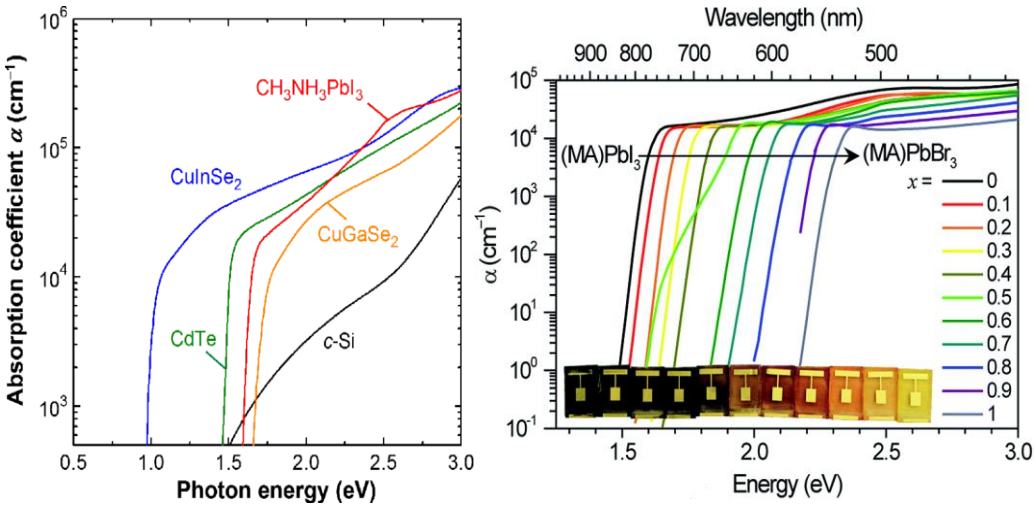

Figure 2.5: Absorption spectra of lead halide perovskites. (left) Absorption coefficient of semiconductors for PV applications. (right) The absorption coefficient spectra of $MAPb(Br_xI_{1-x})_3$. Inset: photograph of $MAPb(Br_xI_{1-x})_3$ based PSCs with *x* ranging from 0 to 1 (left to right). Figure adapted from ref. [39, 40].

2.5.2 Efficient Free Charge Carrier Generation

High absorption coefficient is necessary but not a sufficient condition for generating large photo-carriers, it would also rely on the efficient dissociation of the exciton (bound hole-electron pair). Exciton binding energy (E_b) is the minimum energy required to separate the excitons into free carriers, which contribute to the photocurrent. If $E_b < kT$, then thermal energy would be sufficient to generate free carriers; therefore, small exciton binding energy (less than room temperature thermal energy ~26 meV) is highly desirable for PV applications. On the other hand, additional efforts are needed for semiconductors having $E_b > kT$ to ensure that excitons at room temperature are dissociated. For example, a significant form of V_{OC} loss in organic photovoltaics (OPVs) is due to the energy required to separate Frenkel excitons, which have large exciton binding energy (0.20 – 1.0 eV) [36, 41]. The E_b for $MAPbI_3$ is much lower than OPVs, with values ranging from just two meV to as high as 75 meV depending upon the morphology, crystallinity of films and measuring techniques [42-46]. However, it is agreed that free charge carriers dominate the conversion process from photons to photocurrent in PSCs [36, 47]. This essentially confirms the non-excitonic nature of $MAPbI_3$ and the mechanism of small V_{OC} losses in PSCs.

2.5.3 Exceptionally Long Carrier Diffusion-length

Since $MAPbI_3$ is an excellent PV material, the carrier diffusion length in thin-films exceeds one μm [30] and up to 175 μm in single crystals [48]. For comparison, the typical low temperature processed semiconductors have a carrier diffusion lengths about 10 nm [49]. The long carrier diffusion-length in $MAPbI_3$ ensures that the photogenerated carriers can travel long distances before they recombine and can be extracted efficiently. Recent theoretical and

experimental studies have shown that reasonable carrier mobility (μ) and excellent recombination lifetime (τ) are the reason behind long carrier diffusion-length. The reasonable carrier mobility arises from the small effective mass of holes and electrons, which are found to be quite balanced as well for $MAPbI_3$. This results in superior and ambipolar charge transport [37]. High intrinsic mobility also depends on the electron-phonon coupling. The weak coupling in $MAPbI_3$ helps the photogenerated carriers to quickly relax to band-edges, leading to high intrinsic mobilities [50, 51]. Despite that, the intrinsic carrier mobility of $MAPbI_3$ is modest (tens of cm^2/Vs) compared to high-quality inorganic PV materials such as GaAs or Si [37]. However, what separates $MAPbI_3$ from other PV materials is the carrier recombination lifetime. The lifetime of excited-state carriers in low-temperature processed $MAPbI_3$ (ranging from 100 ns to 15 µs) is comparable to that of high-quality GaAs. The average mobility and long carrier recombination lifetime lead to extremely long drift and diffusion lengths that are much longer than the light penetration depth. This explains excellent carrier collection in PSCs.

2.5.4 Benign Defects in $MAPbI_3$

The role of defects is very critical for thin-film photovoltaics, as the formation of defects is inevitable during low-temperature fabrication process. The nonradiative recombination and the carrier scattering which reduces the carrier recombination lifetime, is generally caused by the defects that create mid-bandgap states. Interestingly, grain boundaries defects and intrinsic point defects having low formation energy, do not create mid-bandgap states in $MAPbI_3$ and therefore can be considered as electronically benign [52]. Point defects that create mid-bandgap states, on the other hand, have high formation energy and are unlikely to form during normal synthesis conditions [37, 53]. The formation energies of the intrinsic defects in $MAPbI_3$ and their transition

levels are shown in Figure 2.6. In addition, neutral Schottky and Frenkel defects were also found to be in resonance with the bands, most likely due to the ionic nature of $MAPbI_3$ [53]. The "superior optoelectronic properties" of $MAPbI_3$ are often attributed to these excellent defect tolerant properties which arise from unusual valence band maximum (VBM) and conduction band minimum (CBM) characteristics. The CBM and VBM of $[PbI_6]^{4-}$ cluster (the building block of Pb-based halide perovskites) are composed of antibonding orbitals, resulting from the partially oxidized Pb^{2+} cation. The antibonding-type orbitals push the VBM energy up, resulting in resonant cation vacancies. On the other hand, relativistic spin-orbit interaction increases the width of the Pb(6*p*) conduction band. Therefore, any dangling bonds due to anion vacancies will appear as resonances within the conduction band [54]. Hence, the lifetime of the carriers remains so high in $MAPbI_3$ thin-film even after processing under low temperature and from a solution-based route.

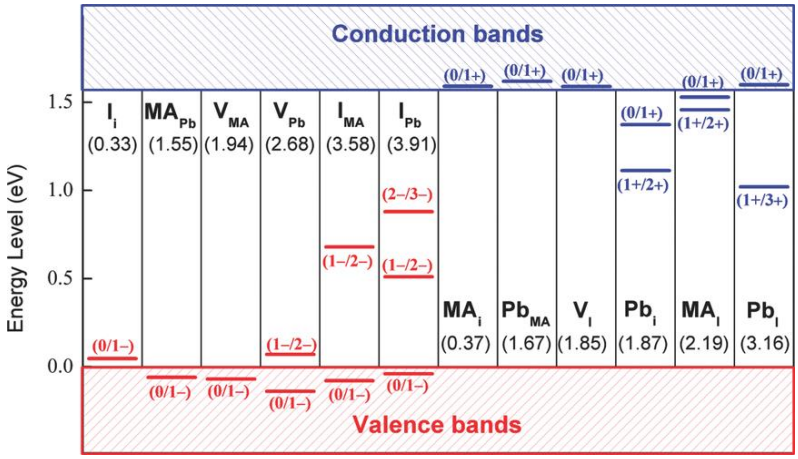

Figure 2.6: Transition energy levels of intrinsic donors and acceptors in $CH_3NH_3PbI_3$. The values in the parentheses indicate the formation energy of the respective neutral defects. MA stands for methylammonium (CH_3NH_3). Figure adapted from ref. [55].

2.6 Challenges in Perovskite Solar Cells

2.6.1 Instability of Perovskites

While the PCE is soaring to a record high, the easy-to-fabricate PSCs face the grandest challenge in commercialization as they are also easy-to-degraded. Long-term stability remains a significant issue in exploiting the full potential of solution-processed low-cost PSCs. Figure 2.7 shows the state-of-the-art PCE vs. lifetime of the PSCs. The highly efficient PSCs have lifetime around 1000 hrs, which is much shorter as compared to the lifetime of commercial Si PV. The best lifetime was obtained around 10000 hrs (1 year) but with much-reduced PCE (12%) [56]. Besides, the highly efficient devices must be fabricated in meticulous environments, and the efficiency drops instantly upon contact with the ambient atmosphere. The main reason for this degradation is the intrinsic instability of $MAPbI_3$ under various environmental factors, such as moisture, oxygen, UV radiation, and electrical and thermal stress [57-61]. In the presence of moisture/water, $MAPbI_3$ can quickly degrade into PbI_2 through a series of hydrated intermediate phases [62, 63]. While the exact mechanism and reaction kinetics are still being discussed, UV radiation, and oxygen speed up the reaction kinetics [64]. Moreover, $MAPbI_3$ also undergoes reversible structural changes from tetragonal to cubic at ~58 °C, which can affect both performance and long-term stability during operating conditions, which can reach 80 ℃ or higher in tropical environment. Thermal treatment could also lead to ionic migration and interdiffusion, leading to irreversible degradation [65].

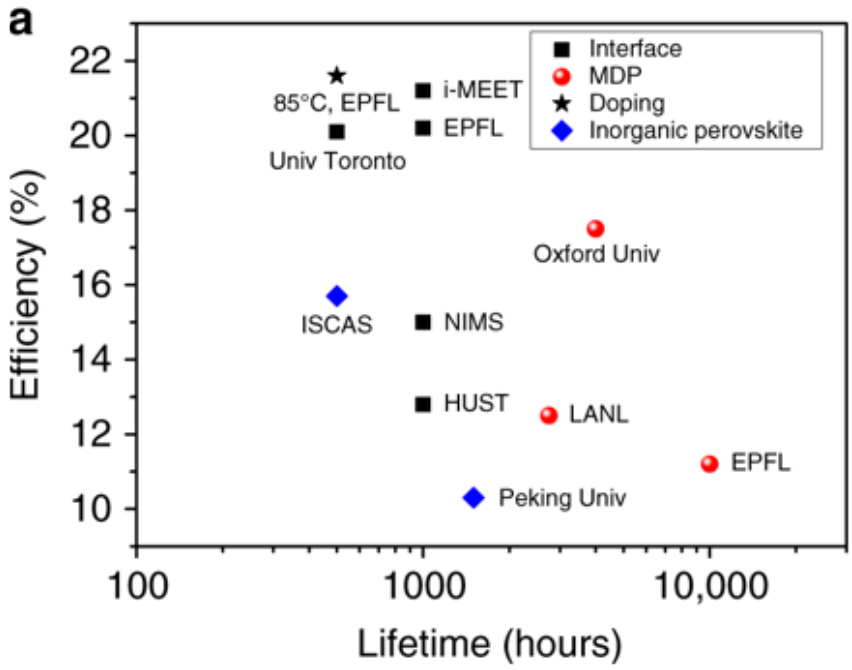

Figure 2.7: The state-of-the-art of PCE vs lifetime of PSCs. Composition and interface engineering remain two key aspect to improve the stability of PSCs (see ref. [66] for details) [66].

One way of circumventing this problem is through encapsulation schemes such as sealing the devices with hydrophobic polymer [67, 68], or utilizing triple layer mesoporous structure [24, 69], or using hydrophobic charge transport layers [70]. Interface degradation between ETL and the perovskite layer can be overcome by replacing TiO_2-based ETL which shows photocatalytic behavior under UV illumination. UV-stable ETL materials (such as $BaSnO_3$) or an interfacial layer (such as CsBr, CsI, Sb_2S_3 or Cl atoms) between the ETL and absorber layer have been demonstrated to improve the stability of PSCs [71-75]. Commonly used organic HTMs such as Spiro-OMeTAD, P3HT, and PTAA also suffer from moisture and thermal instability in their doped form, which can be prevented by substituting with inorganic HTMs such as CuI, CuSCN [76]. Triple mesoscopic perovskite structure has been demonstrated to

overcome the stability problem at the cost of less efficiency compared to the state-of-the-art perovskite solar cells [58, 69, 77].

The chemical stability of $MAPbI_3$, however, remains an open question. Efforts have been put forth to alleviate the degradation mechanism without deteriorating the optoelectronic properties. The use of mixed halides and/or the reduction of structural dimensionality are potential pathways; the removal of chemically labile organic cation is another effective way of achieving relatively stable perovskite materials. Noh, *et al.* [78] demonstrated that replacing iodide by bromide can improve overall device stability under light. Mixed iodide-chloride perovskite systems are also found to be more stable than $MAPbI_3$ [10, 13]. Later, Jiang, *et al.* [79] showed that partial replacement of iodine with thiocyanate anion (SCN^-) also improved the moisture stability. More recently, partial replacement of MA with a mixture of organic/inorganic cations showed remarkable stability under ambient atmosphere [80-82]. Apart from that, mixtures of 2D/3D perovskite (employing a larger organic cation) also exhibit better stability than pristine $MAPbI_3$, but with a low PCE compared to that of $MAPbI_3$ PSCs. While the stability has been boosted to a certain degree, it still falls well short of the strict prerequisites for long-term practical uses.

2.6.2 Toxicity of Lead

Despite the enormous success of Pb-based halide perovskites, the toxicity associated with Pb^{2+} cannot be ignored. Extensive investigations have reported the calamitous effect of only a few micrograms of Pb accumulated in the human body, especially in children [83, 84]. Lead is one of the most poisonous metals affecting almost all the organs in the human body. The presence of lead in the human body often remains undetected due to no visible symptoms. However, long-term exposure results in an adverse impact on cognitive abilities, bone,

tissues, various organs, nervous system; even long-term exposure of heavy lead levels linked to death [85]. Although a through life cycle assessment of PSCs is premature at this stage, the toxicity of heavy metals is indisputable. All the highly efficient PSCs contain more than 10% lead in weight which is much higher the regulation limit of heavy metals in consumer electronics [86, 87]. The European Union, for example, limits the maximum lead concentration to 0.1% in weight. Another significant issue with lead-based halide perovskites is their water solubility. Lead halide perovskites dissolve readily in water, which can eventually accumulate in the food chain and therefore end up into the human body.

2.7 Lead-free Perovskite Solar Cell

2.7.1 Homovalent Substitutions of Pb

Concern over the potential adverse environmental impact of Pb-based halide perovskites forced us to search for a suitable replacement of Pb in perovskite structure. Rationally, any element with +2 oxidation state can replace lead in perovskite structure. However, theoretical calculation revealed that apart from Sn and Ge, other divalent cations do not form perovskite structure, or the resultant bandgap is too high for PV applications [88]. Hence, Sn and Ge remain the most interesting because of their similar electronic configuration as Pb. The study of Sn-based halide perovskites was also started in the 1990s when Mitzi, *et al.* [6] showed conducting behavior of $CH_3NH_3SnI_3$. After the phenomenal success of Pb-based halide perovskites in PV, the Sn-based halide perovskites received renewed interests. In one of the earlier report, it was demonstrated that oxidation of Sn^{2+} to Sn^{4+} in the presence of oxygen leads to self-doping in the thin-films and can behave differently depending upon the fabrication route[89]. Eventually, the first PV device with Sn-based halide perovskite ($CH_3NH_3SnI_{3-x}Br_x$) resulted in 5.73% PCE with J_{SC} of 16.30 mA cm^{-2}, and V_{OC} of 0.68 V in planar configuration, albeit with

extremely poor stability in ambient atmosphere [90]. Within same time, *Noel, et al.* [91] reported $CH_3NH_3SnI_3$ based compounds with 6.4% PCE with an impressive V_{OC} of 0.88 V. As compared to $CH_3NH_3PbI_3$ (bandgap of 1.55 eV), the Sn-analogue ($CH_3NH_3SnI_3$) has smaller bandgap (1.3 eV), which can also be engineered through chemical substitution of halogen atom [92]. However, the solar cell devices degraded within 24 hours after exposing to the ambient atmosphere. In a similar approach, Kumar, *et al.* [93] demonstrated $CsSnI_3$-based thin-films suffered from severe defects formation due to self-oxidations. They demonstrated that solar cell efficiency could be increased from merely 0.0003% to ~2% with the addition of SnF_2 which reduces the intrinsic defect concentration. Unfortunately, the propensity for Sn^{2+} to undergo oxidation to Sn^{4+} has proved challenging to overcome and results in poor morphology and fast degradation. Later, a two-step synthesis of $MASnI_3$ was proved to be useful to retard the oxidation of Sn^{2+}, however no device data were reported [94]. A record efficiency of 7.7% was later obtained when thin-films of $MASnI_3$ was deposited by pulsed laser deposition technique [95]. Nevertheless, the PCE of Sn-based halide perovskite still remains low compared to Pb-based halide perovskites, and extreme instability in ambient atmosphere makes it more difficult for PV applications. The Ge-based halide perovskites were also received much interest initially as a Pd-free alternative [88]. However, poor PCE (< 1%) and atmospheric instability are still the most significant challenges to overcome. Apart from Sn and Ge, other divalent metals do not exhibit perovskite crystal structure as they lie outside of the stability region in (t, μ) map. However, metastable phases can be formed by employing suitable A-site cations. Recent high-throughput calculation predicted Mg-based iodide perovskites as lead-free perovskite compound for PV applications [96]. Figure 2.7 shows the calculated bandgap values of lead-free perovskites employing different divalent cation as *B*-site cation. However, detailed experimental investigations are still lacking to rule out the divalent cations.

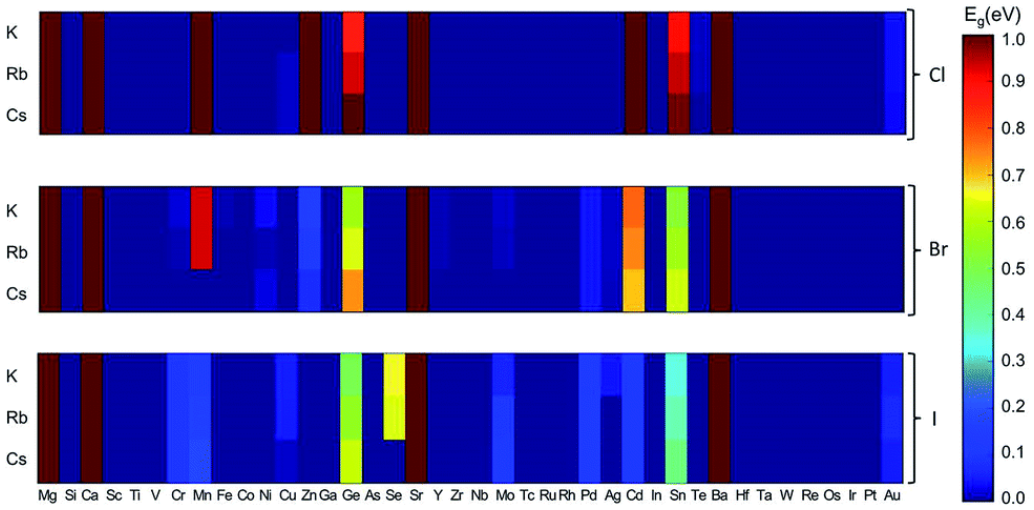

Figure 2.8: Calculated bandgaps of AMX_3 halide perovskites (*A*: K, Rb, Cs; *M* is the divalent cations on *x*-axis; *X*: Cl, Br, I). Figure adapted from ref. [88].

2.7.2 Heterovalent Substitutions of Pb

The group 13 and 15 elements from periodic table shares the similar electronic structure of Pb but comes with different oxidation state, which prevents the formation of the conventional perovskite structure. Nevertheless, high stability, similar electronic structure, and low toxicity make them excellent candidates for the replacement of Pb.

A. Bi-based halide perovskite

Bi-based halide perovskites have long been studied for their rich variety of structural composition [97-99], but most of works were limited in ferroelectricity, phase transformation, and non-linear optical properties. Recently, Bi-perovskites of the family of $A_3Bi_2X_9$ (A = alkali/organic cation, X = halogen anion) has received renewed attention among the photovoltaic community as lead-free absorber materials. Lehner, et al. [100] examined the crystal, and electronic structure of $A_3Bi_2I_9$ (A = K^+, Rb^+, Cs^+) compounds both experimentally and computationally. They found that the effect of the cations

on the optical bandgap is negligible. All three cations exhibit an optical bandgap of about 2 eV. Later, Park, *et al.* [101] reported $MA_2Bi_2I_9$ (MA = Methylammonium) and $Cs_3Bi_2I_9$ based solar cell devices with efficiencies 0.12% and ~1% in mesoscopic solar cell architecture. Shortly after that, Lyu, *et al.* [102] also reported $MA_3Bi_2I_9$ based perovskite solar cell with efficiency of 0.19% in planar structure architecture. They found that the carrier density in $MA_3Bi_2I_9$ is around 10^{16} cm^{-3}, which is nearly seven orders of magnitude higher than $MAPbI_3$ thin-films. Although Bi has a similar electronic configuration to that of Pb, the devices based on $Cs_3Bi_2I_9$ do not perform very well as compared to $MAPbI_3$. However, the solar cell devices were quite stable and performed without any hysteresis, demonstrating distinct advantages over Pb- and Sn-based PSCs. Recently, Hoye, *et al.* [103] indicated that vapor processing films show better PL performance as compared to the solution processed ones. They pointed out that non-radiative recombination, to be the limit for the performance of the $MA_3Bi_2I_9$ thin-films. Interestingly, $MA_3Bi_2I_9$-based PSCs prepared on anatase TiO_2 mesoporous layer showed better performances than those prepared on a planar structure or brookite TiO_2 mesoporous layer [104]. This illustrates that additional optimizations are needed on device level to improve the performance of Bi-based perovskites further.

B. Sb-based Halide Perovskites

Like Bi-based halide perovskites, Sb-based halide perovskites also exhibit low dimensional structure, which can be modified by appropriate A-site cations. The first report on $Cs_3Sb_2I_9$ as an absorber material in mesoscopic solar cell configuration yielded <1% PCE, but thin-films exhibited excellent ambient stability [105]. Later, replacing Cs^+ with smaller cations such as Rb^+ and NH_4^+ resulted in improved PV performance and better control over crystal structure [106, 107]. Recently, Boopathi, *et al.* [108] reported more than 2% PCE with $MA_3Sb_2I_9$ with a planar structure by improving the thin-film morphology with

HI addition in the precursor solution. Although the initial results are quite impressive with Sb-based halide perovskites, the intrinsic disorder in the crystal structure appears to be a significant obstacle in achieving high PCE.

C. Halide-based Double Perovskites

Since Bi- and Sb-based halide perovskites exhibit low-dimensionality, an alternative approach would be an addition of monovalent cation and trivalent cation together to maintain the 3D perovskite structure. This results in double perovskite structure with ordered B-site cations and a general formula of $A_2B^{I}B^{III}X_6$ (Figure 2.8). Although double perovskites are quite well-known in the field of oxide perovskites, synthesis of halide double perovskites appears to be a significant hurdle. Slavney, et al. [109] were first to synthesize $Cs_2AgBiBr_6$ halide double perovskite, which shows more than 700 ns carrier recombination lifetime and remarkable stability. Recent reports also recorded promising PCE using $Cs_2AgBiBr_6$ in both mesoscopic and planar architecture [110-112]. However, the optical bandgap of $Cs_2AgBiBr_6$ is above 2 eV which restricts its usage as a highly efficient single junction solar cells. Recently, first principle calculations have been extensively used to predict suitable bandgap PV materials based on double perovskite crystal structure [72, 113, 114]. Figure 2.8 shows the recent work from Zhao, *et al.* [115], highlighting the promising double halide perovskites based on DFT calculations. Nevertheless, more experimental works are needed to find suitable synthesis route and thin-film formation for their applications in PV [116-118].

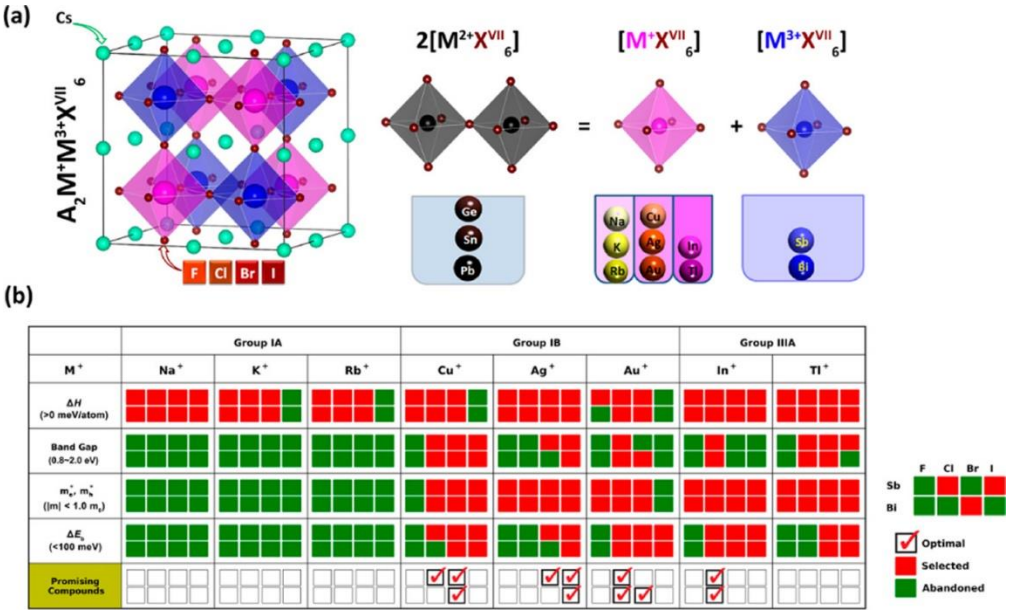

Figure 2.9: Screening of lead-free halide double perovskites. (a) Crystal structure of $A_2M^+M^{3+}X^{VII}X_6$ double perovskites which forms by cation transmutation (right panel). (b) Results of screening process by considering the following properties: decomposition enthalpy (ΔH), band gap, carriers' effective masses (m_e*, m_h*), and exciton binding energy (ΔE_b). The optimal compositions are marked with red checks. Figure adapted from ref. [115].

2.8 Conclusions

The direct bandgap, high absorption coefficient in visible wavelength, reasonable transport properties, defect tolerant nature, long carrier diffusion length and recombination lifetime are the most sought-after properties for a high-quality PV semiconductor. In this aspect, lead-based halide perovskites especially $MAPbI_3$ triumphs over all other thin-film PV materials as these excellent properties can be achieved in $MAPbI_3$ even with inexpensive solution processable fabrication route. Within three years of their discovery as PV semiconductor, Pb-based halides perovskite became the most promising third-generation PV technology. However, there are three crucial issues with PSC before it becomes a commercial success: long term stability, large scale

fabrication, and toxicity. Although research into stability and large-scale production has gained positive momentum recently, the toxicity of Pb remains an open issue. One viable solution to eliminate Pb hazards is to replace Pb completely with non-toxic metal cations. Based on current understanding of Pb-based perovskites and coupled with high throughput calculations, various homovalent and heterovalent alternatives have been proposed, most notably Sn-based halide perovskites, Bi- and Sb-based halide perovskites and double perovskites. However, there are numerous difficulties must be tended to before these new materials become competitive alternatives.

References

[1] C. Li, X. Lu, W. Ding, L. Feng, Y. Gao, and Z. Guo, "Formability of ABX_3 (X = F, Cl, Br, I) halide perovskites," *Acta Crysrallogr. B*, vol. 64, pp. 702-707, 2008.

[2] C. Li, K. C. K. Soh, and P. Wu, "Formability of ABO_3 perovskites," *J. Alloys Compd.*, vol. 372, pp. 40-48, 2004/06/09/ 2004.

[3] M. A. Peña and J. L. G. Fierro, "Chemical Structures and Performance of Perovskite Oxides," *Chem. Rev.*, vol. 101, pp. 1981-2018, 2001/07/01 2001.

[4] Q. Sun and W.-J. Yin, "Thermodynamic Stability Trend of Cubic Perovskites," *J. Am. Chem. Soc.*, vol. 139, pp. 14905-14908, 2017/10/25 2017.

[5] D. B. Mitzi, C. A. Feild, W. T. A. Harrison, and A. M. Guloy, "Conducting tin halides with a layered organic-based perovskite structure," *Nature*, vol. 369, pp. 467-469, 06/09/print 1994.

[6] D. B. Mitzi, C. A. Feild, Z. Schlesinger, and R. B. Laibowitz, "Transport, Optical, and Magnetic Properties of the Conducting Halide Perovskite $CH_3NH_3SnI_3$," *J. Solid State Chem.*, vol. 114, pp. 159-163, 1// 1995.

[7] A. Kojima, K. Teshima, Y. Shirai, and T. Miyasaka, "Organometal Halide Perovskites as Visible-Light Sensitizers for Photovoltaic Cells," *J. Am. Chem. Soc.*, vol. 131, pp. 6050-6051, 2009/05/06 2009.

[8] J.-H. Im, C.-R. Lee, J.-W. Lee, S.-W. Park, and N.-G. Park, "6.5% efficient perovskite quantum-dot-sensitized solar cell," *Nanoscale*, vol. 3, pp. 4088-4093, 2011.

[9] H.-S. Kim, C.-R. Lee, J.-H. Im, K.-B. Lee, T. Moehl, A. Marchioro, *et al.*, "Lead Iodide Perovskite Sensitized All-Solid-State Submicron Thin Film Mesoscopic Solar Cell with Efficiency Exceeding 9%," *Scientific Reports*, vol. 2, p. 591, 08/21/online 2012.

[10] M. M. Lee, J. Teuscher, T. Miyasaka, T. N. Murakami, and H. J. Snaith, "Efficient Hybrid Solar Cells Based on Meso-Superstructured Organometal Halide Perovskites," *Science,* vol. 338, pp. 643-647, 2012-11-02 00:00:00 2012.

[11] J. H. Heo, S. H. Im, J. H. Noh, T. N. Mandal, C.-S. Lim, J. A. Chang, *et al.*, "Efficient inorganic–organic hybrid heterojunction solar cells containing perovskite compound and polymeric hole conductors," *Nat. Photonics,* vol. 7, p. 486, 05/05/online 2013.

[12] J. Burschka, N. Pellet, S.-J. Moon, R. Humphry-Baker, P. Gao, M. K. Nazeeruddin, *et al.*, "Sequential deposition as a route to high-performance perovskite-sensitized solar cells," *Nature,* vol. 499, p. 316, 07/10/online 2013.

[13] M. Liu, M. B. Johnston, and H. J. Snaith, "Efficient planar heterojunction perovskite solar cells by vapour deposition," *Nature,* vol. 501, p. 395, 09/11/online 2013.

[14] N. J. Jeon, J. H. Noh, Y. C. Kim, W. S. Yang, S. Ryu, and S. I. Seok, "Solvent engineering for high-performance inorganic–organic hybrid perovskite solar cells," *Nat. Mater.,* vol. 13, p. 897, 07/06/online 2014.

[15] N. J. Jeon, J. H. Noh, W. S. Yang, Y. C. Kim, S. Ryu, J. Seo, *et al.*, "Compositional engineering of perovskite materials for high-performance solar cells," *Nature,* vol. 517, p. 476, 01/07/online 2015.

[16] S.-G. Li, K.-J. Jiang, M.-J. Su, X.-P. Cui, J.-H. Huang, Q.-Q. Zhang, *et al.*, "Inkjet printing of $CH_3NH_3PbI_3$ on a mesoscopic TiO_2 film for highly efficient perovskite solar cells," *J. Mater. Chem. A,* vol. 3, pp. 9092-9097, 2015.

[17] K. Cao, Z. Zuo, J. Cui, Y. Shen, T. Moehl, S. M. Zakeeruddin, *et al.*, "Efficient screen printed perovskite solar cells based on mesoscopic TiO_2/Al_2O_3/NiO/carbon architecture," *Nano Energy,* vol. 17, pp. 171-179, 2015/10/01/ 2015.

[18] *Chart* of Best Research-Cell Efficiencies Provided by National Renewable Energy Laboratory. http://www.nrel.gov/pv/assets/images/efficiency_chart.jpg

[19] E. H. Anaraki, A. Kermanpur, L. Steier, K. Domanski, T. Matsui, W. Tress, *et al.*, "Highly efficient and stable planar perovskite solar cells by solution-processed tin oxide," *Energy Environ. Sci.*, vol. 9, pp. 3128-3134, 2016.

[20] G. E. Eperon, T. Leijtens, K. A. Bush, R. Prasanna, T. Green, J. T.-W. Wang, *et al.*, "Perovskite-perovskite tandem photovoltaics with optimized band gaps," *Science*, vol. 354, pp. 861-865, 2016.

[21] J. Ávila, C. Momblona, P. Boix, M. Sessolo, M. Anaya, G. Lozano, *et al.*, "High voltage vacuum-deposited $CH_3NH_3PbI_3$–$CH_3NH_3PbI_3$ tandem solar cells," *Energy Environ. Sci.*, vol. 11, pp. 3292-3297, 2018.

[22] T. Leijtens, K. A. Bush, R. Prasanna, and M. D. McGehee, "Opportunities and challenges for tandem solar cells using metal halide perovskite semiconductors," *Nat. Energy*, vol. 3, pp. 828-838, 2018/10/01 2018.

[23] Z. Ku, Y. Rong, M. Xu, T. Liu, and H. Han, "Full Printable Processed Mesoscopic $CH_3NH_3PbI_3/TiO_2$ Heterojunction Solar Cells with Carbon Counter Electrode," *Sci. Rep.*, vol. 3, p. 3132, 11/04/online 2013.

[24] A. Mei, X. Li, L. Liu, Z. Ku, T. Liu, Y. Rong, *et al.*, "A hole-conductor–free, fully printable mesoscopic perovskite solar cell with high stability," *Science*, vol. 345, pp. 295-298, 2014.

[25] J. Desilvestro, M. Graetzel, L. Kavan, J. Moser, and J. Augustynski, "Highly efficient sensitization of titanium dioxide," *J. Am. Chem. Soc.*, vol. 107, pp. 2988-2990, 1985/05/01 1985.

[26] P. Gao, M. Gratzel, and M. K. Nazeeruddin, "Organohalide lead perovskites for photovoltaic applications," *Energy Environ. Sci.*, vol. 7, pp. 2448-2463, 2014.

[27] A. Marchioro, J. Teuscher, D. Friedrich, M. Kunst, R. van de Krol, T. Moehl, *et al.*, "Unravelling the mechanism of photoinduced charge transfer processes in lead iodide perovskite solar cells," *Nat. Photonics*, vol. 8, p. 250, 01/19/online 2014.

[28] L. Etgar, P. Gao, Z. Xue, Q. Peng, A. K. Chandiran, B. Liu, *et al.*, "Mesoscopic $CH_3NH_3PbI_3/TiO_2$ Heterojunction Solar Cells," *J. Am. Chem. Soc.*, vol. 134, pp. 17396-17399, 2012/10/24 2012.

[29] W. A. Laban and L. Etgar, "Depleted hole conductor-free lead halide iodide heterojunction solar cells," *Energy Environ. Sci.*, vol. 6, pp. 3249-3253, 2013.

[30] G. Xing, N. Mathews, S. Sun, S. S. Lim, Y. M. Lam, M. Grätzel, *et al.*, "Long-Range Balanced Electron- and Hole-Transport Lengths in Organic-Inorganic $CH_3NH_3PbI_3$," *Science*, vol. 342, pp. 344-347, 2013-10-18 00:00:00 2013.

[31] G. Giorgi, J.-I. Fujisawa, H. Segawa, and K. Yamashita, "Small Photocarrier Effective Masses Featuring Ambipolar Transport in Methylammonium Lead Iodide Perovskite: A Density Functional Analysis," *J. Phys. Chem. Lett.*, vol. 4, pp. 4213-4216, 2013/12/19 2013.

[32] M. Liu, M. B. Johnston, and H. J. Snaith, "Efficient planar heterojunction perovskite solar cells by vapour deposition," *Nature*, vol. 501, pp. 395-398, 2013.

[33] O. Malinkiewicz, A. Yella, Y. H. Lee, G. M. Espallargas, M. Graetzel, M. K. Nazeeruddin, *et al.*, "Perovskite solar cells employing organic charge-transport layers," *Nat. Photonics*, vol. 8, pp. 128-132, 02//print 2014.

[34] N.-G. Park, M. Grätzel, T. Miyasaka, K. Zhu, and K. Emery, "Towards stable and commercially available perovskite solar cells," *Nat. Energy*, vol. 1, p. 16152, 10/17/online 2016.

[35] M. R. Filip, G. Volonakis, and F. Giustino, "Hybrid Halide Perovskites: Fundamental Theory and Materials Design," in *Handbook of Materials Modeling: Applications: Current and Emerging Materials*, W. Andreoni and S. Yip, Eds., ed Cham: Springer International Publishing, 2018, pp. 1-30.

[36] J. Huang, Y. Yuan, Y. Shao, and Y. Yan, "Understanding the physical properties of hybrid perovskites for photovoltaic applications," *Nature Reviews Materials*, vol. 2, p. 17042, 07/04/online 2017.

[37] W.-J. Yin, T. Shi, and Y. Yan, "Superior Photovoltaic Properties of Lead Halide Perovskites: Insights from First-Principles Theory," *J. Phys. Chem. C*, vol. 119, pp. 5253-5264, 2015/03/12 2015.

[38] A. Filippetti, P. Delugas, and A. Mattoni, "Radiative Recombination and Photoconversion of Methylammonium Lead Iodide Perovskite by First Principles: Properties of an Inorganic Semiconductor within a Hybrid Body," *J. Phys. Chem. C*, vol. 118, pp. 24843-24853, 2014/10/30 2014.

[39] M. Shirayama, H. Kadowaki, T. Miyadera, T. Sugita, M. Tamakoshi, M. Kato, *et al.*, "Optical Transitions in Hybrid Perovskite Solar Cells: Ellipsometry, Density Functional Theory, and Quantum Efficiency Analyses for $CH_3NH_3PbI_3$," *Phys. Rev. Appl.*, vol. 5, p. 014012, 01/27/ 2016.

[40] E. T. Hoke, D. J. Slotcavage, E. R. Dohner, A. R. Bowring, H. I. Karunadasa, and M. D. McGehee, "Reversible photo-induced trap formation in mixed-halide hybrid perovskites for photovoltaics," *Chem. Sci.*, vol. 6, pp. 613-617, 2015.

[41] N. C. Giebink, G. P. Wiederrecht, M. R. Wasielewski, and S. R. Forrest, "Thermodynamic efficiency limit of excitonic solar cells," *Phys. Rev. B*, vol. 83, p. 195326, 05/31/ 2011.

[42] Q. Lin, A. Armin, R. C. R. Nagiri, P. L. Burn, and P. Meredith, "Electro-optics of perovskite solar cells," *Nat. Photonics,* vol. 9, p. 106, 12/01/online 2014.

[43] V. D'Innocenzo, G. Grancini, M. J. P. Alcocer, A. R. S. Kandada, S. D. Stranks, M. M. Lee, *et al.*, "Excitons versus free charges in organo-lead tri-halide perovskites," *Nat. Commun.,* vol. 5, p. 3586, 04/08/online 2014.

[44] M. Hirasawa, T. Ishihara, T. Goto, K. Uchida, and N. Miura, "Magnetoabsorption of the lowest exciton in perovskite-type compound (CH_3NH_3)PbI_3," *Physica B,* vol. 201, pp. 427-430, 1994/07/01/ 1994.

[45] K. Tanaka, T. Takahashi, T. Ban, T. Kondo, K. Uchida, and N. Miura, "Comparative study on the excitons in lead-halide-based perovskite-type crystals $CH_3NH_3PbBr_3$ $CH_3NH_3PbI_3$," *Solid State Commun.,* vol. 127, pp. 619-623, 2003/09/01/ 2003.

[46] M. Saba, M. Cadelano, D. Marongiu, F. Chen, V. Sarritzu, N. Sestu, *et al.*, "Correlated electron–hole plasma in organometal perovskites," *Nat. Commun.*, vol. 5, p. 5049, 09/30/online 2014.

[47] C. S. Ponseca, T. J. Savenije, M. Abdellah, K. Zheng, A. Yartsev, T. Pascher, *et al.*, "Organometal Halide Perovskite Solar Cell Materials Rationalized: Ultrafast Charge Generation, High and Microsecond-Long Balanced Mobilities, and Slow Recombination," *J. Am. Chem. Soc.*, vol. 136, pp. 5189-5192, 2014/04/09 2014.

[48] Q. Dong, Y. Fang, Y. Shao, P. Mulligan, J. Qiu, L. Cao, *et al.*, "Electron-hole diffusion lengths > 175 μm in solution-grown $CH_3NH_3PbI_3$ single crystals," *Science,* vol. 347, pp. 967-970, 2015.

[49] T. C. Sum and N. Mathews, *Halide Perovskites: Photovoltaics, Light Emitting Devices, and Beyond*: Wiley, 2019.

[50] M. B. Johnston and L. M. Herz, "Hybrid Perovskites for Photovoltaics: Charge-Carrier Recombination, Diffusion, and Radiative Efficiencies," *Acc. Chem. Res.*, vol. 49, pp. 146-154, 2016/01/19 2016.

[51] T. Zhao, W. Shi, J. Xi, D. Wang, and Z. Shuai, "Intrinsic and Extrinsic Charge Transport in $CH_3NH_3PbI_3$ Perovskites Predicted from First-Principles," *Sci. Rep.*, vol. 6, p. 19968, 01/29/online 2016.

[52] W.-J. Yin, H. Chen, T. Shi, S.-H. Wei, and Y. Yan, "Origin of High Electronic Quality in Structurally Disordered $CH_3NH_3PbI_3$ and the Passivation Effect of Cl and O at Grain Boundaries," *Adv, Electron. Mater.*, vol. 1, p. 1500044, 2015.

[53] J. Kim, S.-H. Lee, J. H. Lee, and K.-H. Hong, "The Role of Intrinsic Defects in Methylammonium Lead Iodide Perovskite," *J. Phys. Chem. Lett.*, vol. 5, pp. 1312-1317, 2014/04/17 2014.

[54] R. E. Brandt, V. Stevanović, D. S. Ginley, and T. Buonassisi, "Identifying defect-tolerant semiconductors with high minority-carrier lifetimes: beyond hybrid lead halide perovskites," *MRS Communications*, vol. 5, pp. 265-275, 2015.

[55] W.-J. Yin, T. Shi, and Y. Yan, "Unique Properties of Halide Perovskites as Possible Origins of the Superior Solar Cell Performance," *Adv. Mater.*, vol. 26, pp. 4653-4658, 2014.

[56] G. Grancini, C. Roldán-Carmona, I. Zimmermann, E. Mosconi, X. Lee, D. Martineau, *et al.*, "One-Year stable perovskite solar cells by 2D/3D interface engineering," *Nat. Commun.*, vol. 8, p. 15684, 06/01/online 2017.

[57] N. Aristidou, C. Eames, I. Sanchez-Molina, X. Bu, J. Kosco, M. S. Islam, *et al.*, "Fast oxygen diffusion and iodide defects mediate oxygen-induced degradation of perovskite solar cells," *Nat. Commun.*, vol. 8, p. 15218, 05/11/online 2017.

[58] N. Aristidou, I. Sanchez-Molina, T. Chotchuangchutchaval, M. Brown, L. Martinez, T. Rath, *et al.*, "The Role of Oxygen in the Degradation of Methylammonium Lead Trihalide Perovskite Photoactive Layers," *Angew. Chem. Int. Ed.*, vol. 54, pp. 8208-8212, 2015.

[59] W. Nie, J.-C. Blancon, A. J. Neukirch, K. Appavoo, H. Tsai, M. Chhowalla, *et al.*, "Light-activated photocurrent degradation and self-healing in perovskite solar cells," *Nat. Commun.*, vol. 7, p. 11574, 05/16/online 2016.

[60] Y. Han, S. Meyer, Y. Dkhissi, K. Weber, J. M. Pringle, U. Bach, *et al.*, "Degradation observations of encapsulated planar $CH_3NH_3PbI_3$ perovskite solar cells at high temperatures and humidity," *J. Mater. Chem. A*, vol. 3, pp. 8139-8147, 2015.

[61] A. J. Pearson, G. E. Eperon, P. E. Hopkinson, S. N. Habisreutinger, J. T.-W. Wang, H. J. Snaith, *et al.*, "Oxygen Degradation in Mesoporous $Al_2O_3/CH_3NH_3PbI_{3-x}Cl_x$ Perovskite Solar Cells: Kinetics and Mechanisms," *Adv. Energy Mater.*, vol. 6, p. 1600014, 2016.

[62] J. M. Frost, K. T. Butler, F. Brivio, C. H. Hendon, M. van Schilfgaarde, and A. Walsh, "Atomistic Origins of High-Performance in Hybrid Halide Perovskite Solar Cells," *Nano Lett.*, vol. 14, pp. 2584-2590, 2014/05/14 2014.

[63] A. M. A. Leguy, Y. Hu, M. Campoy-Quiles, M. I. Alonso, O. J. Weber, P. Azarhoosh, *et al.*, "Reversible Hydration of $CH_3NH_3PbI_3$ in Films, Single Crystals, and Solar Cells," *Chem. Mater.*, vol. 27, pp. 3397-3407, 2015/05/12 2015.

[64] G. Niu, W. Li, F. Meng, L. Wang, H. Dong, and Y. Qiu, "Study on the stability of $CH_3NH_3PbI_3$ films and the effect of post-modification by aluminum oxide in all-solid-state hybrid solar cells," *J. Mater. Chem. A*, vol. 2, pp. 705-710, 2014.

[65] J. Berry, T. Buonassisi, D. A. Egger, G. Hodes, L. Kronik, Y.-L. Loo, *et al.*, "Hybrid Organic–Inorganic Perovskites (HOIPs): Opportunities and Challenges," *Adv. Mater.*, vol. 27, pp. 5102-5112, 2015.

[66] L. Meng, J. You, and Y. Yang, "Addressing the stability issue of perovskite solar cells for commercial applications," *Nat. Commun.*, vol. 9, p. 5265, 2018/12/10 2018.

[67] F. Bella, G. Griffini, J.-P. Correa-Baena, G. Saracco, M. Grätzel, A. Hagfeldt, *et al.*, "Improving efficiency and stability of perovskite solar cells with photocurable fluoropolymers," *Science*, p. aah4046, 2016.

[68] N. A. Manshor, Q. Wali, K. K. Wong, S. K. Muzakir, A. Fakharuddin, L. Schmidt-Mende, *et al.*, "Humidity versus photo-stability of metal halide perovskite films in a polymer matrix," *PCCP*, vol. 18, pp. 21629-21639, 2016.

[69] Y. Hu, S. Si, A. Mei, Y. Rong, H. Liu, X. Li, *et al.*, "Stable Large-Area (10 × 10 cm2) Printable Mesoscopic Perovskite Module Exceeding 10% Efficiency," *Solar RRL*, vol. 1, p. 1600019, 2017.

[70] Z. Zhu, D. Zhao, C.-C. Chueh, X. Shi, Z. Li, and A. K. Y. Jen, "Highly Efficient and Stable Perovskite Solar Cells Enabled by All-Crosslinked Charge-Transporting Layers," *Joule*, vol. 2, pp. 168-183, 2018/01/17/ 2018.

[71] S. S. Shin, E. J. Yeom, W. S. Yang, S. Hur, M. G. Kim, J. Im, *et al.*, "Colloidally prepared La-doped $BaSnO_3$ electrodes for efficient, photostable perovskite solar cells," *Science*, 2017.

[72] H. Tan, A. Jain, O. Voznyy, X. Lan, F. P. García de Arquer, J. Z. Fan, *et al.*, "Efficient and stable solution-processed planar perovskite solar cells via contact passivation," *Science*, 2017.

[73] S. Ito, S. Tanaka, K. Manabe, and H. Nishino, "Effects of Surface Blocking Layer of Sb_2S_3 on Nanocrystalline TiO_2 for $CH_3NH_3PbI_3$

Perovskite Solar Cells," *J. Phys. Chem. C,* vol. 118, pp. 16995-17000, 2014/07/31 2014.

[74] F. Han, J. Luo, B. Zhao, Z. Wan, R. Wang, and C. Jia, "Cesium Iodide Interface Modification for High Efficiency, High Stability and Low Hysteresis Perovskite Solar Cells," *Electrochim. Acta,* vol. 236, pp. 122-130, 2017/05/10/ 2017.

[75] D. Zhao, Z. Zhu, M.-Y. Kuo, C.-C. Chueh, and A. K.-Y. Jen, "Hexaazatrinaphthylene Derivatives: Efficient Electron-Transporting Materials with Tunable Energy Levels for Inverted Perovskite Solar Cells," *Angew. Chem. Int. Ed.,* vol. 55, pp. 8999-9003, 2016.

[76] J. You, L. Meng, T.-B. Song, T.-F. Guo, Y. Yang, W.-H. Chang, *et al.*, "Improved air stability of perovskite solar cells via solution-processed metal oxide transport layers," *Nat. Nanotechnol.,* vol. 11, p. 75, 10/12/online 2015.

[77] A. K. Baranwal, S. Kanaya, T. A. N. Peiris, G. Mizuta, T. Nishina, H. Kanda, *et al.*, "100 °C Thermal Stability of Printable Perovskite Solar Cells Using Porous Carbon Counter Electrodes," *ChemSusChem,* vol. 9, pp. 2604-2608, 2016.

[78] J. H. Noh, S. H. Im, J. H. Heo, T. N. Mandal, and S. I. Seok, "Chemical Management for Colorful, Efficient, and Stable Inorganic–Organic Hybrid Nanostructured Solar Cells," *Nano Lett.,* vol. 13, pp. 1764-1769, 2013/04/10 2013.

[79] Q. Jiang, D. Rebollar, J. Gong, E. L. Piacentino, C. Zheng, and T. Xu, "Pseudohalide-Induced Moisture Tolerance in Perovskite $CH_3NH_3Pb(SCN)_2I$ Thin Films," *Angew. Chem.,* vol. 127, pp. 7727-7730, 2015.

[80] Z. Wang, D. P. McMeekin, N. Sakai, S. van Reenen, K. Wojciechowski, J. B. Patel, *et al.*, "Efficient and Air-Stable Mixed-Cation Lead Mixed-

Halide Perovskite Solar Cells with n-Doped Organic Electron Extraction Layers," *Adv. Mater.,* vol. 29, p. 1604186, 2017.

[81] M. Saliba, T. Matsui, J.-Y. Seo, K. Domanski, J.-P. Correa-Baena, M. K. Nazeeruddin, *et al.,* "Cesium-containing triple cation perovskite solar cells: improved stability, reproducibility and high efficiency," *Energy Environ. Sci.,* vol. 9, pp. 1989-1997, 2016.

[82] M. Saliba, T. Matsui, K. Domanski, J.-Y. Seo, A. Ummadisingu, S. M. Zakeeruddin, *et al.,* "Incorporation of rubidium cations into perovskite solar cells improves photovoltaic performance," *Science,* vol. 354, pp. 206-209, 2016.

[83] Q. Zhang, F. Hao, J. Li, Y. Zhou, Y. Wei, and H. Lin, "Perovskite solar cells: must lead be replaced – and can it be done?," *Sci. Technol. Adv. Mater.,* vol. 19, pp. 425-442, 2018/12/31 2018.

[84] G. Flora, D. Gupta, and A. Tiwari, "Toxicity of lead: a review with recent updates," *Interdisciplinary Toxicology,* vol. 5, pp. 47-58, 2012.

[85] A. L. Wani, A. Ara, and J. A. Usmani, "Lead toxicity: a review," *Interdisciplinary toxicology,* vol. 8, pp. 55-64, 2015.

[86] M. Saliba, J.-P. Correa-Baena, M. Grätzel, A. Hagfeldt, and A. Abate, "Perovskite Solar Cells: From the Atomic Level to Film Quality and Device Performance," *Angew. Chem. Int. Ed.,* vol. 57, pp. 2554-2569, 2018.

[87] A. Abate, "Perovskite Solar Cells Go Lead Free," *Joule,* vol. 1, pp. 659-664, 2017/12/20/ 2017.

[88] T. Krishnamoorthy, H. Ding, C. Yan, W. L. Leong, T. Baikie, Z. Zhang, *et al.,* "Lead-free germanium iodide perovskite materials for photovoltaic applications," *J. Mater. Chem. A,* vol. 3, pp. 23829-23832, 2015.

[89] C. C. Stoumpos, C. D. Malliakas, and M. G. Kanatzidis, "Semiconducting Tin and Lead Iodide Perovskites with Organic Cations:

Phase Transitions, High Mobilities, and Near-Infrared Photoluminescent Properties," *Inorg. Chem.*, vol. 52, pp. 9019-9038, 2013/08/05 2013.

[90] F. Hao, C. C. Stoumpos, D. H. Cao, R. P. Chang, and M. G. Kanatzidis, "Lead-free solid-state organic-inorganic halide perovskite solar cells," *Nat. Photonics*, vol. 8, pp. 489-494, 2014.

[91] N. K. Noel, S. D. Stranks, A. Abate, C. Wehrenfennig, S. Guarnera, A.-A. Haghighirad, *et al.*, "Lead-free organic–inorganic tin halide perovskites for photovoltaic applications," *Energy Environ. Sci.*, vol. 7, pp. 3061-3068, 2014.

[92] D. Sabba, H. K. Mulmudi, R. R. Prabhakar, T. Krishnamoorthy, T. Baikie, P. P. Boix, *et al.*, "Impact of Anionic Br–Substitution on Open Circuit Voltage in Lead Free Perovskite ($CsSnI_{3-x}Br_x$) Solar Cells," *J. Phys. Chem. C*, vol. 119, pp. 1763-1767, 2015.

[93] M. H. Kumar, S. Dharani, W. L. Leong, P. P. Boix, R. R. Prabhakar, T. Baikie, *et al.*, "Lead-Free Halide Perovskite Solar Cells with High Photocurrents Realized Through Vacancy Modulation," *Adv. Mater.*, vol. 26, pp. 7122-7127, 2014.

[94] M. Weiss, J. Horn, C. Richter, and D. Schlettwein, "Preparation and characterization of methylammonium tin iodide layers as photovoltaic absorbers," *phys. status solidi A*, vol. 213, pp. 975-981, 2016.

[95] U. Bansode, R. Naphade, O. Game, S. Agarkar, and S. Ogale, "Hybrid Perovskite Films by a New Variant of Pulsed Excimer Laser Deposition: A Room-Temperature Dry Process," *J. Phys. Chem. C*, vol. 119, pp. 9177-9185, 2015/04/30 2015.

[96] M. R. Filip and F. Giustino, "Computational Screening of Homovalent Lead Substitution in Organic–Inorganic Halide Perovskites," *J. Phys. Chem. C*, vol. 120, pp. 166-173, 2016/01/14 2016.

[97] I. Girnyk, O. Krupych, I. Martunyuk-Lototska, F. Motsnyi, and R. Vlokh, "Phase Coexistence in $Cs_3Bi_2I_9$ Ferroelastics: Optical, Dilatation and Ultrasonic Velocity Studies," *arXiv preprint arXiv:0709.0053*, 2007.

[98] V. F. Machulin, F. V. Motsnyi, O. M. Smolanka, G. S. Svechnikov, and E. Y. Peresh, "Effect of temperature variation on shift and broadening of the exciton band in $Cs_3Bi_2I_9$ layered crystals," *Low Temp. Phys.*, vol. 30, pp. 964-967, 2004.

[99] F. Motsnyi, "Optical measurements of ferroelastics ($Cs_3Bi_2I_9$): New phenomena and optical devices," in *2010 International Conference on Advanced Optoelectronics and Lasers*, 2010.

[100] A. J. Lehner, D. H. Fabini, H. A. Evans, C.-A. Hébert, S. R. Smock, J. Hu, *et al.*, "Crystal and Electronic Structures of Complex Bismuth Iodides $A_3Bi_2I_9$ (A = K, Rb, Cs) Related to Perovskite: Aiding the Rational Design of Photovoltaics," *Chem. Mater.*, vol. 27, pp. 7137-7148, 2015/10/27 2015.

[101] B.-W. Park, B. Philippe, X. Zhang, H. Rensmo, G. Boschloo, and E. M. J. Johansson, "Bismuth Based Hybrid Perovskites $A_3Bi_2I_9$ (A: Methylammonium or Cesium) for Solar Cell Application," *Adv. Mater.*, vol. 27, pp. 6806-6813, 2015.

[102] M. Lyu, J.-H. Yun, M. Cai, Y. Jiao, P. V. Bernhardt, M. Zhang, *et al.*, "Organic–inorganic bismuth (III)-based material: a lead-free, air-stable and solution-processable light-absorber beyond organolead perovskites," *Nano Research*, vol. 9, 2016.

[103] R. L. Z. Hoye, R. E. Brandt, A. Osherov, V. Stevanović, S. D. Stranks, M. W. B. Wilson, *et al.*, "Methylammonium Bismuth Iodide as a Lead-Free, Stable Hybrid Organic–Inorganic Solar Absorber," *Chemistry – A European Journal*, 2016.

[104] T. Singh, A. Kulkarni, M. Ikegami, and T. Miyasaka, "Effect of Electron Transporting Layer on Bismuth-Based Lead-Free Perovskite

$(CH_3NH_3)_3Bi_2I_9$ for Photovoltaic Applications," *ACS Appl. Mater. Interfaces,* vol. 8, pp. 14542-14547, 2016/06/15 2016.

[105] B. Saparov, F. Hong, J.-P. Sun, H.-S. Duan, W. Meng, S. Cameron, *et al.*, "Thin-Film Preparation and Characterization of $Cs_3Sb_2I_9$: A Lead-Free Layered Perovskite Semiconductor," *Chem. Mater.,* vol. 27, pp. 5622-5632, 2015/08/25 2015.

[106] P. C. Harikesh, H. K. Mulmudi, B. Ghosh, T. W. Goh, Y. T. Teng, K. Thirumal, *et al.*, "Rb as an Alternative Cation for Templating Inorganic Lead-Free Perovskites for Solution Processed Photovoltaics," *Chem. Mater.,* vol. 28, pp. 7496-7504, 2016/10/25 2016.

[107] P. C. Harikesh, B. Wu, B. Ghosh, R. A. John, S. Lie, K. Thirumal, *et al.*, "Doping and Switchable Photovoltaic Effect in Lead-Free Perovskites Enabled by Metal Cation Transmutation," *Adv. Mater.,* vol. 30, p. 1802080, 2018.

[108] K. M. Boopathi, P. Karuppuswamy, A. Singh, C. Hanmandlu, L. Lin, S. A. Abbas, *et al.*, "Solution-processable antimony-based light-absorbing materials beyond lead halide perovskites," *J. Mater. Chem. A,* vol. 5, pp. 20843-20850, 2017.

[109] A. H. Slavney, T. Hu, A. M. Lindenberg, and H. I. Karunadasa, "A Bismuth-Halide Double Perovskite with Long Carrier Recombination Lifetime for Photovoltaic Applications," *J. Am. Chem. Soc.,* vol. 138, pp. 2138-2141, 2016/02/24 2016.

[110] W. Gao, C. Ran, J. Xi, B. Jiao, W. Zhang, M. Wu, *et al.*, "High-Quality Cs2AgBiBr6 Double Perovskite Film for Lead-Free Inverted Planar Heterojunction Solar Cells with 2.2 % Efficiency," *ChemPhysChem,* vol. 19, pp. 1696-1700, 2018.

[111] C. Wu, Q. Zhang, Y. Liu, W. Luo, X. Guo, Z. Huang, *et al.*, "The Dawn of Lead-Free Perovskite Solar Cell: Highly Stable Double Perovskite $Cs_2AgBiBr_6$ Film," *Adv. Sci.,* vol. 5, p. 1700759, 2018.

[112] W. Ning, F. Wang, B. Wu, J. Lu, Z. Yan, X. Liu, *et al.*, "Long Electron–Hole Diffusion Length in High-Quality Lead-Free Double Perovskite Films," *Adv. Mater.*, vol. 30, p. 1706246, 2018.

[113] G. Volonakis, A. A. Haghighirad, R. L. Milot, W. H. Sio, M. R. Filip, B. Wenger, *et al.*, "$Cs_2InAgCl_6$: A New Lead-Free Halide Double Perovskite with Direct Band Gap," *J. Phys. Chem. Lett.*, vol. 8, pp. 772-778, 2017/02/16 2017.

[114] G. Volonakis, M. R. Filip, A. A. Haghighirad, N. Sakai, B. Wenger, H. J. Snaith, *et al.*, "Lead-Free Halide Double Perovskites via Heterovalent Substitution of Noble Metals," *J. Phys. Chem. Lett.*, vol. 7, pp. 1254-1259, 2016/04/07 2016.

[115] X.-G. Zhao, J.-H. Yang, Y. Fu, D. Yang, Q. Xu, L. Yu, *et al.*, "Design of Lead-Free Inorganic Halide Perovskites for Solar Cells via Cation-Transmutation," *J. Am. Chem. Soc.*, vol. 139, pp. 2630-2638, 2017/02/22 2017.

[116] F. Giustino and H. J. Snaith, "Toward Lead-Free Perovskite Solar Cells," *ACS Energy Lett.*, vol. 1, pp. 1233-1240, 2016/12/09 2016.

[117] S. Chakraborty, W. Xie, N. Mathews, M. Sherburne, R. Ahuja, M. Asta, *et al.*, "Rational Design: A High-Throughput Computational Screening and Experimental Validation Methodology for Lead-Free and Emergent Hybrid Perovskites," *ACS Energy Lett.*, vol. 2, pp. 837-845, 2017/04/14 2017.

[118] X.-G. Zhao, D. Yang, J.-C. Ren, Y. Sun, Z. Xiao, and L. Zhang, "Rational Design of Halide Double Perovskites for Optoelectronic Applications," *Joule*, vol. 2, pp. 1662-1673, 2018/09/19/ 2018.

Chapter 3

Experimental and Theoretical Methodology

This chapter outlines the various experimental and theoretical methods used in this thesis. The first part of this chapter discusses the experimental techniques used for fabrication of thin-films, single crystals and PV devices. The specifications of each characterization techniques and conditions are also mentioned in this chapter. The second part of this chapter gives a brief introduction to VASP. The approximations and limits of VASP were also discussed in general. The methodology for defect characterizations using DFT were also outlined here. Deviation from these procedures not stated here are described in the relevant section.

3.1 Materials and Chemicals

All the relevant chemicals, unless otherwise mentioned, were purchased from Sigma-Aldrich, stored in the glovebox and were used without further purification. The glovebox was maintained under argon atmosphere with H_2O < 1 ppm and O_2 < 1 ppm. Solvents including dimethylsulfoxide (DMSO) (99.8%), dimethylformamide (DMF) (99.8%), and toluene (99%) were purchased in anhydrous form. The methylammonium iodide (CH_3NH_3I, MAI), formamidinium iodide (CH_5IN_2, FAI) and TiO_2 nanoparticles paste (30NRD) were purchased from Dyesol (now Greatcell solar), Australia. Poly(triarylamine) (PTAA), Poly(3-hexylthiophene-2,5-diyl) (P3HT), and 2,2',7,7'-Tetrakis-(N, N-di-4-methoxyphenylamino)-9,9'-spirobifluorene (Spiro-OMeTAD) were purchased from Sigma-Aldrich. Poly(4-butylphenyldiphenylamine) (PTPD) was purchased from Ossila Ltd. For solar cell device fabrication, Fluorine doped tin oxide (FTO) from Nippon Sheet Glass (TEC 7, Resistivity: 6-8 ohm/sq) was used as substrates. Quartz glass was used for spectroscopic measurement.

3.2 Synthesis of Materials

The thin-films of relevant absorber materials are fabricated via solution processing due to inherent advantages of stoichiometry control and ease of operations. In addition, all the thin-films were fabricated via single step deposition methods, *i.e.* all the required chemicals were dissolved together in a solvent for deposition.

3.2.1 Bi-based Iodide Perovskite Synthesis

For $Cs_3Bi_2I_9$ thin-films, the precursor CsI and BiI_3 were mixed in 1.5:1 atomic ratio in DMSO:DMF (4:1 v/v) mixed solvent. Depending on the requirement, the concentration of the solution was varied by controlling the amount of the precursor. For $MA_3Bi_2I_9$ and $FA_3Bi_2I_9$, a similar procedure was followed with

MAI and FAI as A-site cation source respectively. The precursor solutions were kept stirring using a magnetic bead for overnight at 70 °C to dissolve properly. The spin coating was carried out via single-step thin-film deposition method. Around 40 µL precursor solution was spread onto the substrate, following by spinning at 2000 rpm for 30 s. The substrates were annealed afterwards at 100 ℃ for 15 min on a hotplate. All the spin coating steps for Bi-based perovskites were performed inside an Ar-filled glovebox with H_2O < 1 ppm.

The single crystals of $Cs_3Bi_2I_9$ were grown by antisolvent diffusion crystallization method. Typically, 779.7 mg CsI and 1179.38 mg of BiI_3 was dissolved in 10 ml DMF and the solution was filtered through 0.2 µm polytetrafluoroethylene (PTFE) syringe filter. The precursor solution containing vial was kept inside a beaker in toluene environment undisturbed for few days to obtain mm size single crystals.

3.2.2 Ag_xBiI_{3+x} Thin-films

For synthesizing Ag_xBiI_{3+x} thin-films, the stoichiometric amount of AgI and BiI_3 were mixed together in DMSO:DMF (7:3 v/v) and kept for overnight stirring at 70 °C. For $AgBiI_4$, the ratio of AgI-to-BiI_3 was kept 0.9:1 and for Ag_2BiI_5, the ratio was 2:1. In normal spin coating (NSC) method, spin speed was maintained at 5000 rpm for 45 s with a ramp of 2 s. For dynamic hot casting (DHC) method (Figure 3.1), around 60 µL precursor solutions (100 ℃) was dropcasted onto the preheated substrate (100 ℃) during spinning stage. The coated substrates were then annealed at 160 ℃ for 30 minutes in both NSC and DHC technique. The fabrication of $AgBiI_4$ and Ag_2BiI_5 thin-films were carried out in ambient atmosphere.

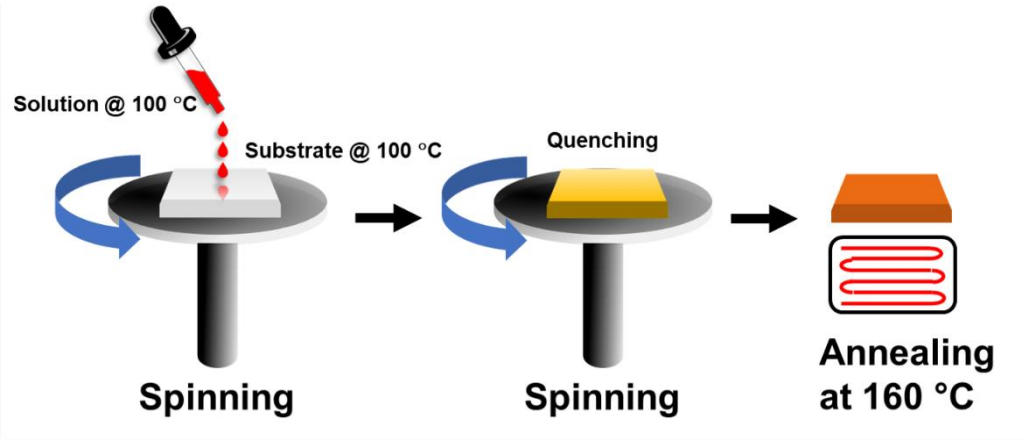

Figure 3.1: Schematic illustration of dynamic hot casting (DHC) method.

3.3 Solar Cell Fabrications

Fluorine-doped tin oxide (FTO) coated glass slides were first patterned by laser-etching, following by cleaning in soap solution, DI water and ethanol. After ozone plasma treatment of the glass slides, spray pyrolysis technique was used to deposit a thin TiO_2 blocking layer using titanium diisopropoxide bis(acetylacetone) as the precursor solution. Subsequently, ~500 µm thick TiO_2 mesoporous layer was deposited by spin coating of TiO_2 nanoparticles (particle size ~30 nm). The spin-coated TiO_2 layer was then annealed at 450 ℃ for 30 minutes, followed by ambient cooling. The mesoporous substrates were then treated with $TiCl_4$ solution (5 mM) for 30 minutes at 70 ℃. The substrates were then dried using air gun and followed by another annealing step at 500 ℃. The absorber layer was deposited onto mp-TiO_2 layer via either NSC or DHC method. After the deposition of absorber layer, suitable hole-transport layer (HTM) such as Spiro-OMeTAD (100 mg mL^{-1} in chlorobenzene) was spin-coated at 4000 rpm for 30 s. Around 80 nm Au contact electrode was deposited by thermal evaporation. The device area was defined by a metal mask with an aperture area of 0.2 cm^2.

3.4 Characterization Techniques

3.4.1 Thin-films Characterizations

A. X-ray Diffraction (XRD)

X-ray diffraction was carried out at room temperature to investigate the crystal structure and phases of the thin-films and powder samples using Bruker D8 Advanced Diffractometer (Bragg-Brentano geometry) with Cu-K_α radiation (λ = 1.5418 Å) and refined with Rietveld refinement. For grazing angle XRD, an incident angle of 4° was used to record the pattern with a step size of 0.05° and a time step of 1 s. The XRD patterns were analyzed using X'pert Highscore software.

B. Scanning Electron Microscopy

Field Emission Scanning Electron Microscope (JEOL, JSM-7600F, operated at 5 kV) was used to characterize the surface and cross-sectional morphology of the thin-films. To improve the resolution and reduce the charge collection on the surface, the samples were platinum-coated (10 nm) before analysis. For energy dispersive X-ray spectroscopy (EDX), the accelerating voltage was increased to 15 kV during operations.

C. Absorption (UV-Vis) Spectroscopy

UV-Visible spectrophotometer (Shimadzu-3600) was used to characterize the absorption spectra of the thin-films in the wave-length range of 300-800 nm at room temperature with integrated sphere attachment (ISR-3100) and 20 nm slit-width. The film thickness was determined by surface profilometer. The absorption coefficient was calculated by the following equation:

$$\alpha\ (cm^{-1}) = \frac{absorbance\ (A)(a.u)}{thickness\ (t)(cm)} \quad (1)$$

D. Photoluminescence (PL) Spectroscopy

Time-integrated photoluminescence measurement were conducted by directing the excitation laser pulses to single crystals/thin films. The photoluminescence was collected at a backscattering angle by a spectrometer (Acton, Spectra Pro 2500i) and CCD (Princeton Instruments, Pixis 400B). Time-resolved photoluminescence was collected using an Optronis Optoscope streak camera system which has an ultimate temporal resolution of 10 ps.

E. Transient Absorption (TA) Spectroscopy

Transient absorption measurements were performed using an integrated Helios and EOS setup (Ultrafast Systems LLC). The transient dynamics in fs–ns time region (150 fs–5 ns) was acquired by Helios that works in a nondegenerate pump–probe configuration. The 400 nm pump pulses were generated from a beta barium borate (BBO) crystal that was used to double the frequency of 800 nm from a 1-kHz regenerative amplifier (Coherent Legend, 800 nm, 150 fs, 1 mJ). A mode-lock Ti-sapphire oscillator (Coherent Vitesse, 80MHz) was used to seed the amplifier. The probe pulses were a white light continuum generated by passing the 800 nm fs pulses through either a 2 mm sapphire plate for visible part (400–800 nm) or a 1 cm sapphire plate for NIR part (800–1600 nm). The transient dynamics in the ns–μs time region (1 ns–1 μs) was acquired by EOS. The pump beam was the same with that used in Helios. The probe beam EOS was a white continuum generated from a photonic fiber using a Nd:YAG laser (1064 nm). The probe light was collected using a CMOS sensor for UV–VIS part and InGaAs diode array sensor for NIR part.

F. Cathodoluminescence (CL) Spectroscopy

The cathodoluminescence measurements were performed on FEI Verios scanning electron microscope (SEM) equipped with a Gatan MonoCL$_4$ Elite cathodoluminescence (CL) system. Samples were spin coated onto silicon substrate as described earlier. Power resolved CL spectroscopy was performed by exposing a fixed area of sample (30 μm^2) with a constant accelerating voltage at 5kV and varying the beam current from 0.1-3.2 nA.

G. Ultraviolet Photoelectron Spectroscopy (UPS)

The UPS measurements were carried out using a VG ESCA Lab system. An integrated ultrahigh vacuum (UHV) system equipped with the fast-entry lock chamber and analysis chamber with typical base pressure in the range of ~10^{-10} mbar. To provide ultraviolet irradiation impinged to the sample, the analysis chamber is equipped with a He discharge lamp. The UV source was an unfiltered He I (21.2 eV) excitation and the sample was biased at -5 V to extract the low-energy secondary cutoff. The UV light spot size on the sample is about 1 mm in diameter.

3.4.2 Solar Cell Device Characterization

The IV curves of the devices were produced using solar simulator (San-EI Electric, XEC 301S) at AM1.5 illumination (power density 1000 W m^{-2}) and recorded by Keithley model 2612A source meter. EQE/IPCE measurement was carried out by PV300 (Bentham) equipped with Xenon/quartz halogen monochromatic light source. The device area was 0.2 cm^2 as defined by a metal shadow mask during *J-V* characterizations.

3.5 Theoretical Framework

3.5.1 Introduction to VASP

Density functional theory (DFT) calculations in this study were carried out using Vienna ab initio Simulation Package (VASP) [1-7]. VASP is a proprietary package written on Fortran 90 program for atomic scale materials modelling. The underlying principle of VASP is the approximate solution to the many-body Schrodinger equation which is solved either within DFT or using Kohn-Sham (KS) equation or using Hartree-Fock (HF) approximations. The interaction between electrons and ions are described by either norm-conserving or ultrasoft (US) or projector-augmented-wave (PAW) in VASP calculations. VASP also offers parallelization over bands and over plane wave coefficient.

3.5.2 Calculation Parameters

The electronic structure calculations are performed through VASP with the standard frozen-core projected augmented-wave method (PAW) with 400 eV as the cut-off energy for basis set. The atomic positions are relaxed till force/atom is less than 0.05 eV/Å. All structural relaxations were performed with Gaussian smearing of 0.05 eV. Cs, Bi, and I atoms are described by $5s^2 5p^6 6s^1$, $5d^{10} 6s^2 6p^3$, $5s^2 5p^5$ valence electrons respectively. A 5×5×2 Monkhorst-Pack for single unit cell and 5×5×2 Gamma K-point grid for supercell calculations are applied for Brillouin zone integration. All schematic representations of the crystal structures were generated using VESTA program [8].

3.5.3 Band Structure Calculations

The simulations of the band structures were carried out in two steps. Initially, the unit cell was relaxed by a self-consistent run. Finally, a non-self-consistent run was performed using earlier charge density and the energy states were calculated along high symmetry direction on discrete K mesh. The high

symmetry path was shown in the Figure 5.2 i.e. from Brillouin zone center Γ with the coordinates (0, 0, 0) to M (0.5, 0, 0), K (0.333, 0.333, 0), Γ (0, 0, 0), A (0, 0, 0.5), L (0.5, 0, 0.5), and H (0.333, 0.333, 0.5).

3.5.4 Effective Mass Calculations

Effective mass of the carriers was calculated assuming parabolic band diagram at CBM and VBM based on the following equation

$$m^* = \hbar^2 \left[\frac{\partial^2 \varepsilon(k)}{\partial k^2}\right]^{-1} \quad (2)$$

Where $\epsilon(k)$ represents band eigenvalues and k is the crystal momentum vector.

3.5.5 Methodology for Defects Calculations

The chemical nature of any solid is often characterized by the defects that are present in the crystalline solids. However, it is quite difficult to experimentally determine defects in a solid. Another approach may be DFT which can calculate the defects energies. The contribution of the defects on a crystalline material can be quantified by the transition levels and the concentration, both of which can be deduced from DFT. Depending on the transition level, the defect may act like donor, acceptor, or both as well as whether it is shallow or deep. On the other hand, its influences are determined by the concentration of that defect. Both aspects can be quantified from the formation energy of the defects. In the dilute limit, defect formation energy E_{form} governs the defect concentration N at a constant volume through Boltzmann expression:

$$N = N_0 \exp\left(\frac{-E_{form}}{k_B T}\right) \quad (3)$$

Where, N_0 is the number of applicable sites (including the symmetry-equivalent local configurations) and k_B is the Boltzmann constant.

In a perfect crystal, the defects are generated upon exchanging particles between the atoms and/or electron reservoir and the crystal. The energy of the atom reservoir energy is determined by the chemical potential of the elements and electrons reservoir is determined by the Fermi energy. The total energies of the crystal can be obtained from first principles, i.e., without resorting to the experimental parameters. In principle, the defect formation energy can be calculated from [9]

$$E^f[X^q] = E_{tot}[X^q] + \sum_i n_i \mu_i - E_{tot}[bulk] + qE_F + E_{corr} \quad (4)$$

The total energy $E_{tot}[X^q]$ is calculated for the supercell containing the defect X in charge state q, and $E_{tot}[bulk]$ for the perfect supercell. The integer n_i is the number of atoms of species i (host atoms or impurity atoms). n_i is positive when the it is removed from the supercell and negative when it is added to the supercell to create the defect, and the μ_i is the relative chemical potentials of i. The last term, E_{corr} is the correction term that include other effects such as image charge correction [10], band filling correction and finite-size effects. However, this term is not included here as the objective of this study is not to calculate absolute energy, rather compare formation energies for different point defects.

References

[1] G. Kresse and D. Joubert, "From ultrasoft pseudopotentials to the projector augmented-wave method," *Phys. Rev. B,* vol. 59, p. 1758, 1999.

[2] G. Kresse and J. Furthmüller, "Efficient iterative schemes for *ab initio* total-energy calculations using a plane-wave basis set," *Phys. Rev. B,* vol. 54, pp. 11169-11186, 10/15/ 1996.

[3] G. Kresse and J. Hafner, "*Ab initio* molecular-dynamics simulation of the liquid-metal amorphous-semiconductor transition in germanium," *Phys. Rev. B,* vol. 49, pp. 14251-14269, 05/15/ 1994.

[4] G. Kresse and J. Hafner, "*Ab initio* molecular dynamics for liquid metals," *Phys. Rev. B,* vol. 47, pp. 558-561, 01/01/ 1993.

[5] J. P. Perdew, K. Burke, and M. Ernzerhof, "Generalized Gradient Approximation Made Simple," *Phys. Rev. Lett.,* vol. 77, pp. 3865-3868, 10/28/ 1996.

[6] J. P. Perdew, K. Burke, and Y. Wang, "Generalized gradient approximation for the exchange-correlation hole of a many-electron system," *Phys. Rev. B,* vol. 54, p. 16533, 1996.

[7] J. P. Perdew and Y. Wang, "Accurate and simple analytic representation of the electron-gas correlation energy," *Phys. Rev. B,* vol. 45, pp. 13244-13249, 06/15/ 1992.

[8] K. Momma and F. Izumi, "VESTA 3 for three-dimensional visualization of crystal, volumetric and morphology data," *J. Appl. Crystallogr.,* vol. 44, pp. 1272-1276, 2011.

[9] S. Lany and A. Zunger, "Assessment of correction methods for the band-gap problem and for finite-size effects in supercell defect calculations: Case studies for ZnO and GaAs," *Phys. Rev. B,* vol. 78, p. 235104, 12/04/ 2008.

[10] G. Makov and M. C. Payne, "Periodic boundary conditions in *ab initio* calculations," *Phys. Rev. B,* vol. 51, pp. 4014-4022, 02/15/ 1995.

Chapter 4*

Charge Carrier Dynamics and Photovoltaic Performance of Bismuth-based Iodide Perovskite

This chapter describes the structural and optoelectronic properties of bismuth-based iodide perovskites. X-ray diffraction and optical absorption studies indicate that Bi-based perovskites crystallize into $A_3Bi_2I_9$ (A = Cs, CH_3NH_3, CH_5N_2) molecular structure in which $[Bi_2I_9]^{3-}$ bioctahedra are separated by large A-site cations. As a prototype, $Cs_3Bi_2I_9$ was investigated for mesoscopic solar cell absorber. Despite a reasonable optical bandgap (~2 eV) and absorption coefficient, the power conversion efficiency of $Cs_3Bi_2I_9$-based mesoscopic solar cells was found to be severely limited by poor photocurrent density. Comparison between thin-films and single crystals highlights the presence of intrinsic defects in thin-films, which act as nonradiative recombination centers. Further studies by transient absorption spectroscopy revealed that other reasons behind the poor performance of $Cs_3Bi_2I_9$-based solar cells might be charge localizations due to the molecular crystal structure.

*This section published substantially as Biplab Ghosh, Bo Wu, Hemant Kumar Mulmudi, Claude Guet, Klaus Weber, Tze Chien Sum, Subodh G. Mhaisalkar, and Nripan Mathews. Limitations of $Cs_3Bi_2I_9$ as lead-free photovoltaic absorber materials. *ACS Applied Materials and Interfaces* 10(41), 35000-35007 (2018). DOI: 10.1021/acsami.7b14735.

4.1 Introduction

Lead (Pb) halide perovskites have attracted enormous interest as of late because of their exciting optical properties, which have resulted in over 23% efficient photovoltaics. Nevertheless, stability and toxicity remain enormous hurdles for extensive applications of these compounds in photovoltaics. Thus, alternative compounds with similar optoelectronic properties need to be considered. Group 15 elements from the periodic table, especially Bi appears to be a suitable replacement of Pb for optoelectronic applications. Bi possesses similar electronic configurations as that of lead, expecting similar chemical properties. Besides, bismuth halides are highly stable in ambient atmosphere and soluble in organic solvents, leading to easy fabrication of perovskites via solution processable route.

Bi-based halide perovskites are an interesting class of material because of their rich structural diversity and semiconducting properties [1]. The ability of bismuth to exist in a wide range of coordination geometries (from cluster to 1D, 2D, or even 3D) makes it particularly exciting for designing novel compounds for optoelectronic applications. Studies on the coordination chemistry of bismuth halides over several decades conclude that the network of metal-anionic motifs can be easily manipulated by varying the size and geometry of cations, reaction environments, and crystallization conditions [2-4]. Based on recent success with Pb-based halide perovskites, similar attempts have been made to synthesize Bi-based perovskites which crystallize into $[Bi_2I_9]^{3-}$ family of compounds [5]. Extensive work has also been done previously on this family of compounds, but mostly on structural characterizations [6, 7]. Herein, we examined the templating effect of three cations, namely Cs, MA, and FA which are widely used with Pb-based halide perovskites. Later, $Cs_3Bi_2I_9$ was used as a prototype Bi-based iodide perovskite for optoelectronic and photovoltaic characterizations.

4.2 Physical Characterizations

Bi-based iodide perovskites were synthesized by solution processing route. The iodide salts of each *A*-site cations were dissolved in organic solvents along with bismuth iodide (BiI_3) to prepare the precursor solution, which was later spin-coated and annealed to fabricate the thin-films. Figure 4.1 shows the grazing-angle X-ray diffraction patterns of $Cs_3Bi_2I_9$ (CBI), $MA_3Bi_2I_9$ (MBI) and $FA_3Bi_2I_9$ (FBI) thin-films. The reference reflection patterns for CBI and MBI were indexed with calculated patterns from single crystal data [8, 9]. As illustrated in Figure 4.1, both CBI and MBI films exhibit reflection peaks corresponding to the pure CBI and MBI phase without any presence of impurity. The lattice constants and the crystal structure of the phases are well matched with the reported crystal structure as shown in Table 4.1. For FBI, there were no available single crystal data previously reported in the literature. Hence, we performed Rietveld refinement of the FBI powder. The FBI powder was collected by drop-casting the precursor solution onto a glass substrate, followed by annealing and scratching off the powder for the XRD analysis. The crystal structure of FBI is found to be best fitted with hexagonal crystal structure (Table 4.1). The XRD reflection peaks of the FBI thin-film was indexed with the calculated pattern as shown in Figure 4.1. The pattern is in close resemblance to the case of MBI XRD pattern with gradual shift of the peaks to smaller 2θ values. The shift can be rationalized with the larger size of formamidinium cation (ionic radius 2.79 Å) as compared to methylammonium ion (ionic radius 2.7 Å) which results in increased lattice constant of the former. Moreover, this trend can also be realized comparing with the CBI XRD pattern. From Cs (ionic radius 1.88 Å) to MA to FA, the size of *A*-site cation increases which results in an increased lattice constant and shifts of reflection peaks towards smaller angle.

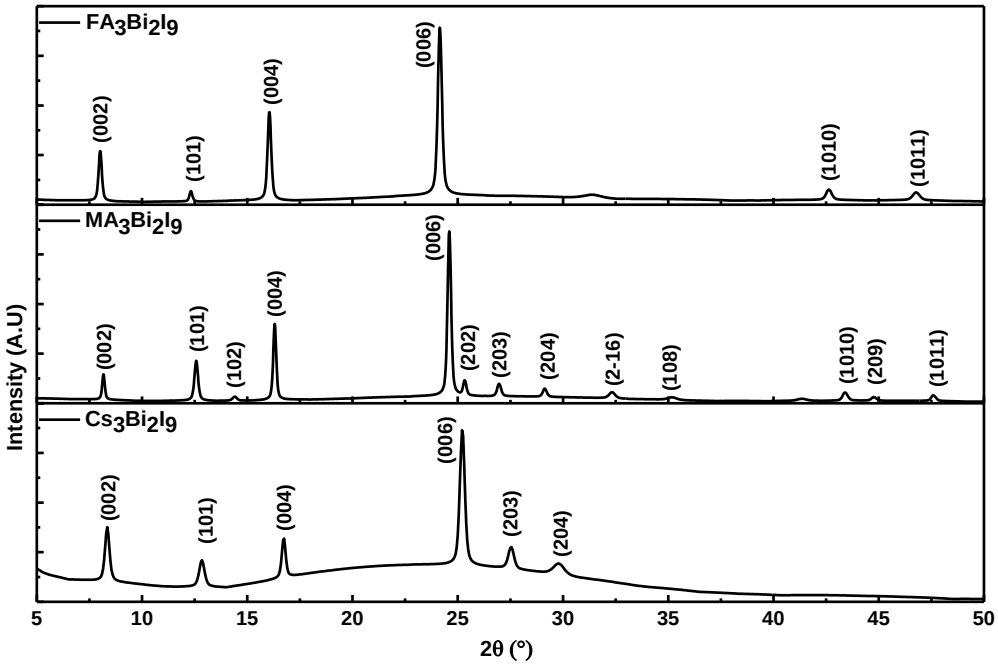

Figure 4.1: Grazing-angle XRD patterns of bismuth-based iodide perovskites (the reflection peaks are indexed with simulated XRD patterns from single crystal data).

This demonstrates that all these compounds form $A_3Bi_2I_9$ [A = Cs^+, $CH_3NH_3^+$, $CH_3(NH_2)_2^+$] crystal structure (space group: p6$_3$mmc) which is composed of $[Bi_2I_9]^{3-}$ bioctahedra, alternating between *A*-site cations, whereas, Pb-based halide perovskites composed of corner-sharing $[PbI_6]^{4-}$ octahedra and the *A*-site cation occupies the octahedral voids as shown in Figure 2.1. The crystal structure of Bi-based perovskites can be visualized as a defect-variant perovskite with a general formula of $A_3Bi_2\square I_9$ where □ denotes a Bi vacancy. Figure 4.2 schematically illustrates the evolution of defect-assisted structure from an ideal perovskite crystal structure.

Table 4.1: Lattice parameters of $A_3Bi_2I_9$ (A = Cs, MA, FA) perovskites

	$Cs_3Bi_2I_9$		$MA_3Bi_2I_9$		$FA_3Bi_2I_9$	
	Current study	References	Current study	References	Current study	References
a (Å)	8.42	8.41[5], 8.65[10], 8.58[11]	8.58	8.47[12], 8.58[9, 10, 13] 8.57[11]	8.77	9.36[10], 8.69[11]
b (Å)	8.42	8.42[5], 8.65[10], 14.52[11]	8.58	8.47[12], 8.58[10, 13] 14.85[11]	8.77	9.34[10], 15.11[11]
c (Å)	21.2	21.2[5], 21.92[10], 21.15[11]	21.74	21.614[12] 21.69[9, 10] 21.72[11] 21.76[8]	22.11	21.96[10], 22.05[11]
Volume (Å^3)	1301.0	1300.5[5], 2539.59[11]	1386.1	1388.46[13], 1341.9[12], 2737.76[11] 1384.2[9]	1471.56	2866.73[11]

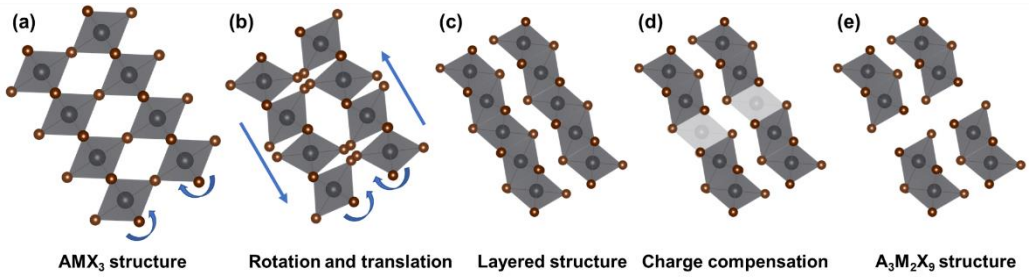

Figure 4.2: Evolution of defect-assisted $A_3M_2X_9$ molecular structure from ideal perovskite sturcture AMX_3 (A-site cations omitted for clarity). (a) ideal cubic perovskites as viewed from [110] direction, (b) due to large A-site cation, there is a rotation of the octahedra and translation, forming skutterudite structure, (c) further translation in [110] direction results in the layered perovskite structure, (d) one layer of the octahedra is removed for charge compensation due to +3 oxidation state of *M*-site cation, forming (e) $A_3M_2X_9$ crystal structure.

Although the positions of the reflections in XRD pattern perfectly match the reference patterns, the spin-coated thin-films show higher intensities in (00*l*) planes, which can be attributed to the preferential orientation of the grains along *c*-direction. Besides, the high angle reflections are also completely missing which may be due to thickness of the films. The preferential orientations of grains in CBI and MBI can also be observed in the scanning electron micrograph as shown in Figure 4.3. Both CBI and MBI shows platelet grains with a needle-like protrusion. On the other hand, the surface coverage of FBI-based thin-films was found to be severely inadequate.

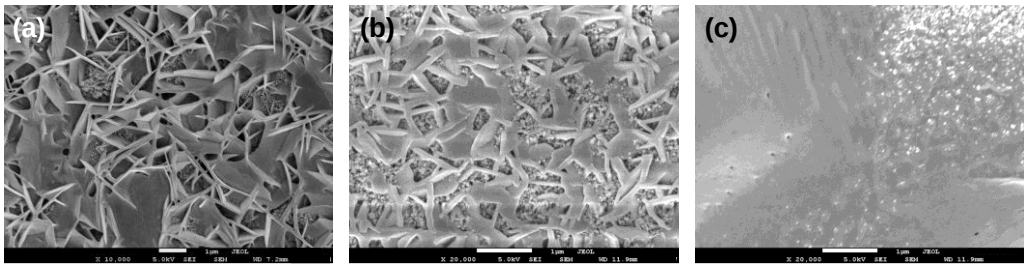

Figure 4.3: Scanning electron micrograph of (a) $Cs_3Bi_2I_9$, (b) $MA_3Bi_2I_9$, and (c) $FA_3Bi_2I_9$ thin-films deposited on mesoporous TiO_2 substrate.

In order to assess the potentials in photovoltaics, steady-state absorption spectroscopy was carried out to estimate the optical bandgap. Figure 4.4(a) illustrates the absorption spectra of these thin-films deposited on glass substrates. The bandgap of each compound was estimated using the Tauc plot for an indirect allowed optical transition, whose quantity was plotted against hν based on the following relationship:

$$(\alpha h\nu)^2 \propto \left(h\nu - E_g\right) \quad (1)$$

where α is absorption coefficient, h is the Plank's constant, and ν is the frequency of light. All the phases showed similar bandgaps with values of 2.1 eV, 2.08 eV, and 2.18 eV for CBI, MBI, and FBI respectively (Figure 4.4(b-d)). On the contrary, lead-based halide perovskites show larger range of absorption onset revealing a greater dependency on the size of the *A*-site cations [14]. While the optical bandgaps of these Bi-based perovskites are far off from an optimum single junction solar cell's bandgap, a two eV bandgap semiconductor can be efficiently used for tandem/semi-transparent solar cell applications where high open-circuit voltage (V_{OC}) is of prime concern [15]. Another interesting feature of the absorption spectra is the presence of sharp excitonic-like characteristics at the absorption onset. This sharp excitonic absorption is a characteristic feature for low dimensional perovskite materials at room

temperature, whereas it is inseparable from the continuous absorption edge for higher dimensional perovskite materials [16]. For Bi-based iodide perovskites, the excitonic absorption peak near the bandedge is usually correlated with strong quantum confinement effect due to 0D nature of $[Bi_2I_9]^{3-}$ bioctahedra (discussed later). The measured absorption coefficient of ~$1x10^4$ cm^{-1} at 450 nm for $Cs_3Bi_2I_9$ thin films is also reasonable for such high and indirect bandgap materials, but at least one order smaller than $MAPbI_3$ thin films [17].

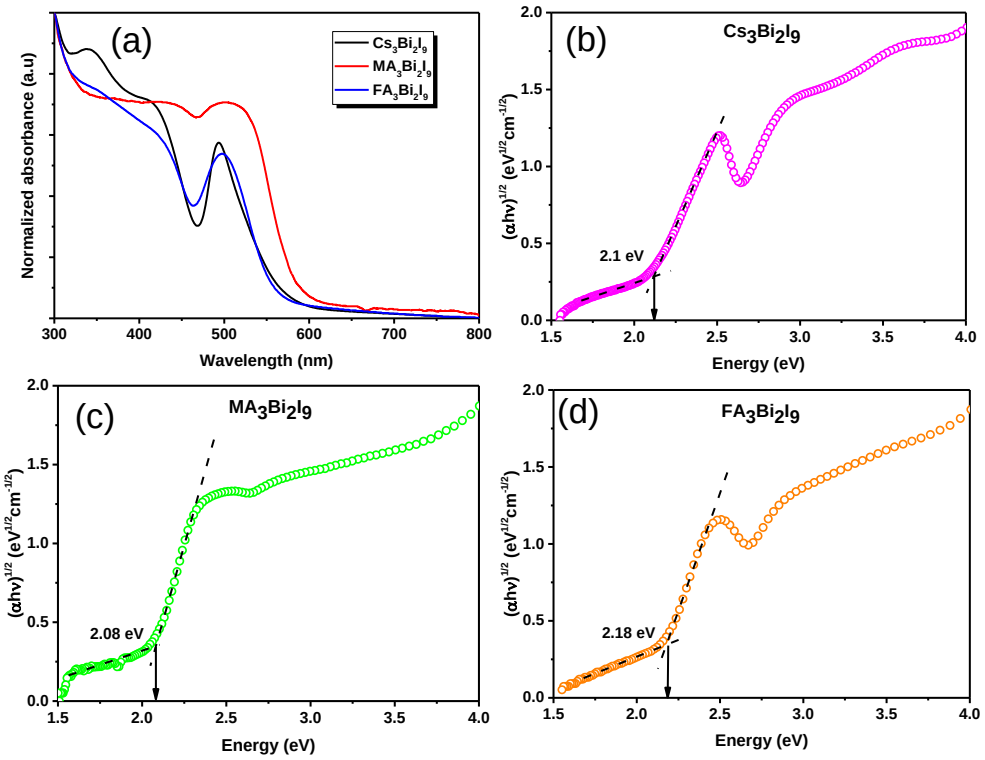

Figure 4.4: Optical properties of $A_3Bi_2I_9$ thin-films deposited on glass substrate. (a) Normalized absorption spectra of $Cs_3Bi_2I_9$, $MA_3Bi_2I_9$, and $FA_3Bi_2I_9$ thin-films as plotted against wavelength. The Tauc plots near bandedge for the absorption spectra of (b) $Cs_3Bi_2I_9$, (c) $MA_3Bi_2I_9$, (d) $FA_3Bi_2I_9$.

4.2.1 Stability of Bi-based Perovskites

In order to assess the atmospheric stability of Bi-based iodide perovskites, the thin-films were stored in ambient condition with relative huidity (RH) of 60-75% in ambient light at 22 ℃. Figure 4.5 shows the grazing angle XRD patterns of the thin-films. All three phases exhibit similar degradation mechanism via partial oxidation to BiOI. Considering relative intensities of the peaks, $MA_3Bi_2I_9$ appears to be less stable among these three phases.

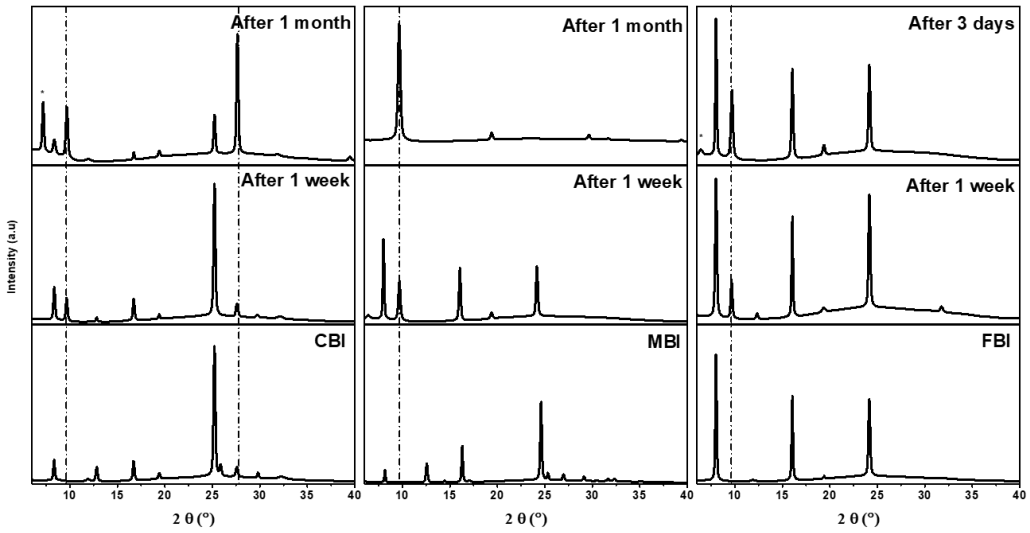

Figure 4.5: Grazing angle XRD patterns of bismuth-based iodide perovskites. Thin-films were kept in ambient atmosphere (22 ℃, 60-75% RH, fluoroscent light). Vertical dashed lines indicate BiOI reflections. No suitable phase was found for the reflection below 5° 2θ (marked *). Bottom panel for each composition shows the pattern on first day.

Figure 4.6 shows the optical photograph of the thin-films deposited on glass substrates. Apparently, there is no color change in $Cs_3Bi_2I_9$ and $FA_3Bi_2I_9$ thin-films after 1 week of storage. However, the thin-films became darker after 1 month of storage, which is most probably due to an increased volume fraction of BiOI as indicated in the XRD patterns. Interestingly, CBI and FBI films show additional reflection at very low angle (<5°) which did not correspond to any suitable phase in the current database. We believe the reflection is due to formation of hydrated phase of Bi-based perovskites. Similar low angle reflections were also observed with $MAPbI_3$ over long exposure time in water vapor [18]. Thus, the preliminary investigations on the optical properties of several *A*-site cations reveal that optical bandgaps of Bi-based perovskites remain insensitive to *A*-site cation (considering similar crystal structure). However, all inorganic $Cs_3Bi_2I_9$ exhibited superior stability in ambient atmosphere as compared to organic-inorganic hybrid perovskites (MA and FA-containing perovskites). Similar observations can also be found for Pb-based halide perovskites. Hence, for further characterizations and photovoltaic applications, $Cs_3Bi_2I_9$ was selected as a prototype Bi-based iodide perovskite.

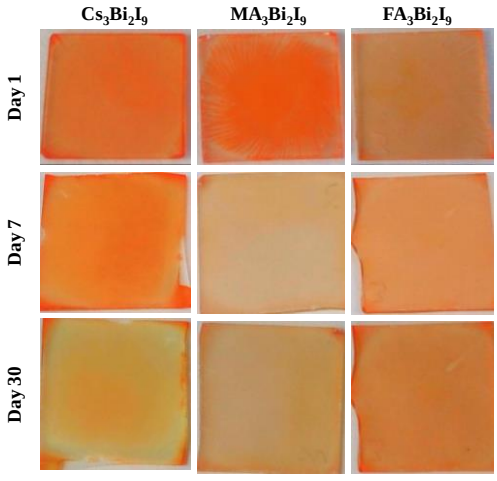

Figure 4.6: Optical photograph of Bi-based iodide perovskite thin-films; glass is used as substrates. The samples were kept in ambient atmosphere (22 ℃, 60-75% RH, fluoroscent light).

4.3 Photo-physical Characterization of $Cs_3Bi_2I_9$

4.3.1 Photoluminescence Spectroscopy

Photoluminescence spectroscopy is one of the most common techniques used to measure the fraction of radiative recombination which should be maximized for good PV applications. Unfortunately, $Cs_3Bi_2I_9$ thin-films do not display prominent photoluminescence spectra as seen with Pb-based halide perovskites; instead a broad and asymmetric luminescence peak (PLQY < ~10^{-5}) was observed. As the low-temperature solution processing technique often suffers from high defect density, we grew $Cs_3Bi_2I_9$ single crystals to overcome the uncertainties of thin-film processing conditions. Figure 4.7(a) shows the static PL spectra of $Cs_3Bi_2I_9$ thin-films and single crystals. Unsurprisingly, PL intensity from single crystals was much higher (more than 100 times) compared to thin-films, most probably due to reduced defect states. The single crystal exhibits a neat PL emission centered around 1.9 eV, which is ~0.2 eV blue-shifted from the optical bandgap. Despite the marked improvement of PL intensity in single crystals, the emission was still low compared to highly luminous Pb-based halide perovskites. There may be various reasons of low PL emission from $Cs_3Bi_2I_9$, most notably indirect bandedge and high defect concentration. Due to the indirect band edge of $Cs_3Bi_2I_9$, the radiative recombination only occurs when phonons are involved in conserving momentum, which results in a very low quantum yield and a broad spectrum. To confirm, we carried out transient photoluminescence (TRPL) spectroscopy of the thin films and the single crystals to determine the carrier lifetime. If the origin of the luminescence is from the indirect band edge, then the carriers that are located at the indirect band edge should exhibit long lifetime (discussed later). As illustrated in Figure 4.7(b), thin films show a bi-exponential decay with a time constant of 5 ps (98%) and 73 ps (2%), while single crystals have a lifetime of ~160 ps. These values are much shorter as compared to the lifetime

of free carriers which is the dominant mechanism in $MAPbI_3$ [17]. Hence, phonon-assisted multiple self-trapped exciton emission models seems more plausible for the broad emission from $Cs_3Bi_2I_9$ as reported recently by McCall, *et al.* [19] from their low-temperature photoluminescence studies.

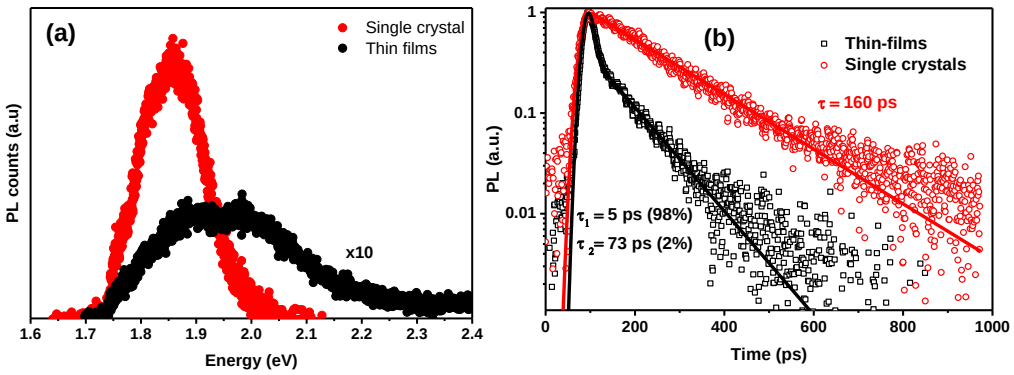

Figure 4.7: Luminescence spectroscopic study of $Cs_3Bi_2I_9$. (a) Comparison of photoluminescence spectra from thin-films and single crystal $Cs_3Bi_2I_9$. (b) Photoluminescence decay time of $Cs_3Bi_2I_9$ thin-films and single crystals.

4.3.2 Cathodoluminescence Spectroscopy

To further resolve the nature of the emission, we explored cathodoluminescence (CL) spectroscopy in which high energy electron beam can provide better spatial resolution than conventional PL spectroscopy due to the order-of-magnitude higher carrier generations [20]. The typical CL spectra of $Cs_3Bi_2I_9$ thin films show two emission bands, a weak band centered at 1.91 eV and a much stronger band centered at 2.5 eV (represented as peak 1 and peak 2 respectively) (Figure 4.8(a)). The latter can be assigned to the direct exciton emission as the position corresponds well with the direct exciton absorption peak, which was absent in our room temperature photoluminescence studies

[19, 21]. As a step further, we extended our CL studies at varied excitation power (represented by the electron-beam current I_b) and analyzed using simple power law model[22], $I_{CL} \propto I_b^k$. The power-law fittings as illustrated in Figure 4.8(b) reveal that the intensities of peak 2 and peak 1 display a linear and a sublinear relationship with the excitation power respectively. The linear relationship for the peak 2 confirms the free excitonic luminescence of $Cs_3Bi_2I_9$, which was too weak to be detected in typical photoluminescence studies. The sublinear dependence of the peak 1 on power is also consistent with our PL studies and with the localized nature of the self-trapped excitons (STE) by extrinsic defects [22-24]. Unfortunately, recombination by STE is predominant over free excitonic luminescence, which usually have negative impact on PV performances.

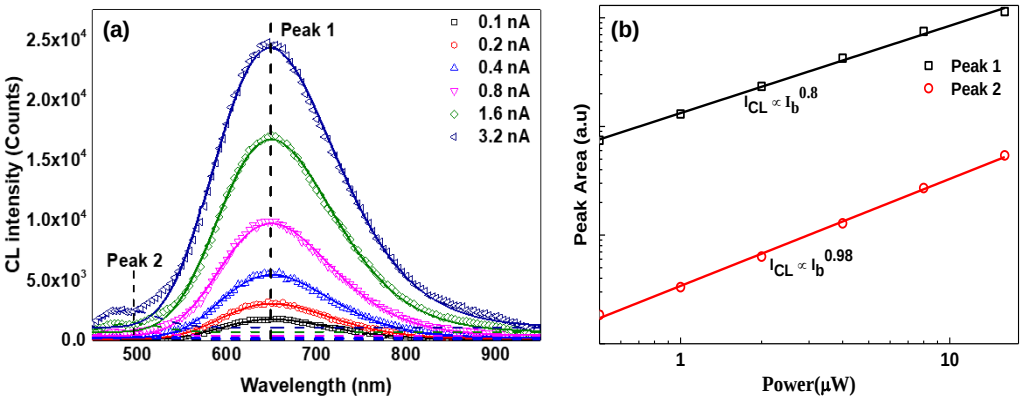

Figure 4.8: Cathodoluminescence (CL) spectroscopic study of $Cs_3Bi_2I_9$. (a) CL spectra of $Cs_3Bi_2I_9$ thin-film under different current bias. (b) Power-law fits of CL peak area (see text for details) against different electron beam power.

4.3.3 Transient Absorption Spectroscopy

As the low PLQY limits the utility of photoluminescence spectroscopy, we carried out transient absorption (TA) spectroscopic analysis on thin films to elucidate the dynamics of the photoexcited carriers. As illustrated in Figure 4.9(a), several features can be identified from the TA spectra (under 400 nm excitation at different time delays): (2) a negative transient absorption peak at around 2.52 eV (492 nm) ($\Delta A<0$, $\Delta T/T>0$); (1) and (3) two positive transient absorption peaks at 2.62 eV (473 nm) and 2.23 eV (554 nm), and (4) a broad, feature-less photo-induced absorption (PIA) extending from visible to near-infrared region. The negative peak corresponds well with the exciton peak showing in steady state absorption spectrum (Figure 4.4(a)); hence, we attribute it to the photo-bleach (PB) of the exciton peak. The broad PIA extending from Visible to NIR region shows an immediate sub-picosecond rise after photo-excitation (within our system response), followed by a very fast decay (τ_1= 4 ps, τ_2= 68 ps). The spectrum feature, together with the immediate rise and fast decay, points that the broad PIA can be attributed to the absorption from the "hot carrier" located at the Γ valley (direct transition region) before relaxation to the indirect band-edge (M point) (see chapter 5 for details). Such fast decay within tens of picoseconds corresponds well with intervalley relaxation mediated by carrier-phonon scattering [25].

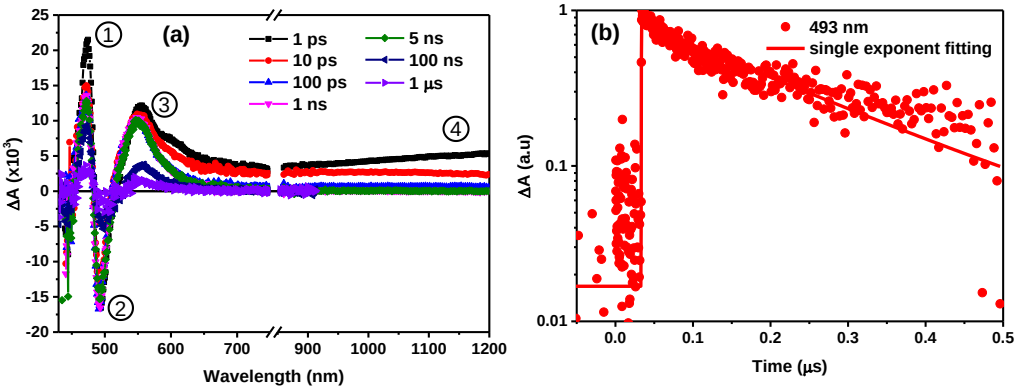

Figure 4.9: Exited-state charge carrier dynamics in $Cs_3Bi_2I_9$. (a) Transient absorption spectra of $Cs_3Bi_2I_9$ thin-films for different time delays under 400 nm excitation, (b) Excited-state carrier decay dynamics of the same at 493 nm.

Transient absorption at exciton resonances can be induced by several mechanisms, such as phase-space filling, Coulombic screening, bandgap renormalization, etc. [26]. To elucidate the detailed mechanism, we analyzed the decay dynamics of the excited-state carriers. The exciton bleaching peak (2) decay contains multiple information: an initial fast decay corresponds to the hot carrier relaxation, followed by a slow rise and then an almost constant value within the 5 ns time window. Similar dynamics are also observed for the PIA at the blue side (1); the red side PIA (3) is slightly different, possibly due to the overlapping of the signals with the hot-carrier induced absorption. In addition, the long-residual as revealed by the ns-µs transient absorption in Figure 4.9(b), shows a decay time constant of around 200 ns. This long-lived component cannot be attributed to exciton recombination lifetime, as otherwise the luminescence should be strong and show similar decay constant. The long-lived species is expected to originate from the relaxed carriers at the indirect band edge. Recombination via band-to-band transition is forbidden for the carriers located at the indirect band edge; therefore, they have a typical lifetime much longer than direct bandgap materials. The dynamics of the exciton peak

indicates that the dynamics do not originate from exciton itself, but instead, is a result of the carriers-induced transmission change near the exciton resonance. While phase-space filling usually only change the oscillation strength of the excitons, Coulombic screening and bandgap renormalization effects can result in exciton linewidth broadening and position shifts [27]. The bleaching near exciton resonance, together with two PIA band lying on both sides of the bleaching peak, is a typical signature of exciton band broadening due to carrier-exciton scattering after photo-excitation [25]. In the initial time (~10 ps), the broadening is mainly attributed to the non-relaxed hot carriers; after that, the carriers that gradually relaxed to the indirect band edge contribute to the scattering effects. Note that Scholz, et al. [28] recently attributed a similar signal in $MA_3Bi_2I_9$ to the exciton Stark effect. Here in $Cs_3Bi_2I_9$, the long-lived nature of the signal is because of the indirect band edge carriers, rather than due to excitons.

4.3.4 Energetics of $Cs_3Bi_2I_9$

To probe the energetics of $Cs_3Bi_2I_9$, ultraviolet spectroscopic (UPS) measurements were performed on the thin-films deposited onto FTO-coated glass substrate. As shown in Figure 4.10, the Fermi energy (E_F) was found to be 4.2 eV, determined by subtracting the cut-off energy from the excitation wavelength (21.22 eV). The ionization energy (IE), *i.e.*, the position of the VBM with respect to vacuum was determined to be 5.58 eV by extrapolating in the low binding energy region. In conjunction with the measured optical bandgap of 2.1 eV, $Cs_3Bi_2I_9$ appears to be weakly *p*-type semiconductor.

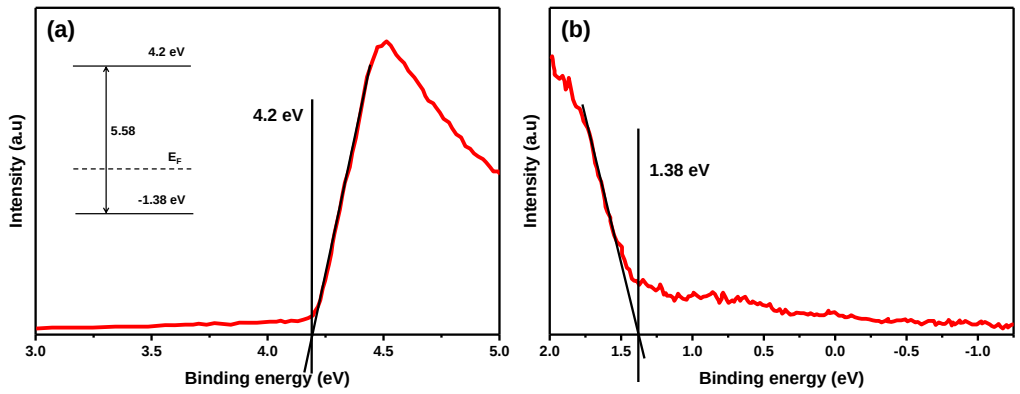

Figure 4.10: Energetics of $Cs_3Bi_2I_9$. (a) UPS spectrum at high binding region, the scale was set by subtracting the energy of the excitation wavelength (He I lamp, 21.22 eV). Inset: the energetics of $Cs_3Bi_2I_9$ using approximate VBM energy and estimated optical bandgap in Figure 4.4, (b) Linear extrapolation of the spectrum edge at low-binding energy region.

4.4 Photovoltaic Performance of $Cs_3Bi_2I_9$-based Solar cell

To investigate the effect of precursor solution concentration, three different concentrations were used to fabricate the PSCs. The corresponding *J-V* characteristics of the $Cs_3Bi_2I_9$-based PSCs are shown in Figure 4.11(a). Mesoporous device architecture with Spiro-OMeTAD as HTM was used for this investigation. With increasing precursor solution concentration from 0.25 M to 0.6 M, the V_{OC} of the PSCs increased from 0.5 V to 0.75 V, and the FF (fill factor) of the PSCs decreased gradually. The highest performance was obtained from 0.4 M concentration with a V_{OC} of 0.64 V, J_{SC} 0.25 mA.cm^{-2} and FF 0.43, leading to a 0.07% PCE at 1 sun illumination. The corresponding solar cell parameters of the PSCs are tabulated in Table 4.2. There is no apparent change in morphology of the thin-films albeit increase in platelet sizes with increasing precursor solution concentration as illustrated in Figure 4.12. The bigger platelets resulted in thicker capping layer in PSC devices (Figure

4.12). At high concentration, the capping layer thickness is the highest, which resulted in an increased series resistance, leading to low FF. Poor charge collection in the thick capping layer could be another reason for low performance of the PSC fabricated with 0.6 M concentration. At 0.25 M, the photocurrent density is mostly limited by the small fraction of absorbed light which resulted in poor PCE. Hence, the optimized precursor solution is kept 0.4 M for rest of the work on $Cs_3Bi_2I_9$-based PSCs.

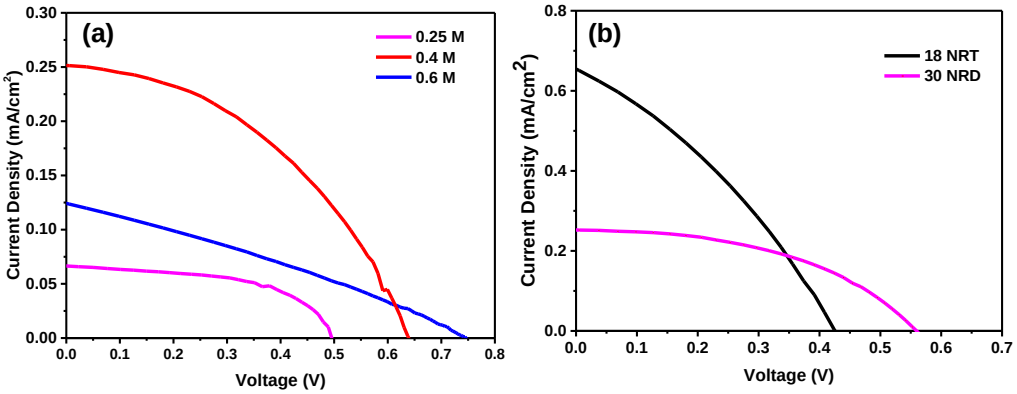

Figure 4.11: Photovoltaic performance of $Cs_3Bi_2I_9$-based PSCs. (a) Influence of precursor solution concentration on the *J-V* curves. (b) Effect of mesoporous TiO_2 layer on the *J-V* characteristics.

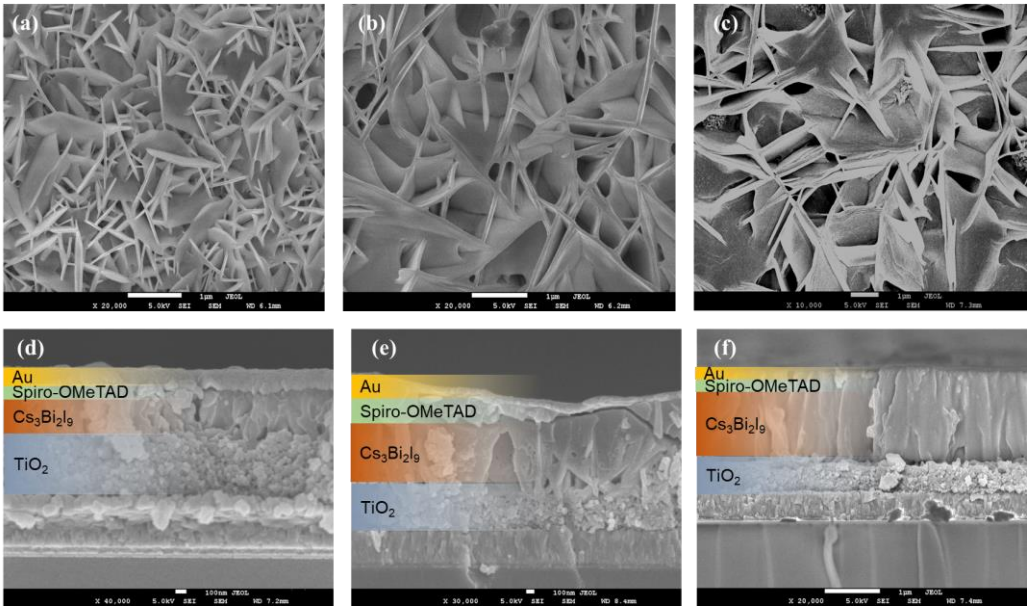

Figure 4.12: Scanning electron micrograph showing the morphology of $Cs_3Bi_2I_9$ fabricated with different precursor solution concentration. (a, b, c) Top surface of the thin-films deposited on mp-TiO_2, and (d, e, f) the device cross-section of $Cs_3Bi_2I_9$-based mesoscopic solar cells fabricated with (a, d) 0.25 M, (b, e) 0.4 M, and (c, f) 0.6 M precursor solution concentration.

Table 4.2: PV parameters of $Cs_3Bi_2I_9$-based mesoscopic solar cells fabricated with different precursor solution concentration

Precursor solution concentration	0.25 M	0.4 M	0.6 M
V_{OC} (V)	0.75	0.64	0.5
J_{SC} (mAcm^{-2})	0.12	0.25	0.07
FF (%)	29.90	42.78	56.73
PCE (%)	0.03	0.07	0.02

The mesoporous layers have a huge impact on the charge separation and transport of electrons in poor semiconducting materials [29]. To investigate the role of TiO_2 nanoparticles, two different types of TiO_2 paste: 18NR-T (average particle size 20 nm) and 30NR-D (average particle size 30 nm) were used to fabricate the mesoporous layer. Both pastes were bought from Dyesol (now Greatcell Solar), and the fabrication techniques were kept identical. Figure 4.11(b) represents the *J-V* characteristics for individual representative CBI-based PSCs employing different TiO_2 nanoparticles and Figure 4.13 shows the SEM of the PV device cross-sections. The highest current density (0.65 mA cm^{-2}) was obtained with mesoporous layer fabricated using 18NR-T TiO_2 paste; however, the V_{OC} is smaller as compared to PSCs fabricated using 30NR-D TiO_2 paste. Table 4.3 shows the PV parameters of the CBI-based PSCs fabricated with different TiO_2 paste. The higher photocurrent observed from smaller TiO_2 nanoparticles results from the likelihood of forming complete and continuous pathways through the absorber layer to the bottom contact.

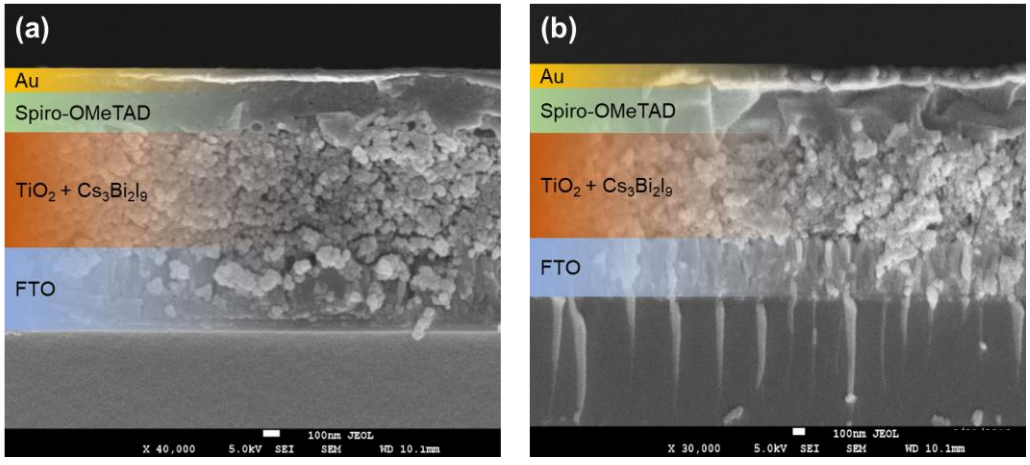

Figure 4.13: Cross-sectional scanning electron micrograph of $Cs_3Bi_2I_9$-based mesoscopic devices fabricated with (a) 18-NRT TiO_2 and (b) 30-NRD TiO_2 paste

Table 4.3: PV parameters of $Cs_3Bi_2I_9$-based mesoscopic solar cells fabricated with different TiO_2 paste

	18NR-T	30NR-D
V_{OC} (V)	0.43	0.56
J_{SC} ($mAcm^{-2}$)	0.65	0.25
FF (%)	32.98	46.76
PCE (%)	0.09	0.07

To investigate the effect of HTMs on the $Cs_3Bi_2I_9$-based PSCs, we employed three different HTMs such as Spiro-OMeTAD, PTAA (polytriarylamine), and PTPD (poly (N, N1-bis(4-butylphenyl)-N, N1-bis(phenyl)benzidine) as well as fabricated devices without any HTM. The ionization energies of all these HTMs overlapped well with the valence band energy of $Cs_3Bi_2I_9$ as illustrated in Figure 4.14(a). The energy levels of $Cs_3Bi_2I_9$ thin-films were calculated from UPS spectra. Spiro-OMeTAD is the most popularly used HTM in lead-based halide perovskites due to tunable charge transport using dopants. However, dissolution of $Cs_3Bi_2I_9$ by t-BP (tert-butyl pyridine) (one of the major components of Spiro-OMeTAD dopant) prevented the use of dopant in this work. Triarylamine-based PTAA is well known for its good hole transportability and stability in ambient atmosphere [30]. Organic polymer-based PTPD also exhibits good PV performances with lead-based halide perovskites due to efficient charge transfer [31]. The corresponding *J-V* characteristics CBI-based PSCs were illustrated in Figure 4.14(b). In all cases, Spiro-OMeTAD-based devices outperformed all other HTMs, although the HTMs exhibit good energy match with CBI. The maximum PCE was observed with Spiro-OMeTAD-based PSCs as higher photocurrent, photovoltage and fill factors were obtained. The PV parameters of the PSCs are listed in Table 4.4.

Interestingly, devices without any HTM shows a V_{OC} of ~0.7 V, but also suffer from poor photocurrent density and low fill factor which may be due to increased series resistance at the CBI/Au interface.

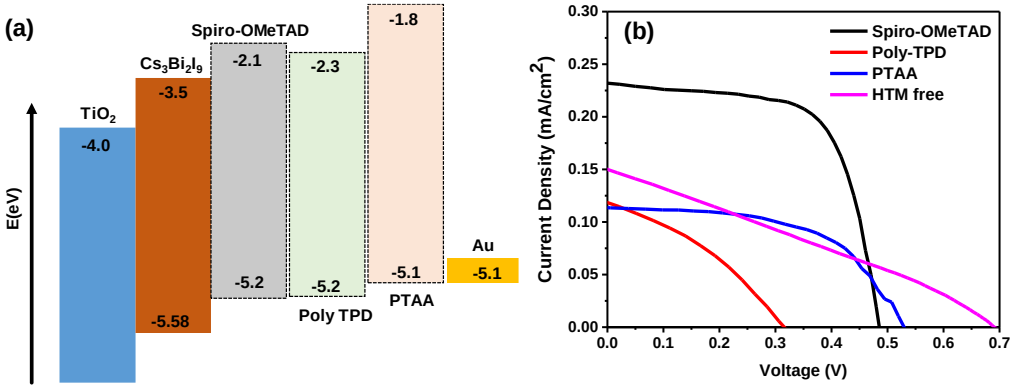

Figure 4.14: Energetics and PV performance of different HTMs. (a) Schematic energy levels of every component of CBI-based PSCs, (b) *J-V* characteristics of $Cs_3Bi_2I_9$-based PSCs with different HTMs. Spiro-OMeTAD, PTPD and PTAA were used as HTM in following structure: FTO/c-TiO_2/mp-TiO_2/$Cs_3Bi_2I_9$/HTM/Au; No HTM indicates the same device structure without any hole-transport materials between $Cs_3Bi_2I_9$ and Au.

Table 4.4: PV parameters of $Cs_3Bi_2I_9$-based mesoscopic solar cells fabricated employing different HTMs

	Spiro-OMeTAD	PTPD	PTAA	HTM free
V_{OC} **(V)**	0.49	0.32	0.53	0.69
J_{SC} **(mAcm^{-2})**	0.23	0.12	0.11	0.15
FF (%)	67.19	34.90	56.40	28.32
PCE (%)	0.08	0.01	0.03	0.03

4.5 Conclusions

Amongst three A-site cations, Cesium bismuth iodide ($Cs_3Bi_2I_9$) exhibits excellent stability under ambient atmosphere along with reasonable thin-film coverage when compared to $MA_3Bi_2I_9$ and $FA_3Bi_2I_9$. Hence, the investigations on optoelectronic and photovoltaic properties were carried out on $Cs_3Bi_2I_9$ as a prototype Bi-based perovskite. Steady-state photoluminescence spectroscopy resulted in poor PLQY along with short carrier lifetime (in ps range). The presence of defects in thin-films appears to be a significant bottleneck in obtaining high PLQY. The emission due to free carriers was found to be negligible by Cathodoluminescene spectroscopy. However, long-lived photogenerated carriers at the bandedge were observed in transient absorption spectroscopy. The functionality of $Cs_3Bi_2I_9$ in solar cells was also investigated in mesoscopic solar cell configuration. In producing $Cs_3Bi_2I_9$-based perovskite solar cells, a variety of HTM and ETL were explored. Nevertheless, PCEs of $Cs_3Bi_2I_9$-based solar cells were found to be poor, limited by poor photocurrent density. Considering the fact that free carriers should translate into photocurrent, the most plausible reason would be poor extraction of carriers due to natural quantum confinement effect in zero-dimensional electronic structure.

The photo-excited carriers in $Cs_3Bi_2I_9$ are relaxed and localized on the $[Bi_2I_9]^{3-}$ bioctahedra, by the presence of self-trapped excitons that eventually cooled down to ground state by defect-limited non-radiative recombination This behavior is in sharp contrasts with 3D lead halide perovskites, in which the octahedra are connected, and carriers are highly delocalized over many units. Although the role of organic cations on the optoelectronic properties is still under debate, we believed that $Cs_3Bi_2I_9$ represents the overall characteristics of $A_3Bi_2I_9$ family of compounds due to similar crystal structure and absorption spectroscopy and the results obtained in this work can be translated into other A-site cations as well.

References

[1] L.-M. Wu, X.-T. Wu, and L. Chen, "Structural overview and structure–property relationships of iodoplumbate and iodobismuthate," *Coord. Chem. Rev.,* vol. 253, pp. 2787-2804, 2009/12/01/ 2009.

[2] A. Cornia, A. C. Fabretti, R. Grandi, and W. Malavasi, "Structure ofcatena-(2-amino-1,3,4-thiadiazolium, 2-amino-1,3,4-thiadiazole bis(μ-iodo)-di-iodo-bismuth(III)," *J. Chem. Crystallogr.,* vol. 24, pp. 277-280, April 01 1994.

[3] W. Clegg, R. John Errington, G. A. Fisher, M. E. Green, D. C. R. Hockless, and N. C. Norman, "A Phosphine Complex of Bismuth(III): X-ray Crystal Structure of [PMe3H][Bi_2Br_7($PMe3)_2$]," *Chem. Ber.,* vol. 124, pp. 2457-2459, 1991.

[4] D. B. Mitzi, "Templating and structural engineering in organic–inorganic perovskites," *J. Chem. Soc., Dalton Trans.,* pp. 1-12, 2001.

[5] A. J. Lehner, D. H. Fabini, H. A. Evans, C.-A. Hébert, S. R. Smock, J. Hu, *et al.*, "Crystal and Electronic Structures of Complex Bismuth Iodides $A_3Bi_2I_9$ (A = K, Rb, Cs) Related to Perovskite: Aiding the Rational Design of Photovoltaics," *Chem. Mater.,* vol. 27, pp. 7137-7148, 2015/10/27 2015.

[6] D. B. Mitzi and P. Brock, "Structure and Optical Properties of Several Organic−Inorganic Hybrids Containing Corner-Sharing Chains of Bismuth Iodide Octahedra," *lnorg. Chem.,* vol. 40, pp. 2096-2104, 2001/04/01 2001.

[7] F. Lazarini, "Structure of diethylammonium enneaiododibismuthate(III)," *Acta Crystallographica Section C,* vol. 43, pp. 875-877, 1987.

[8] B. Chabot and E. Parthe, "$Cs_3Sb_2I_9$ and $Cs_3Bi_2I_9$ with the hexagonal $Cs_3Cr_2Cl_9$ structure type," *Acta Crysrallogr. B,* vol. 34, pp. 645-648, 1978.

[9] K. Eckhardt, V. Bon, J. Getzschmann, J. Grothe, F. M. Wisser, and S. Kaskel, "Crystallographic insights into $(CH_3NH_3)_3(Bi_2I_9)$: a new lead-free hybrid organic–inorganic material as a potential absorber for photovoltaics," *Chem. Commun.*, vol. 52, pp. 3058-3060, 2016.

[10] S. S. Shin, J. P. Correa Baena, R. C. Kurchin, A. Polizzotti, J. J. Yoo, S. Wieghold, *et al.*, "Solvent-Engineering Method to Deposit Compact Bismuth-Based Thin Films: Mechanism and Application to Photovoltaics," *Chem. Mater.*, vol. 30, pp. 336-343, 2018/01/23 2018.

[11] X. Huang, S. Huang, P. Biswas, and R. Mishra, "Band Gap Insensitivity to Large Chemical Pressures in Ternary Bismuth Iodides for Photovoltaic Applications," *J. Phys. Chem. C,* vol. 120, pp. 28924-28932, 2016/12/29 2016.

[12] M. Lyu, J.-H. Yun, M. Cai, Y. Jiao, P. V. Bernhardt, M. Zhang, *et al.*, "Organic–inorganic bismuth (III)-based material: a lead-free, air-stable and solution-processable light-absorber beyond organolead perovskites," *Nano Research*, vol. 9, 2016.

[13] C. Ni, G. Hedley, J. Payne, V. Svrcek, C. McDonald, L. K. Jagadamma, *et al.*, "Charge carrier localised in zero-dimensional $(CH_3NH_3)_3Bi_2I_9$ clusters," *Nat. Commun.*, vol. 8, p. 170, 2017/08/01 2017.

[14] J.-P. Correa-Baena, M. Saliba, T. Buonassisi, M. Grätzel, A. Abate, W. Tress, *et al.*, "Promises and challenges of perovskite solar cells," *Science*, vol. 358, pp. 739-744, 2017.

[15] M. T. Hörantner, T. Leijtens, M. E. Ziffer, G. E. Eperon, M. G. Christoforo, M. D. McGehee, *et al.*, "The Potential of Multijunction Perovskite Solar Cells," *ACS Energy Lett.*, vol. 2, pp. 2506-2513, 2017/10/13 2017.

[16] P. Gao, A. R. Bin Mohd Yusoff, and M. K. Nazeeruddin, "Dimensionality engineering of hybrid halide perovskite light absorbers," *Nat. Commun.*, vol. 9, p. 5028, 2018/11/28 2018.

[17] G. Xing, N. Mathews, S. Sun, S. S. Lim, Y. M. Lam, M. Grätzel, *et al.*, "Long-Range Balanced Electron- and Hole-Transport Lengths in Organic-Inorganic $CH_3NH_3PbI_3$," *Science,* vol. 342, pp. 344-347, 2013-10-18 00:00:00 2013.

[18] A. M. A. Leguy, Y. Hu, M. Campoy-Quiles, M. I. Alonso, O. J. Weber, P. Azarhoosh, *et al.*, "Reversible Hydration of $CH_3NH_3PbI_3$ in Films, Single Crystals, and Solar Cells," *Chem. Mater.*, vol. 27, pp. 3397-3407, 2015/05/12 2015.

[19] K. M. McCall, C. C. Stoumpos, S. S. Kostina, M. G. Kanatzidis, and B. W. Wessels, "Strong Electron–Phonon Coupling and Self-Trapped Excitons in the Defect Halide Perovskites $A_3M_2I_9$ (A = Cs, Rb; M = Bi, Sb)," *Chem. Mater.*, vol. 29, pp. 4129-4145, 2017/05/09 2017.

[20] B. G. Yacobi and D. B. Holt, "Cathodoluminescence," in *Cathodoluminescence Microscopy of Inorganic Solids*, ed Boston, MA: Springer US, 1990, pp. 55-88.

[21] B.-W. Park, B. Philippe, X. Zhang, H. Rensmo, G. Boschloo, and E. M. J. Johansson, "Bismuth Based Hybrid Perovskites $A_3Bi_2I_9$ (A: Methylammonium or Cesium) for Solar Cell Application," *Adv. Mater.*, vol. 27, pp. 6806-6813, 2015.

[22] T. Schmidt, K. Lischka, and W. Zulehner, "Excitation-power dependence of the near-band-edge photoluminescence of semiconductors," *Phys. Rev. B,* vol. 45, pp. 8989-8994, 04/15/ 1992.

[23] M. A. Reshchikov and R. Y. Korotkov, "Analysis of the temperature and excitation intensity dependencies of photoluminescence in undoped GaN films," *Phys. Rev. B,* vol. 64, p. 115205, 08/29/ 2001.

[24] R. Singh, R. J. Molnar, M. S. Ünlü, and T. D. Moustakas, "Intensity dependence of photoluminescence in GaN thin films," *Appl. Phys. Lett.*, vol. 64, pp. 336-338, 1994.

[25] H. Shi, R. Yan, S. Bertolazzi, J. Brivio, B. Gao, A. Kis, *et al.*, "Exciton Dynamics in Suspended Monolayer and Few-Layer MoS_2 2D Crystals," *ACS Nano,* vol. 7, pp. 1072-1080, 2013/02/26 2013.

[26] X. Wu, M. T. Trinh, and X. Y. Zhu, "Excitonic Many-Body Interactions in Two-Dimensional Lead Iodide Perovskite Quantum Wells," *J. Phys. Chem. C,* vol. 119, pp. 14714-14721, 2015/07/02 2015.

[27] Q. Cui, F. Ceballos, N. Kumar, and H. Zhao, "Transient Absorption Microscopy of Monolayer and Bulk WSe_2," *ACS Nano,* vol. 8, pp. 2970-2976, 2014/03/25 2014.

[28] M. Scholz, O. Flender, K. Oum, and T. Lenzer, "Pronounced Exciton Dynamics in the Vacancy-Ordered Bismuth Halide Perovskite $(CH_3NH_3)_3Bi_2I_9$ Observed by Ultrafast UV–vis–NIR Transient Absorption Spectroscopy," *J. Phys. Chem. C,* vol. 121, pp. 12110-12116, 2017/06/08 2017.

[29] T. Singh, A. Kulkarni, M. Ikegami, and T. Miyasaka, "Effect of Electron Transporting Layer on Bismuth-Based Lead-Free Perovskite $(CH_3NH_3)_3Bi_2I_9$ for Photovoltaic Applications," *ACS Appl. Mater. Interfaces,* vol. 8, pp. 14542-14547, 2016/06/15 2016.

[30] S. Mohamed, D. Demeter, J.-A. Laffitte, P. Blanchard, and J. Roncali, "Structure-properties relationships in triarylamine-based donor-acceptor molecules containing naphtyl groups as donor material for organic solar cells," *Sci. Rep.,* vol. 5, p. 9031, 03/12/online 2015.

[31] D. Zhao, M. Sexton, H.-Y. Park, G. Baure, J. C. Nino, and F. So, "High-Efficiency Solution-Processed Planar Perovskite Solar Cells with a Polymer Hole Transport Layer," *Adv. Energy Mater.,* vol. 5, p. 1401855, 2015.

Chapter 5*

Improving Photovoltaic Performance of $Cs_3Bi_2I_9$ Through Targeted Defect Passivation

This chapter is devoted to the theoretical investigations on $Cs_3Bi_2I_9$ by density functional theory (DFT) to elucidate the physical origin of poor photovoltaic performance and to complement the experimental results obtained in the previous chapter. The electronic bandgap of $Cs_3Bi_2I_9$ was found to be indirect in nature, and the flat bands near the bandgap resulted in heavy and anisotropic carrier effective mass, both of which are detrimental for high-performance PV compounds. The intrinsic the defect calculations also revealed the formation of mid-bandgap states in normal synthesis conditions. The vacancy of iodide (V_I) and Cs_{Bi} antisites were identified as the non-radiative recombination centres with low formation energies. Based on these studies, new formalism of experimental conditions was followed, which resulted in significant improvement of PCE in $Cs_3Bi_2I_9$-based mesoscopic solar cells.

*This chapter published substantially as Biplab Ghosh, Sudip Chakraborty, Hao Wei, Claude Guet, Shuzhou Li, Subodh Mhaisalkar, and Nripan Mathews. Poor Photovoltaic Performance of $Cs_3Bi_2I_9$: An Insight through First-Principles Calculations. *Journal of Physical Chemistry C* 121(32), 17062-17067 (2017). DOI: 10.1021/acs.jpcc.7b03501

5.1 Introduction

The excellent optoelectronic properties and defect tolerance of Pb-based halide perovskites are often attributed to $6s^2$ electrons in Pb^{2+}. However, despite having $6s^2$ electrons in the outer orbital in Bi^{3+}, the semiconducting properties of Bi-based iodide perovskites were found to be poor resulting in poor PV performance of $Cs_3Bi_2I_9$-based solar cells. The possible reasons are speculated to be the high concentration of defects and poor charge transport in the bulk material, as discussed in the previous chapter. This warrants an in-depth theoretical investigation to elucidate the structure-property correlation in $Cs_3Bi_2I_9$ perovskite. While there are numerous experimental techniques for identifying and characterizing defects, experiments often investigate only specific type of defect, limited by the respective spectroscopic technique, hence offering only isolated picture of the defects. Density functional theory (DFT), on the other hand, proved to be an excellent alternative for defect characterizations in semiconductors by employing a supercell structure with periodic boundary conditions. By calculating the formation energies of intrinsic defects, one can identify the most favourable defects during synthesis conditions. Hence, appropriate measures can be taken during synthesis condition to minimize the impact of the specific defects. To this end, the ability to engineer the intrinsic point defects in $Cs_3Bi_2I_9$ during its growth process to mitigate the effects of deleterious non-radiative recombination sites and tune its photovoltaic performance can be beneficial.

5.2 Crystal Structure Optimization

$Cs_3Bi_2I_9$ exhibits a hexagonal crystal symmetry at room temperature with the space group $P6_3/mmc$ and undergoes a ferroelastic phase transition to monoclinic structure at 220 K [1]. Since the room temperature phase is of primary interest in PV applications, we only considered the hexagonal crystal structure of $Cs_3Bi_2I_9$ in this study. The hexagonal structure can be considered as

a distorted and defect modulated face-sharing perovskite structure in which every third layer of octahedral Bi sites are depleted for charge compensation. Consequently, two neighboring $[BiI_6]^{3-}$ octahedron form a face-sharing $[Bi_2I_9]^{3-}$ bioctahedra which are separated by Cs^+ cations, eventually forming a 0D crystal structure (Figure 5.1). Within $[Bi_2I_9]^{3-}$ cluster, there are two types of Bi-I bonds: three bridging and six terminals. The bridging Bi-I bonds (3.246 Å) are longer compared to the terminal ones (2.923 Å). The I-Bi-I bond angle deviates from 90° (as for the case of conventional cubic perovskites) to smaller angle (Table 5.1).

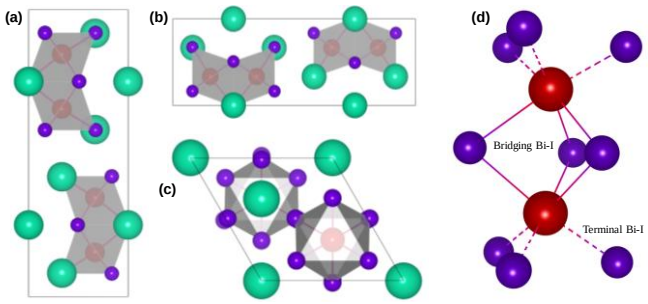

Figure 5.1: Schematic crystal structure of $Cs_3Bi_2I_9$ (red, green, and violet colors represent Bi, Cs, and I atoms) as seen along (a) a-axis, (b) b-axis and (c) c-axis. (d) $[Bi_2I_9]^{3-}$ bioctahedra with two different types of Bi-I bonds (crystal structures were rendered using VESTA).

Density functional theory (DFT) calculations for electronic structure of $Cs_3Bi_2I_9$ was performed using VASP. The generalized gradient approximation was used for the exchange-correlation function using the parameterizations of Perdew, Burke, and Ernzerhof (PBE) and the pseudopotentials are treated within the framework of Blochl's projected augmented wave (PAW) method. Table 5.1 lists the lattice constant, bond lengths and bond angles of the optimized crystal

structure of $Cs_3Bi_2I_9$, together with the reference structure. We observed a significant increase in volume in the optimized crystal structure with the largest deviation of ~5% was observed in c-axis. This discrepancy is due to the fact that the accuracy of calculations decreases due to relativistic effects. Furthermore, the hexagonal crystal structure of $Cs_3Bia_2I_9$ is a high-temperature phase, and DFT calculations do not take thermal effects into account. However, our results are in good agreement with the other reports with similar level of calculations [2, 3].

Table 5.1: Comparison between the reference and optimized $Cs_3Bi_2I_9$ crystal lattice parameters

Parameter		Optimized structure	Reference [4]
Lattice constant (Å)	a	8.618	8.412
	c	22.228	21.182
Volume (Å^3)		1429.728	1297.941
Bond length (Å)	Terminal Bi-I	2.994	2.923
	Bridging Bi-I	3.241	3.246
	Bi-Bi	4.111	4.050
Bong angle (°)	Bi-I-Bi	78.866	77.180

5.3 Electronic Bandstructure of $Cs_3Bi_2I_9$

There are different published reports on the experimental bandgap value of $Cs_3Bi_2I_9$. Machulin, *et al.* [1] reported a ~2.8 eV bandgap of $Cs_3Bi_2I_9$ single crystals. However, recent works by Lehner, *et al.* [5] and Park, *et al.* [6] estimated an indirect optical bandgap of 1.9 eV and 2.2 eV for $Cs_3Bi_2I_9$ respectively thin-films. Our experimental results also showed an indirect optical bandgap of 2.1 eV for $Cs_3Bi_2I_9$ thin-films. It should be noted here that the presence of a strong excitonic peak in the absorption spectrum often makes it difficult to extract the exact bandgap of low dimensional compounds such as is the case with $Cs_3Bi_2I_9$. Figure 5.2(a) illustrates the electronic bandstructure plot of $Cs_3Bi_2I_9$ as calculated by DFT. The effect of spin-orbit coupling (SOC) is also illustrated in that Figure. The bandstructure is calculated by walking through the high symmetry path which is shown in Figure 5.2(b). The Brillouin zone sampling data were collected from Bilbao Crystallographic Server [7]. The VBM is arbitrarily set at 0 eV and is located at M point. According to our calculations, the electronic bandgap is indirect in nature between Γ and M point. The calculated bandgap value is found to be 1.65 eV and 2.34 eV with and without SOC respectively. Though DFT calculations within GGA approximation can approximately estimate the experimental bandgap for $MAPbI_3$, similar calculations for other semiconductors generally do not provide an accurate bandgap estimation. The HSE06 type hybrid exchange-correlation functional has been found to be more accurate in predicting semiconductor bandgap. However, DFT calculations considering SOC, HSE06 and excitonic effect together would not be viable as far the computational expenses are concerned. Instead, we opted for optical absorption spectra calculation using different functionals to highlight the bandgap underestimation in PBE.

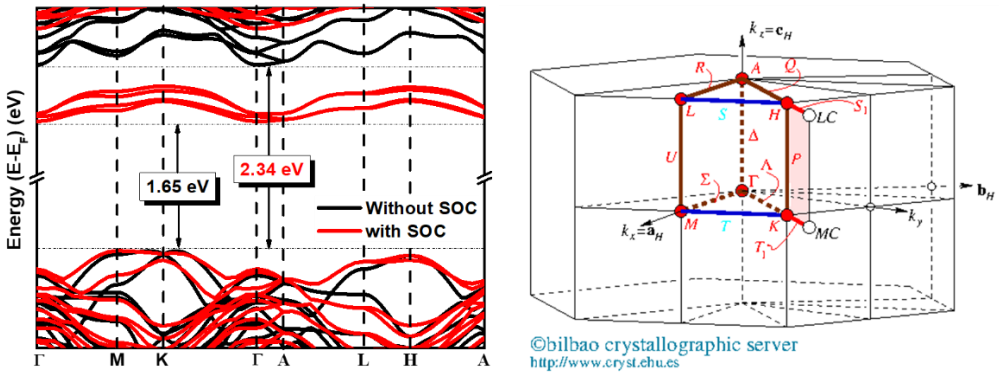

Figure 5.2: Bandstructure of $Cs_3Bi_2I_9$ along high-symmetry paths in the first Brillouin zone within GGA approximation using PBE functional. (right) First Brillouin zone of hexagonal lattice (adapted from Bilbao crystallographic server) showing high symmetry K-points used for bandstructure calculations.

A comparative investigation was conducted to determine the optical absorption spectra in three different combinations: i. GGA-PBE without spin-orbit coupling (SOC), ii. HSE06 without SOC and iii. HSE06 with SOC and illustrated in Figure 5.3(a). The first prominent peak of the optical response shows a blue shift towards the higher photon energy when we consider the hybrid functional without spin-orbit interaction. It is also interesting that the bandgap of $Cs_3Bi_2I_9$ with PBE functional without SOC and HSE06 with SOC consideration nearly matches with each other, similar to $MAPbI_3$ [8]. Therefore, PBE without SOC consideration would give us the approximate electronic bandgap values for $Cs_3Bi_2I_9$ due to the cancellation of errors created by standard DFT and that created by ignoring SOC, similar to what was reported for $MAPbI_3$ [9]. The mismatch in bandgap and optical absorption edge is most probably due to the lower energy excitonic peak which is common for this kind of low dimensional materials.

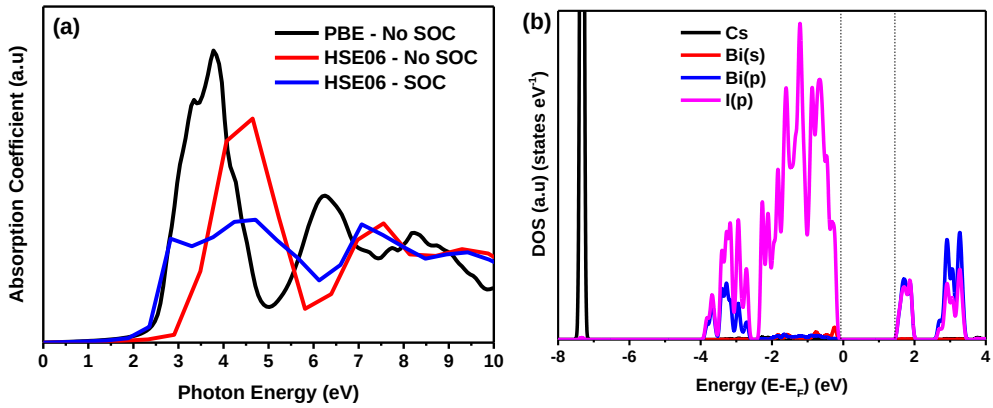

Figure 5.3: Simulated optical properties of $Cs_3Bi_2I_9$. (a) Calculated absorption spectra of $Cs_3Bi_2I_9$ with different functional treatment. (b) Comparison of projected density of states (PDOS) of $Cs_3Bi_2I_9$ calculated with Spin-orbit coupling (SOC) considerations.

5.4 Transport Properties

Apart from having a proper bandgap value, "good" photovoltaic materials must have reasonable transport properties, enabling an efficient charge collection and low electron-hole recombination centers. The effective mass of the carriers is a proper indication of transport properties of a semiconductor, as the smaller effective mass indicates high mobility of the carriers and vice-versa. The effective mass of electrons (m_e^*) and holes (m_h^*) are calculated considering the parabolic approximation of CBM and VBM according to

$$\frac{1}{m^*} = \frac{1}{\hbar^2}\frac{d^2E(k)}{dk^2} \quad (1)$$

where k is the crystal momentum vector. The calculated effective masses of holes and electrons at CBM and VBM are given in Table 5.2. The effective mass of holes and electrons are quite equivalent, indicating that $Cs_3Bi_2I_9$ may also exhibit ambipolar transport, like $MAPbI_3$. However, the values are quite large and anisotropic, originating from the flat band nature and low symmetry

of $Cs_3Bi_2I_9$. Thus, the carrier mobility expected to be quite low, resulting in poor charge transport. The flat nature of the CBM and VBM is also a stark contrast with $CH_3NH_3PbI_3$ bandstructure, in which large band dispersion provides smaller photocarrier effective mass and superior charge transport [10].

Table 5.2: Calculated effective mass of Electrons and Holes estimated from the calculated band structures

Effective mass (m*)	Γ→K	Γ→A	Γ→M	M→Γ	M→K
Electron	2.2	3.2	1.8		
Hole				2.27	16.3

5.5 Projected Density of States (PDOS)

Figure 5.3(b) illustrates the projected density of states (PDOS) close to VBM and CBM in $Cs_3Bi_2I_9$. The orbital contribution of Cs^+ ion can easily be recognized by the vertical line in the DOS; this indicates that the electronic states of Cs are fully localized in space, without substantial interaction with inorganic bioctahedra. Moreover, these states are far below the energy gap region that controls the photoconversion properties: the highest occupied Cs^+ level (HOMO) lies about ~7.3 eV below the VBM. Concerning the empty Cs states, they appear 3 eV above the CBM. From these results, a paramount feature of this compound emerges: Cs and inorganic $[Bi_2I_9]^{3-}$ cages are basically decoupled from the electronic viewpoint; therefore, Cs do not interfere with the active region of the perovskite. Its only role, regarding the electronic properties, is to donate one electron to the surrounding environment. Analogous observations have also been proposed for Pb-based perovskites where the

influence of the protonated cations is found to be insignificant on the VBM and CBM [11]. In addition, the valence band of $Cs_3Bi_2I_9$ is consists of the predominant contributions from *p* orbital of I and a little contribution from Bi(*s*) orbitals. The CBM is composed of nearly equal contribution from I(*p*) and Bi(*p*) orbitals. In comparison, the CBM of $MAPbI_3$ is composed of mainly Pb(*p*) orbitals.

5.6 Defect Characteristics

In order to fully unravel the defect characteristics in $Cs_3Bi_2I_9$, we followed the approach of Yin, *et al.* [11] who showed that point defects creating deep states in $MAPbI_3$ have high formation energies, which would preclude the probability of non-radiative recombination. Defects with low formation energies are found to have transition energies close to VBM and CBM in $CH_3NH_3PbI_3$. This "unusual defect physics" was claimed to explain the exceptional optoelectronic properties of Pb-halide perovskites. We characterized all the possible intrinsic point defects in $Cs_3Bi_2I_9$ and their transition energies in the bandgap to understand the role of defects in low dimensional Bi-based perovskites.

In supercell approach, the positions of the defects were chosen based on symmetry inequivalence. For more than one symmetry equivalent positions, we calculated defect formation energy for both positions and chose for the lowest energy state. For interstitial defects, the atom is kept at the centre of the supercell which was followed by full relaxation of the supercell. The detailed calculation method for defect formation energy can be found in the experimental section. In short, we computed the enthalpy of the bulk constituents as well as the secondary phases and using the thermodynamic boundary conditions, determined the thermodynamic stability region for $Cs_3Bi_2I_9$. We undertook the following methodology to define the range of the chemical potentials:

I. The chemical potential of the respective elements (Cs, Bi, I) should be lower than that of the bulk counterparts in equilibrium, otherwise, it would precipitate in the elemental phase:

$$\mu_{Cs} \leq \mu_{Cs[bulk]} = 0, \mu_{Bi} \leq \mu_{Bi[bulk]} = 0 \; and \; \mu_I \leq \mu_{I[bulk]} = 0 \quad (2)$$

II. The conditions for the formation of secondary phases (CsI, BiI_3) can be expressed as

$$\mu_{Cs} + \mu_I \leq \Delta H(CsI) = -1.14 \; eV \quad (3)$$

$$\mu_{Bi} + 3\mu_I \leq \Delta H(BiI_3) = -1.74 \; eV \quad (4)$$

III. In thermodynamic equilibrium condition, the formation enthalpy of $Cs_3Bi_2I_9$, which is stable in solid phase and the chemical potentials of the constituent atoms need to be equal.

$$3\mu_{Cs} + 2\mu_{Bi} + 9\mu_I = \Delta H(Cs_3Bi_2I_9) = -13.7 \; eV \quad (5)$$

The chemical potential corresponding to Bi and I that are satisfying *Eq. 2-5* are shown as grey region in Figure 5.4, and the chemical range is the boundary of the equilibrium growth conditions for $Cs_3Bi_2I_9$. Any point, which is out of this region, will lead to the formation of secondary phases during synthesis of $Cs_3Bi_2I_9$. The dissociation energy of $Cs_3Bi_2I_9$ defined as 3×E(CsI) + 2×E(BiI_3) – E($Cs_3Bi_2I_9$), is about 6.8 eV, which suggests the high stability of this compound. The broad stability range for $Cs_3Bi_2I_9$ and the large dissociation energy also indicate little influence of the growth conditions on the phase, unlike $CH_3NH_3PbI_3$ in which the stability region is quite narrow [11].

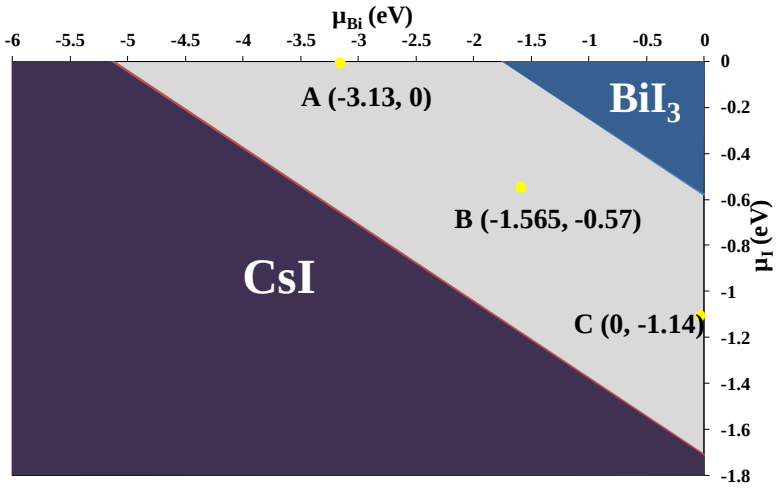

Figure 5.4: Calculated thermodynamic stability region for equilibrium growth of $Cs_3Bi_2I_9$.

We considered all the possible point defects in $Cs_3Bi_2I_9$ keeping the chemical potential within the stability range (Figure 5.4). The chemical potential points are taken at the center of the stability range which could give the three different stoichiometric conditions such as Bi-rich/I-poor conditions (point C), moderate conditions (point B), and I-rich/Bi-poor conditions (point A). Table 5.3 lists the formation energies of three vacancies (V_I, V_{Cs}, V_{Bi}), three interstitials (i_{Cs}, i_{Bi}, i_I), two cation substitution (Cs_{Bi}, Bi_{Cs}) and four antisites (Cs_I, Bi_I, I_{Bi}, I_{Cs}) type of defects in $Cs_3Bi_2I_9$ compound. At Bi-rich/I-poor region (point C) and moderate region (point B), the dominant types of defects are iodine vacancies with lowest formation energies. On the other hand, at I-rich/Bi-poor condition (point A), Cs_{Bi} cation substitution has the lowest formation energy. Apart from Cs_{Bi} substitution, all other Bi-type of defects have high formation energy, possibly due to the strong covalent bonding during the Bi-I dimer formation.

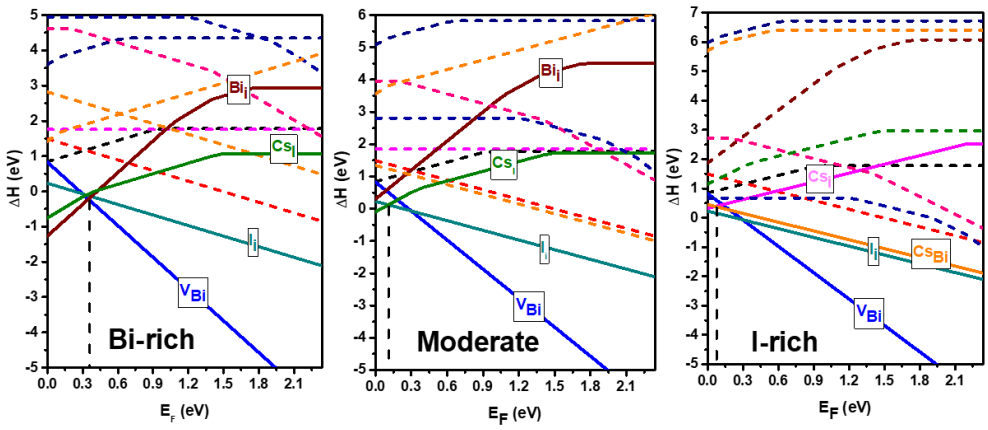

Figure 5.5: Calculated formation energy of defects as a function of fermi energy at three different stoichiometric conditions (Bi-rich, moderate, and I-rich). The bandgap is calculated using GGA approximation with PBE functional.

Figure 5.5 depicts the formation energy of the possible point defects as a function of Fermi energy. Unlike $MAPbI_3$ which shows a transition from p-type to n-type conductivities, $Cs_3Bi_2I_9$ exhibits p-type conductivities in all the stoichiometric regions [11]. The transition level of the defects indicates whether the defect can accept or donate electrons. A defect with a deep transition level usually acts as Shockley-Read-Hall non-radiative recombination centres, and the defects with shallow levels usually control the mobility of the charge carriers. As illustrated in Figure 5.6, among the three possible vacancies, V_{Bi} and V_I exhibit deep transition level in the bandgap region. However, the formation energy associated with the V_{Bi} is quite high as compared to V_I, which implies that V_I is the most prominent defects in the thin-films. On the other hand, V_{Cs} can act as an acceptor as the transition level lies near the vicinity of the VBM; however, its contribution would be minimal as the formation energy of the defect is quite high. The cation substitution Cs_{Bi} has low formation energy as well it creates two transition level: $\epsilon_1(0/1-)$ which is shallow acceptor and $\epsilon_2(1-/2-)$ which is deep acceptor. However, another cation substitution, Bi_{Cs}

has high formation energy which would prohibit from forming any deep mid-bandgap states. Although, most of the antisite and interstitial defects also form deep bandgap states, the probability of antisite defect formation is less due to high formation energy. It is interesting to note that although Cs^+ cations are not directly involved in optoelectronic properties, they can create deep states of energy level inside the bandgap, in contrast to $CH_3NH_3PbI_3$ in which methylammonium ions do not create additional gap states. The tendency for Cs to contribute to sub-bandgap states have been borne out by calculation in $CsPbBr_3$ [12] and $Cs_2AgBiBr_6$ [13]. Based on these considerations, organic-inorganic $(CH_3NH_3)_3Bi_2I_9$ may have better defect tolerance properties as compared to inorganic $Cs_3Bi_2I_9$. The tendency of Cs related defects to form, would also have implications for ionic transport within these semiconductors.

Table 5.3: The defect formation energies (eV) of the neutral defects in $Cs_3Bi_2I_9$ at chemical potential points A, B, C as shown in Figure 5.4

	V_{Cs}	V_{Bi}	V_I	Cs_i	Bi_i	I_i	Cs_{Bi}	Bi_{Cs}	Cs_I	I_{Cs}	I_{Bi}	Bi_I
A	1.60	1.34	1.78	2.52	6.07	2.47	0.56	6.72	2.97	2.72	0.67	6.40
B	2.27	2.90	1.21	1.85	4.51	3.04	1.46	5.83	1.73	3.96	2.81	4.27
C	2.36	4.47	0.64	1.76	2.94	3.61	2.93	4.35	1.07	4.62	4.94	2.13

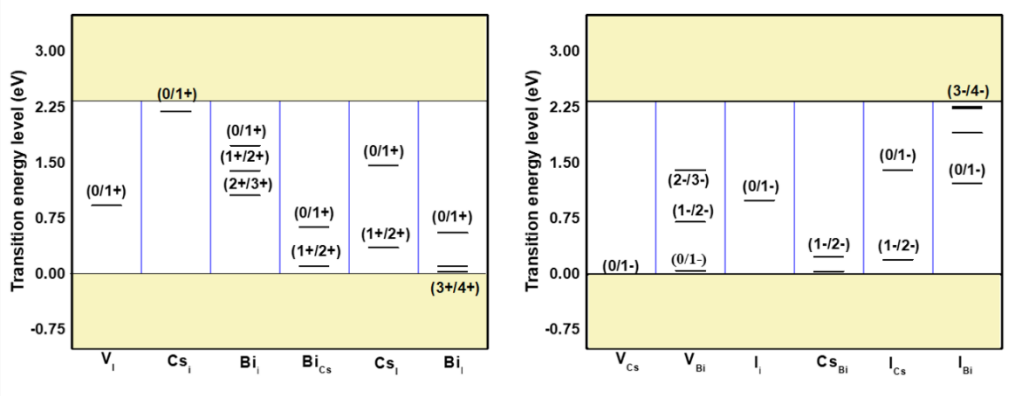

Figure 5.6: Calculated transition energy levels of various intrinsic defects. The white region represents the bandgap.

5.7 Role of Crystal Structure on Defect Properties

The role of defects is very critical for photovoltaics, as the formation of defects is inevitable in thin-films synthesis conditions necessary for device fabrication. They create energy states within the bandgap, leading to possible electron-hole recombination and degradation of the photovoltaic performances. The "superior optoelectronic properties" of $MAPbI_3$ are often attributed to its excellent defect tolerant properties. For example, the formation energy of V_I in $MAPbI_3$ is found to be the smallest of the intrinsic defects, and therefore most likely to develop during synthesis [11]. However, V_I also acts as a shallow donor in $MAPbI_3$, thus contributing to charge transport only, rather than non-radiative recombination center. Although the absolute values of the formation energies of defects in $MAPbI_3$ vary depending on the approximations and functionals, the benign nature of point defects is now universally accepted. The existing explanation for this defect tolerant property is primarily based on the unusual VBM and CBM characteristics of $MAPbI_3$ [14, 15]. The antibonding nature drives the VBM to the higher energies than the interacting atomic orbitals. Any cation vacancies in the vicinity of valence band would now resonate with the VBM and free the

bandgap from the defects. The donor vacancies, on the other hand, form near the CB and remain in resonance with the CBM due to the strong spin-orbit effect of Pb-I, which pulls down the CBM, thus prevents deep bandgap states. All these criteria are met in Bi-based perovskites, *i.e.,* the presence of heavy elements and the partially oxidized Bi^{3+}, resulting in antibonding characteristics in the band-edge. Nevertheless, the presence of defects, in particular, V_I is prominent as a mid-bandgap state. One of the most plausible explanations of this behavior is the low-dimensional crystal structure of Bi-based iodide perovskites. Previously, the PDOS plot showed that there is significant hybridization between Bi(*s*), Bi(*p*), and I(*p*). For a clearer picture about the nature of chemical bonding, the band decomposed charge density near VBM and CBM is shown in Figure 5.7. From these figures, it is obvious that valence band and conduction band of $Cs_3Bi_2I_9$ are both antibonding in nature. Interestingly, the interaction between two Bi atoms are also strongly covalent in nature, and each Bi atom has six-fold coordination with iodine atoms. In addition, the interactions between these Bi atoms and the bridging iodine atoms are also strong, while the terminal iodine has little influence on bonding hybridizations. As a consequence, the iodine vacancies are more likely to occur at the terminal sites due to weak bonding, which would further bring the Bi atoms closer together, leading to a stronger orbital hybridization. Despite the energy costs of the structural reorganization, the formation of stronger Bi-Bi bonds significantly reduces the overall energy of the system and energetically favors the trapping of electrons. In comparison, the Pb-Pb bonds in $MAPbI_3$ are considerably weaker due to their longer bond length as compared to the distorted Bi-bioctahedra. This scenario is quite similar to Ge-based iodide perovskites which also exhibit deep trapping of V_I type defects [16]. Therefore, the presence of heavy elements that are partially oxidized may not be sufficient conditions for defect tolerant behavior. Since the hybridizations also depend on the crystal structure, as in the case of $Cs_3Bi_2I_9$, it would be essential to

understanding the chemical and crystal structure in the design of defect tolerant materials. A similar correlation can be found in TlBr in which V_{Br} acts as shallow donor in simple cubic TlBr, while V_{Br} creates deep bandgap states in rocksalt structure [17].

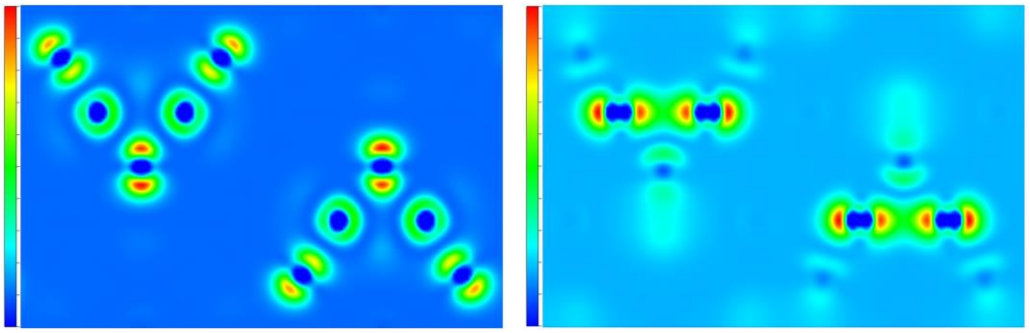

Figure 5.7: Band decomposed charge density near VBM (left) and CBM (right) of $Cs_3Bi_2I_9$ along (110) plane of a unit cell.

Our study, therefore, reveals the significant differences in electronic structure and properties between conventional Pb-based perovskites and Bi-based perovskites. We examined the important factors for good PV material by first-principle calculations. The electronic bandstructure of $Cs_3Bi_2I_9$ indicates the heavy effective mass of the carriers along with large indirect bandgap that would exclude its use in single junction solar cell. However, the main concern is the defect characteristics of these materials. Many defects with low formation energy form deep level states in the bandgap that acts as recombination centers in PV applications. Although the compound was initially thought to be defect tolerant [18], our calculations suggest otherwise. In general, based on our first principle calculations, we can suggest that the presence of deep-level defects can be a significant problem for the performance of the Bi-based ternary halide perovskites in the PV applications. It should be noted here that our study is

limited to the intrinsic point defects present in $Cs_3Bi_2I_9$, which does not include the possibility of defect passivation by external doping or non-equilibrium synthesis that could lead to better performance of the same.

5.8 Defect Passivation for Improved PV

The first principle calculations on $Cs_3Bi_2I_9$ revealed that the most likely defect to form during synthesis is V_I and Cs_{Bi} which can be retarded during synthesis in iodine-rich conditions. Since $Cs_3Bi_2I_9$ does not exhibit the typical defect tolerant properties, we continued our investigations into the passivation of these defects. For this purpose, we modified our precursor solutions with excess BiI_3 that would provide an iodine-rich condition. Moreover, the excess BiI_3 was also expected to prevent the Cs_{Bi} antisites. To test our hypothesis, we conducted detailed investigations on $Cs_3Bi_2I_9$ thin-films with varying excess BiI_3 concentrations and their effect on the photovoltaic properties.

5.8.1 Structural and Optical Characterizations

The thin-films fabricated with different amount of excess BiI_3 were characterized by XRD, UV-Visible and luminescence spectroscopy. Figure 5.8(a) shows the powder XRD patterns of the respective compositions. Powders of different stoichiometric ratio were collected after the precursor solution was drop-casted on the glass substrate and followed by annealing in vacuum oven at 100 °C for 24 hrs. Interestingly, there is no noticeable change in peak positions or the peak intensities of the reflections until the addition of 20% excess BiI_3, signifying no change in crystal structure. Further increase in BiI_3 in the precursor solution resulted in formation of secondary peaks of BiI_3. This observation is also confirmed by presence of another absorption peak near 1.7 eV as for 30% excess BiI_3 as illustrated in Figure 5.8(b). The morphology of the thin-films also remained unchanged even after adding excess BiI_3 in the precursor solution concentration as shown in Figure 5.9. To confirm the

absence of any impurity phases, the atomic concentration was estimated using energy dispersive x-ray spectroscopic (EDX) study. Table 5.4 shows the atomic percentage in the thin-films fabricated with different BiI_3 concentration. For a reference, we included the results from single crystal $Cs_3Bi_2I_9$ also. Within the limitations of EDX, there are no drastic changes in the composition variation, rather the concentration of iodine atoms apparently increased with excess BiI_3 addition.

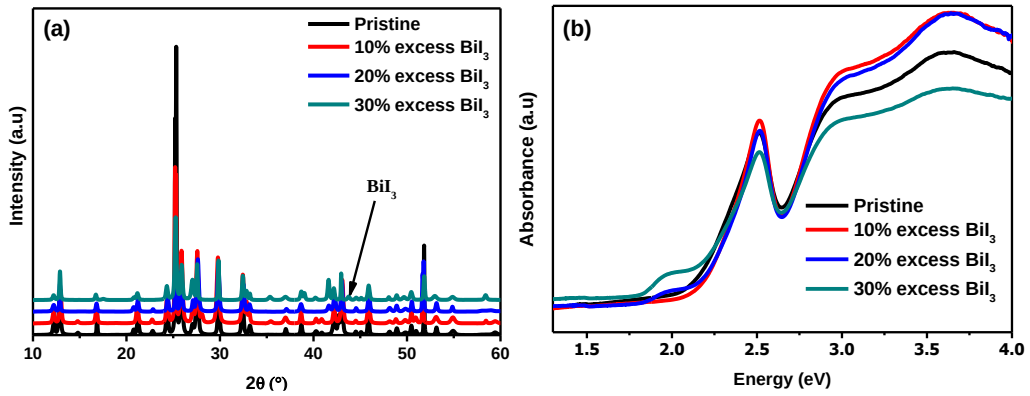

Figure 5.8: Photophysical characterizations of $Cs_3Bi_2I_9$ thin-films with varied BiI_3 concentration. (a) Powder XRD patterns of $Cs_3Bi_2I_9$ produced by varying BiI_3 concentration in precursor solution. Data are shifted along Y-axis for easier comparison. (b) UV-Vis spectra of thin-films fabricated with different BiI_3 compositions in precursor solution.

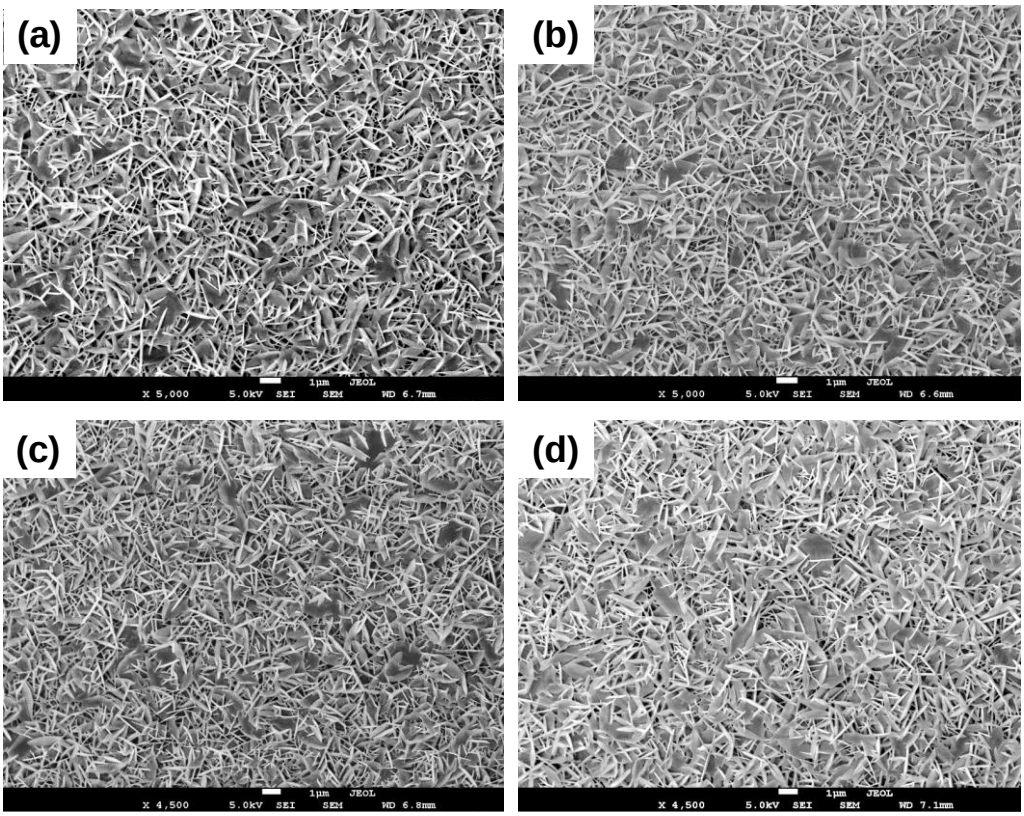

Figure 5.9: SEM morphology of thin-films showing (a) pristine $Cs_3Bi_2I_9$, (b) 10% excess BiI_3, (c) 20% excess BiI_3, and (d) 30% excess BiI_3. The films were deposited on mesoporous TiO_2 layer.

Table 5.4: Atomic concentration of $Cs_3Bi_2I_9$ single crystal and thin-films fabricated from different BiI_3 concentration

	Expected (%)	Single crystal (%)	Stoichiometric (%)	20% excess BiI_3 (%)	30% excess BiI_3 (%)
I	64.29	63.75	62.01	63.14	66.61
Cs	21.43	20.99	24.74	19.03	18
Bi	14.29	15.26	13.25	17.84	15.39

The impact of excess BiI_3 was further investigated qualitatively using luminescence spectroscopy as this technique directly correlate with the optoelectronic properties. Figure 5.10(a) shows the PL spectra from $Cs_3Bi_2I_9$ thin-films with varying BiI_3 concentration. As the PLQY of the thin films remained low and emission was broad in nature, quantitative analysis using photoluminescence was difficult. Nevertheless, the increase in intensity can be correlated with passivation of non-radiative trap states that are inherently present in $Cs_3Bi_2I_9$. The similar results can also be observed with CL measurement (Figure 5.10(b)) in which the emission is red shifted with addition of excess BiI_3. There may be formation of small BiI_3 domains in the $Cs_3Bi_2I_9$ with a smaller bandgap, which is quite difficult to detect by conventional XRD at low concentration and become prominent at a higher fraction as revealed by XRD pattern of 30% excess BiI_3. The decrease in CL bandgap at 30% excess BiI_3 also supports the formation of BiI_3, which lowers overall bandgap of the compounds like compound semiconductors such as $Al_xGa_{1-x}As$. Hence, the excess BiI_3 is most probably going inside the trap states and the structural disorders that are present in $Cs_3Bi_2I_9$.

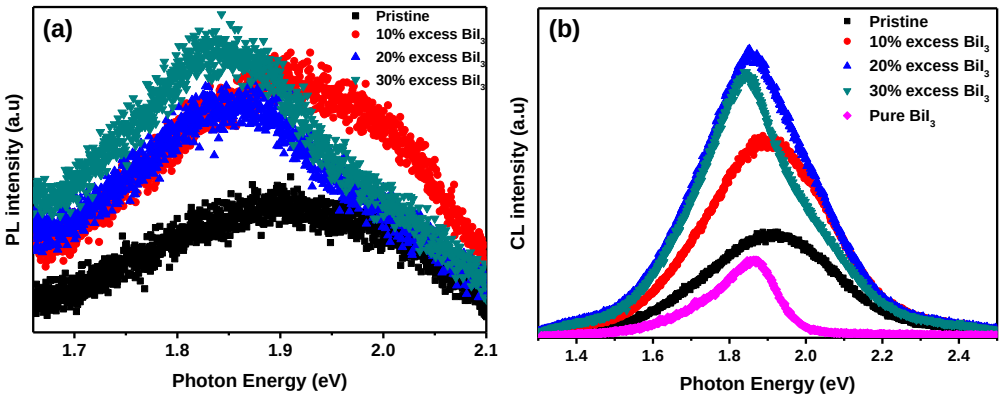

Figure 5.10: Luminescence spectra of $Cs_3Bi_2I_9$ thin-films. (a) PL, and (b) CL spectra (I_b = 0.2 nA) of $Cs_3Bi_2I_9$ thin-films with varying BiI_3 concentration.

5.8.2 Photovoltaic Performances

To realize the impact of the defect passivation on the PV performances, mesoscopic solar cells with a structure of FTO/c-TiO_2/mp-TiO_2/$Cs_3Bi_2I_9$/Spiro-OMeTAD/Au were fabricated. The absorber layers were produced from precursor solutions of varying BiI_3 concentrations. Rest of the layers were fabricated as described earlier. The typical cross-section SEM images of the solar cells are shown in Figure 5.11. The thickness of the absorber layer across different precursor solution concentration remained same, indicating similar light absorption under operating conditions. The *J-V* responses of the solar cells are shown in Figure 5.12(a) and Table 5.5. It can be observed that with increasing BiI_3 concentration in precursor solution, the photocurrent density increased till it reached a maximum value at 20% excess BiI_3. From less than 0.2 mA cm^{-2} photocurrent density that is achieved from stoichiometric precursor solution, we can reach more than 0.65 mA cm^{-2} photocurrent density with 20% excess BiI_3 addition. The best photovoltaic performance was obtained with 20% excess BiI_3 addition with photovoltaic parameters: V_{OC} = 0.49 V, J_{SC} = 0.67 mA cm^{-2} and FF = 63.6%, which resulted in 0.21% power conversion efficiency. However, with further increase in BiI_3 concentration, the PCE of the solar cell devices deteriorate. Figure 5.12(b) graphically illustrates the change in V_{OC} and J_{SC} along the different amount of excess BiI_3 concentration. The V_{OC} continuously decreases with increasing BiI_3 concentration in the precursor solution which is most likely due to reduction of series resistance across the solar cells. At high concentration, the appearance of secondary phases might be contributing in the increased recombination, leading to the reduction of V_{OC}. The secondary phase is also responsible for the reduction in J_{SC} at very high BiI_3 concentration (more than 20% excess BiI_3). The incident photon to current conversion efficiency was shown in Figure 5.13. The integrated current density matches well with the J_{SC} from the solar cells. With increasing BiI_3 concentration, the conversion efficiency (EQE) also

increases, indicating the reduction of defect states in the absorber layer.

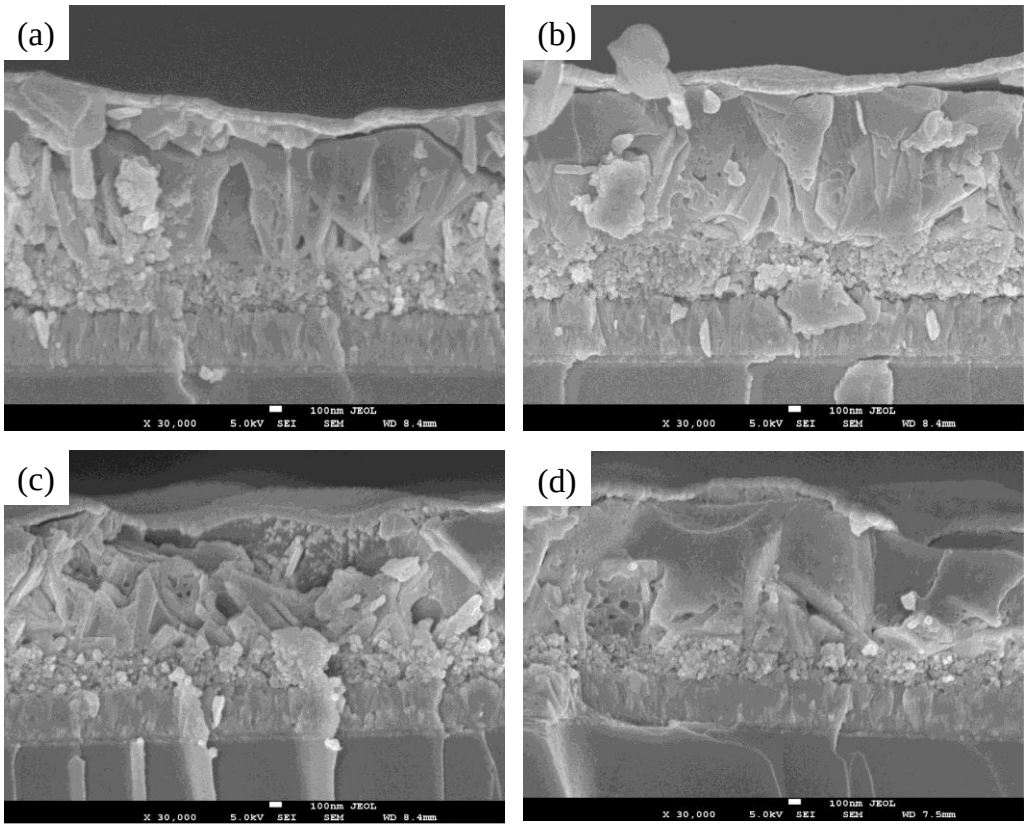

Figure 5.11: Cross-sectional SEM of $Cs_3Bi_2I_9$-based mesoscopic solar cells fabricated with (a) stoichiometric, (b) 10% excess BiI_3, (c) 20% excess BiI_3, and (d) 30% excess BiI_3 in precursor solution.

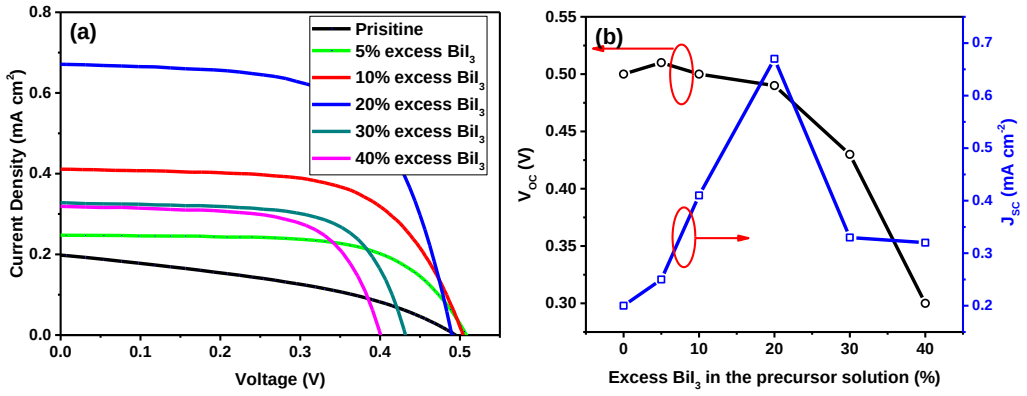

Figure 5.12: PV properties of $Cs_3Bi_2I_9$-based solar cells. (a) *J-V* characteristics of $Cs_3Bi_2I_9$ based mesoscopic solar cell with different precursor solution stoichiometry, (b) Change in V_{OC} and J_{SC} with excess BiI_3 concentration in precursor solution.

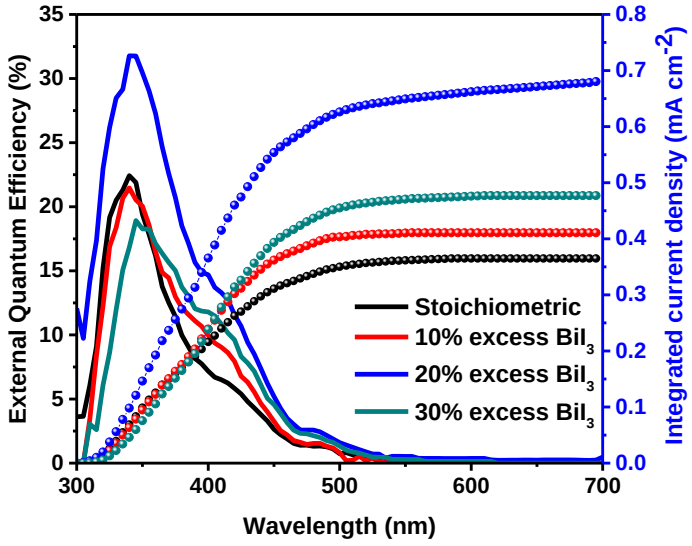

Figure 5.13: Incident current-to-photon conversion efficiency of mesoscopic $Cs_3Bi_2I_9$-based solar cells fabricated with different precursor solution compositions.

Table 5.5: *J-V* parameters of $Cs_3Bi_2I_9$-based mesoscopic solar cell with different precursor solution compositions

	V_{OC} (V)	J_{SC} (mA/cm^2)	FF (%)	PCE (%)
Pristine $Cs_3Bi_2I_9$	0.5	0.2	38.9	0.04
5% excess BiI_3	0.51	0.25	65.3	0.08
10% excess BiI_3	0.5	0.41	63.1	0.13
20% excess BiI_3	0.49	0.67	63.6	0.21
30% excess BiI_3	0.43	0.33	70.2	0.1
40% excess BiI_3	0.4	0.32	68.5	0.09

Although the device performances are not promising for efficient photovoltaics, there is a clear indication of improvement of the materials as well as its properties that are important for optoelectronic applications by defect engineering. Hence, the improvement of photovoltaic performance with a small amount of excess BiI_3 addition can be correlated with the passivating the intrinsic defects or structural disorder, as revealed by our simulation results.

5.9 Conclusions

In conclusion, we systematically investigated $Cs_3Bi_2I_9$ by utilizing density functional theory (DFT) to highlight the important parameters of PV performances. The electronic bandstructure calculation revealed an indirect bandgap of ~2 eV, which itself is large for an efficient single junction solar cells. Moreover, the flat band nature of CBM and VBM indicates the heavy effective mass of the carriers, leading to poor charge transport across the solar cell devices. Most importantly, intrinsic defect characterizations revealed that

$Cs_3Bi_2I_9$ might not be a defect tolerant compound as previously thought of.

Nevertheless, as indicated from the calculation results, the optoelectronic properties of $Cs_3Bi_2I_9$ can be improved by synthesizing in excess BiI_3 environment. Two major types of defects such as V_I and Cs_{Bi} most likely to be passivated by addition of excess BiI_3 as revealed by our experimental investigations. The defect passivation by different stoichiometric conditions is very well reflected in the PV performances. The short-circuit current density (J_{SC}) improved more than three times when the films were fabricated with 20% excess BiI_3 precursor solution, keeping the other variable unchanged. Nevertheless, the PCE of the solar cells remains quite low for practical use in PV applications. Hence, based on all the above results, we conclude that poor charge transport and intrinsic defects may be the possible reasons for low performance of the $Cs_3Bi_2I_9$-based solar cell. Beyond our findings above, further enhancement in performance in Bi-based solar cell can be expected by moving towards 3-D electronic structure which offers better charge transport properties than molecular structure of $Cs_3Bi_2I_9$.

References

[1] V. F. Machulin, F. V. Motsnyi, O. M. Smolanka, G. S. Svechnikov, and E. Y. Peresh, "Effect of temperature variation on shift and broadening of the exciton band in $Cs_3Bi_2I_9$ layered crystals," *Low Temp. Phys.,* vol. 30, pp. 964-967, 2004.

[2] S. S. Shin, J. P. Correa Baena, R. C. Kurchin, A. Polizzotti, J. J. Yoo, S. Wieghold, *et al.*, "Solvent-Engineering Method to Deposit Compact Bismuth-Based Thin Films: Mechanism and Application to Photovoltaics," *Chem. Mater.,* vol. 30, pp. 336-343, 2018/01/23 2018.

[3] X. Huang, S. Huang, P. Biswas, and R. Mishra, "Band Gap Insensitivity to Large Chemical Pressures in Ternary Bismuth Iodides for Photovoltaic Applications," *J. Phys. Chem. C,* vol. 120, pp. 28924-28932, 2016/12/29 2016.

[4] O. Lindqvist, G. Johansson, F. Sandberg, and T. Norin, "Crystal Structure of Caesium Bismuth Iodide, $Cs_3Bi_2I_9$," *Acta Chem. Scand,* vol. 22, pp. 2943-2952, 1968.

[5] A. J. Lehner, D. H. Fabini, H. A. Evans, C.-A. Hébert, S. R. Smock, J. Hu, *et al.*, "Crystal and Electronic Structures of Complex Bismuth Iodides $A_3Bi_2I_9$ (A = K, Rb, Cs) Related to Perovskite: Aiding the Rational Design of Photovoltaics," *Chem. Mater.,* vol. 27, pp. 7137-7148, 2015/10/27 2015.

[6] B.-W. Park, B. Philippe, X. Zhang, H. Rensmo, G. Boschloo, and E. M. J. Johansson, "Bismuth Based Hybrid Perovskites $A_3Bi_2I_9$ (A: Methylammonium or Cesium) for Solar Cell Application," *Adv. Mater.,* vol. 27, pp. 6806-6813, 2015.

[7] M. I. Aroyo, D. Orobengoa, G. de la Flor, E. S. Tasci, J. M. Perez-Mato, and H. Wondratschek, "Brillouin-zone database on the Bilbao Crystallographic ServerThis article forms part of a special issue dedicated to mathematical crystallography, which will be published as a

virtual special issue of the journal in 2014," *Acta Crystallogr. A,* vol. 70, pp. 126-137, 2014.

[8] L. Lang, J.-H. Yang, H.-R. Liu, H. J. Xiang, and X. G. Gong, "First-principles study on the electronic and optical properties of cubic ABX_3 halide perovskites," *Phys. Lett. A,* vol. 378, pp. 290-293, 1/10/ 2014.

[9] J. M. Azpiroz, E. Mosconi, J. Bisquert, and F. De Angelis, "Defect migration in methylammonium lead iodide and its role in perovskite solar cell operation," *Energy Environ. Sci.,* vol. 8, pp. 2118-2127, 2015.

[10] G. Giorgi, J.-I. Fujisawa, H. Segawa, and K. Yamashita, "Small Photocarrier Effective Masses Featuring Ambipolar Transport in Methylammonium Lead Iodide Perovskite: A Density Functional Analysis," *J. Phys. Chem. Lett.,* vol. 4, pp. 4213-4216, 2013/12/19 2013.

[11] W.-J. Yin, T. Shi, and Y. Yan, "Unusual defect physics in $CH_3NH_3PbI_3$ perovskite solar cell absorber," *Appl. Phys. Lett.,* vol. 104, p. 063903, 2014.

[12] J. Kang and L.-W. Wang, "High Defect Tolerance in Lead Halide Perovskite $CsPbBr_3$," *J. Phys. Chem. Lett.,* vol. 8, pp. 489-493, 2017/01/19 2017.

[13] Z. Xiao, W. Meng, J. Wang, and Y. Yan, "Thermodynamic Stability and Defect Chemistry of Bismuth-Based Lead-Free Double Perovskites," *ChemSusChem,* vol. 9, pp. 2628-2633, 2016.

[14] T. Umebayashi, K. Asai, T. Kondo, and A. Nakao, "Electronic structures of lead iodide based low-dimensional crystals," *Phys. Rev. B,* vol. 67, p. 155405, 04/15/ 2003.

[15] E. M. Miller, Y. Zhao, C. C. Mercado, S. K. Saha, J. M. Luther, K. Zhu, *et al.*, "Substrate-controlled band positions in $CH_3NH_3PbI_3$ perovskite films," *PCCP,* vol. 16, pp. 22122-22130, 2014.

[16] W. Ming, H. Shi, and M.-H. Du, "Large dielectric constant, high acceptor density, and deep electron traps in perovskite solar cell material CsGeI3," *J. Mater. Chem. A,* vol. 4, pp. 13852-13858, 2016.

[17] H. Shi and M.-H. Du, "Shallow halogen vacancies in halide optoelectronic materials," *Phys. Rev. B,* vol. 90, p. 174103, 11/05/ 2014.

[18] R. E. Brandt, V. Stevanović, D. S. Ginley, and T. Buonassisi, "Identifying defect-tolerant semiconductors with high minority-carrier lifetimes: beyond hybrid lead halide perovskites," *MRS Communications,* vol. 5, pp. 265-275, 2015.

Chapter 6*

Silver Bismuth Iodide: Crystal Structure, Morphology, and Photovoltaic Performance

In this chapter, a novel bismuth-based ternary halide system – silver bismuth iodides are explored for photovoltaic applications. Like $Cs_3Bi_2I_9$, thin-films of silver bismuth iodides exhibited facile solution processability, reasonable absorption coefficient, and atmospheric stability. Most notably, the mesoscopic solar cells with silver bismuth iodide as an absorber layer exhibited excellent power conversion efficiency as a lead-free solar cell material. In step further, with careful optimization of thin-film morphology, we achieved a power conversion efficiency of above 2.5% while fabricating the solar cells in ambient atmosphere.

---

*This section published substantially as Biplab Ghosh, Bo Wu, Guo Xintong, Padinhare C. Harikesh, Rohit Abraham John, Tom Baikie, Arramel, Andrew T. S. Wee, Claude Guet, Tze Chien Sum, Subodh Mhaisalkar, and Nripan Mathews. Superior performance of Silver Bismuth Iodide photovoltaics fabricated via dynamic hot-casting method under ambient conditions. *Advanced Energy Materials* (2019) 8, 1802051. DOI:10.1002/aenm.201802051

6.1 Introduction

At first glance, bismuth-based iodide perovskites looked promising due to easy solution processability and the high absorption coefficient coupled with long excited-state carrier lifetime. However, as were demonstrated in the previous chapters, the charge extraction from the perovskite solar cells is severely hindered by the molecular nature of the crystal structure, in which the $[Bi_2I_9]^{3-}$ bioctahedra are isolated by the *A*-site cations which does not take part in the bonding. Replacement of the *A*-site protonated cations with transition metal cations such as Ag or Cu results in a fascinating group of compounds called iodobismuthates. Apart from $[BiI_6]^{3-}$ octahedra formed due to Bi-I bonding, the transition metal cations also take part in bonding with iodine, resulting in another octahedron of $[M'X_6]$, where *M'* is the transition metal cation and offer a three-dimensional network of iodobismuthate unit.

Herein, we explored two phases of silver bismuth iodide (Ag_xBiI_{3+x}) with the nominal compositions of $AgBiI_4$ (x = 1) and Ag_2BiI_5 (x = 2) for photovoltaic applications in mesoscopic solar cell configurations. The optoelectronic investigations on Ag_xBiI_{3+x} thin-films showed a smaller lifetime of the excited-state charge carriers as compared to that of $Cs_3Bi_2I_9$ thin-films. However, the solar cells exhibited more than 1% power conversion efficiency, thus supporting our hypothesis of poor performance in $Cs_3Bi_2I_9$ due to the zero-dimensional structure. Moreover, Ag_xBiI_{3+x}-based solar cells can be fabricated in the ambient atmosphere, thus eliminating the need to stringent atmospheric control as required for Pb-based iodide perovskites. However, poor morphology and void formation during thin-film fabrication route appear to be a limiting factor in achieving high-efficiency solar cells. In this case, we developed a modified fabrication route by controlling the crystallization and grain growth to prepare high-quality Ag_xBiI_{3+x} thin-films. The resultant large grain thin-films exhibited full coverage on the mesoporous TiO_2 surface and hence, enhanced photovoltaic performances.

6.2 Crystal Structure of Silver Bismuth Iodide

Silver bismuth iodides, most notably amongst bismuthate family, were investigated earlier as a potential silver ion conductor, albeit their ionic conductivity was found to be poor [1]. However, their semiconducting bandgap opened new directions in optoelectronic applications. Interestingly, the nominal compositions of silver bismuth iodide phases always remained controversial in the literature, partly due to partial occupancies of Ag and Bi atoms and due high miscibility in solid solutions of the competing phases. In general, the solid solution of AgI and BiI_3 can be represented by the general formula of $M'_aM_bX_{a+3b}$ where *M'* and *M* denotes +1 cation and +3 cation respectively (the number represents the nominal charges), and X is the halide atom. Both *M* and *M'* sites are surrounded by six halide atoms in an octahedral configuration in a close-pack crystal structure, exhibiting a coordination number of 6 (Figure 6.1). In comparison, the alkali cation (*A*) has a coordination number of 12, and *M*-site shows a coordination number of 8 in the perovskite structure (either in AMX_3 of defect-assisted $A_3M_2X_9$). Moreover, crystal structures of $M'_aM_bX_{a+3b}$ can be described by the ordered layers of alternating [$M'X_6$] and [MX_6], rather than corner sharing octahedral network of perovskites (Figure 6.1(b) and (c)).

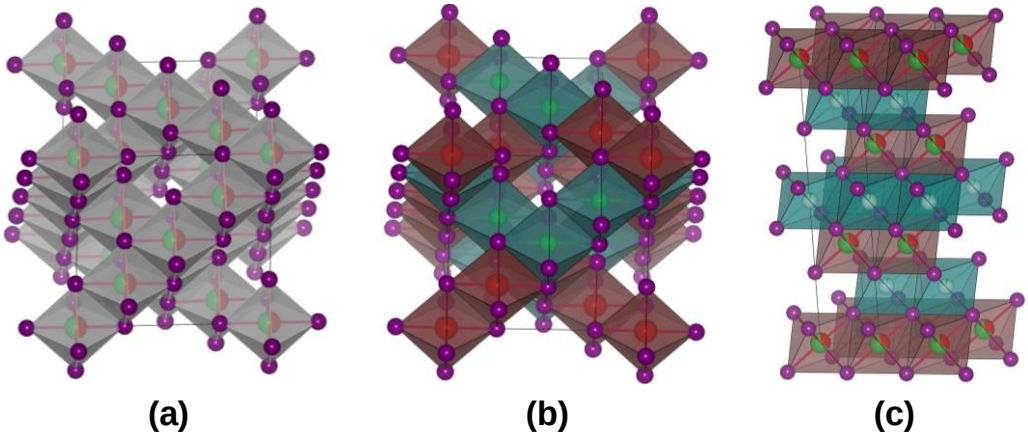

Figure 6.1: Schematic illustration of Ag_xBiI_{3+x} crystal structure. (a) $AgBiI_4$ crystal structure showing partial occupancies of Ag and Bi atoms. (b) Ordered $AgBiI_4$ crystal structure with alternating Ag and Bi atoms, (c) $R\bar{3}m$ crystal structure of Ag_2BiI_5 showing partial occupancies of Ag and Bi atoms in alternating lattice planes. (the red color represents Bi, green represents Ag and purple represents I atoms, the partial white atoms in Ag_2BiI_5 represents partial vacancy).

In silver bismuth iodides system, depending upon the ratio of Ag-to-Bi, several different stoichiometric compositions can be derived; however, the exact stoichiometric composition is often eluded. Four different phases of Ag-Bi-I ternary system have been reported so far, with nominal formulas of $AgBiI_4$, Ag_3BiI_6, Ag_2BiI_5, and $AgBi_2I_7$, yet there can be numerous possible combinations [1-3]. Of these, $AgBi_2I_7$ was found to be energetically unfavorable by DFT calculations in an earlier work [4]. The apparent phase with nominal composition $AgBi_2I_7$ was concluded to be an Ag-deficient $AgBiI_4$, otherwise it would lead to an unphysically short Bi-I bond length. On the other hand, both Ag_3BiI_6 and Ag_2BiI_5 possess a trigonal crystal structure ($R\bar{3}m$) with similar lattice constants [1]. The Ag_3BiI_6 phase was found to stable at high temperature (above 500 °C), although a metastable phase of similar composition can be observed by solid-state reaction according to the authors [5]. Recent work by Jung, *et al.* [6] suggested that only Ag_2BiI_5 can be formed

by solid-state reaction and is independent of precursor compositions [6]. Here we explore only $AgBiI_4$ and Ag_2BiI_5 phases of the silver bismuthate system which are the most stable phases under normal processing conditions for possible PV applications.

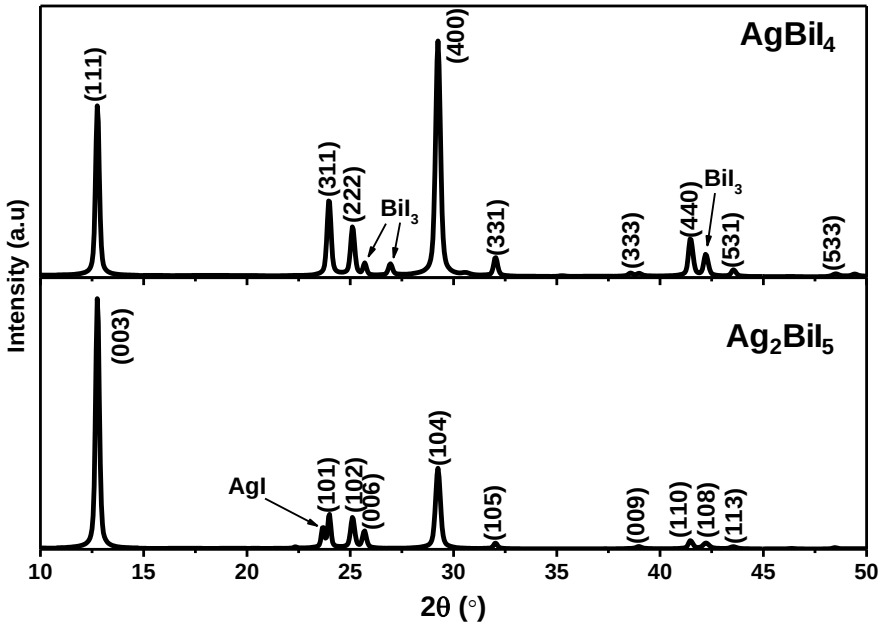

Figure 6.2: Thin-film XRD patterns of (a) $AgBiI_4$ and (b) Ag_2BiI_5. The patterns were indexed with simulated pattern from crystal structures reported previously. The thin-films were deposited onto glass substrate and annealed at 160 ℃. The major impurity phase in $AgBiI_4$ is BiI_3, and AgI in Ag_2BiI_5 which are indicated on the graph.

Figure 6.2 illustrates the XRD patterns of the silver bismuth iodide thin-films with the nominal compositions of $AgBiI_4$ and Ag_2BiI_5. The films were fabricated by dissolving required molar fraction of AgI and BiI_3 in DMSO: DMF mixture (4:1 v/v), followed by spin coating and annealing at 160 ℃. It should be noted here that all the fabrication processes were carried out in the ambient atmosphere. The XRD patterns of the respective phases were indexed

with the simulated pattern from the crystal structures published earlier. Bearing in mind that exact compositions of the phases are often presented in a partial fraction of atomic units due to partial occupancy, which would be difficult to achieve in solution processable technique. Hence, all the compositions mentioned in this chapter are nominal composition, derived from the initial composition of the precursor solutions. Presence of some impurity phases was noted in our observations (marked with BiI_3 and AgI in Figure 6.2), which can be assigned with either AgI, BiI_3 or Ag_2BiI_5 phase as the reflection positions are quite similar for Ag-deficient $AgBiI_4$, Ag_2BiI_5, and BiI_3. In addition, by varying Ag-to-Bi molar ratios, the XRD analysis of the spin-coated thin-films revealed reflections consistent with the impurity phases AgI and Ag_2BiI_5. Hence, our observations were also consistent with previous studies that Ag_3BiI_6 phase may not be stable in the conventional spin coating route. With increasing Ag-to-Bi molar ratio, the reflections from unreacted AgI became increasingly evident in the XRD patterns as illustrated in Figure 6.3.

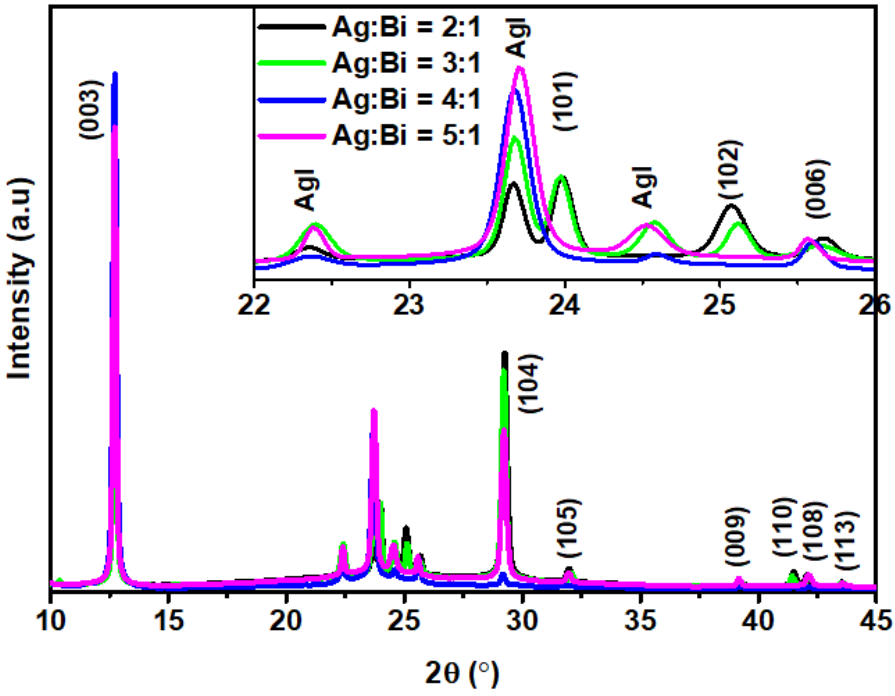

Figure 6.3: X-ray diffraction patterns of the thin-films fabricated from precursor solutions with different Ag-to-Bi ratio. The films were deposited onto glass substrate and annealed at 160 ℃. The patterns were indexed with Ag_2BiI_5 phase. The magnified version from 22 to 26 ° (2θ) is shown in the inset.

6.3 Optoelectronic Properties of Silver Bismuth Iodide

Figure 6.4(a) shows the optical absorption spectra of $AgBiI_4$ and Ag_2BiI_5 thin-films deposited on a flat glass slide. Both the phases showed an absorption onset around 700 nm, which is ~100 nm red-shift from Bi-based zero-dimensional perovskites. The absorption coefficient (~3×10^4 cm^{-1}) was found to be comparable with $Cs_3Bi_2I_9$. The band gaps extracted from Tauc plot (Figure 6.4(b)) relationship for the indirect bandgap relationship gave 1.66 eV and 1.7 eV for $AgBiI_4$ and Ag_2BiI_5 respectively, which are in good agreement with previous reports [3, 6, 7]. The absorption spectrum of Ag_2BiI_5 showed a distinct absorption peak around 3 eV, which may be due to excess AgI in the thin-films

as indicated by the XRD analysis (Figure 6.2(b)). Nevertheless, both the compounds did not show any observable photoluminescence under the room temperature measurement.

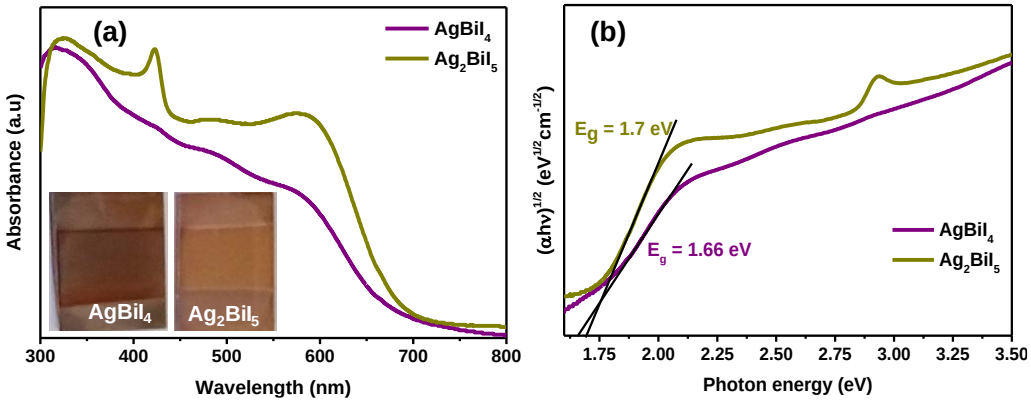

Figure 6.4: Optical properties of Ag_xBiI_{3+x}. (a) Optical absorption spectra of $AgBiI_4$ and Ag_2BiI_5 thin-films measured from 800 nm to 300 nm wavelength. (b) Tauc plot illustrating the estimation of indirect optical bandgap.

Since radiative processes are not prevalent in this system, the excited-states carrier kinetics were monitored through transient absorption (TA) spectroscopy. As shown in Figure 6.5(a), the kinetics of the excited state carriers are similar for both the phases, implying similar fate of the excited state carriers after photoexcitation. The TA spectra showed a strong photo-bleaching (PB) feature (i.e., negative ΔA) around 2.1 eV (~590 nm) and 2.05 eV (~605 nm) for $AgBiI_4$ and Ag_2BiI_5 respectively, followed by a photo-induced absorption (PIA) (i.e., positive ΔA) peak at longer wavelengths. Interestingly, the PB peak positions in both compounds do not correspond to their steady-state absorption edges; instead, they have the same position with the small hump near the absorption edges. This indicates the absorption edge of the two compounds comprise of an absorption continuum and an exciton absorption band which are not spectrally well resolved. The PB is then most likely due to the change of the excitonic

absorption resulting from the photoexcited carrier relaxation to the indirect band edge. Similar observations can also be found in Pb-based halide perovskites, where Elliot's theory has been quite useful in deconvoluting the contribution of the continuum and the excitonic absorption in the absorption spectra [8]. Using a similar framework, the absorption spectra of $AgBiI_4$ and Ag_2BiI_5 were modelled using Elliot's equation (the details can be found in the experimental section). A direct bandgap of 2.37 eV and 2.2 eV were found for $AgBiI_4$ and Ag_2BiI_5 respectively from the fitting of absorption spectra as illustrated in Figure 6.5(b). The direct exciton binding energies as estimated by the fittings are about 260 meV and 150 meV for $AgBiI_4$ and Ag_2BiI_5 respectively. However, these numbers are only approximate due to the broadness of the spectra lines that arise from system disorder. Nevertheless, the fitting results can perfectly explain the observed TA profiles by involving excitonic absorption. Carriers which relax to the indirect band edge can change the excited state exciton feature (oscillation strength, linewidth, and energy) through phase-space filling, carrier-exciton scattering, Stark effect, etc. Considering the negligible excited species at the direct exciton band in the presence of a lower-lying indirect bandgap, the observed decay dynamics at the PB is not due to the relaxation and recombination of excitons themselves, but instead due to the carriers at the indirect band edge. This is clearly seen in Figure 6.5(c), where the PB decay dynamics of both films shows long lifetimes up to tens of ns, which is much longer than the typical values of excitons. The decay dynamics were fitted using the bi-exponential decay formula:

$$I(t) = A_2 \ \exp\left(-t/\tau_1\right) + A_2 \exp\left(-t/\tau_2\right) \qquad (1)$$

where τ_1 and τ_2 are the short and long recombination lifetimes. Non single-exponential decay is commonly seen in many perovskite polycrystalline films, and usually arose from distributions of crystal size or trap states, non-radiative/radiative recombination and surface/bulk recombination difference, etc. [9-12] A fast component of $\tau_1 \approx 7$ ns and $\tau_1 \approx 11$ ns along with the slower

components of $\tau_2 \approx 29$ ns and $\tau_2 \approx 74$ ns were observed for $AgBiI_4$ and Ag_2BiI_5 thin-films. Interestingly, the lifetime values are much faster as compared to the results obtained with $Cs_3Bi_2I_9$ and as well with the reported values of $MAPbI_3$. This faster decay times in Ag_xBiI_{3+x} system may be strongly limited by the surface recombination, structural defects, intrinsic impurities or competing phases. These findings also indicate that defect tolerant nature in Ag_xBiI_{3+x}-system most probably absent, thus limiting the high-performance solar cell applications.

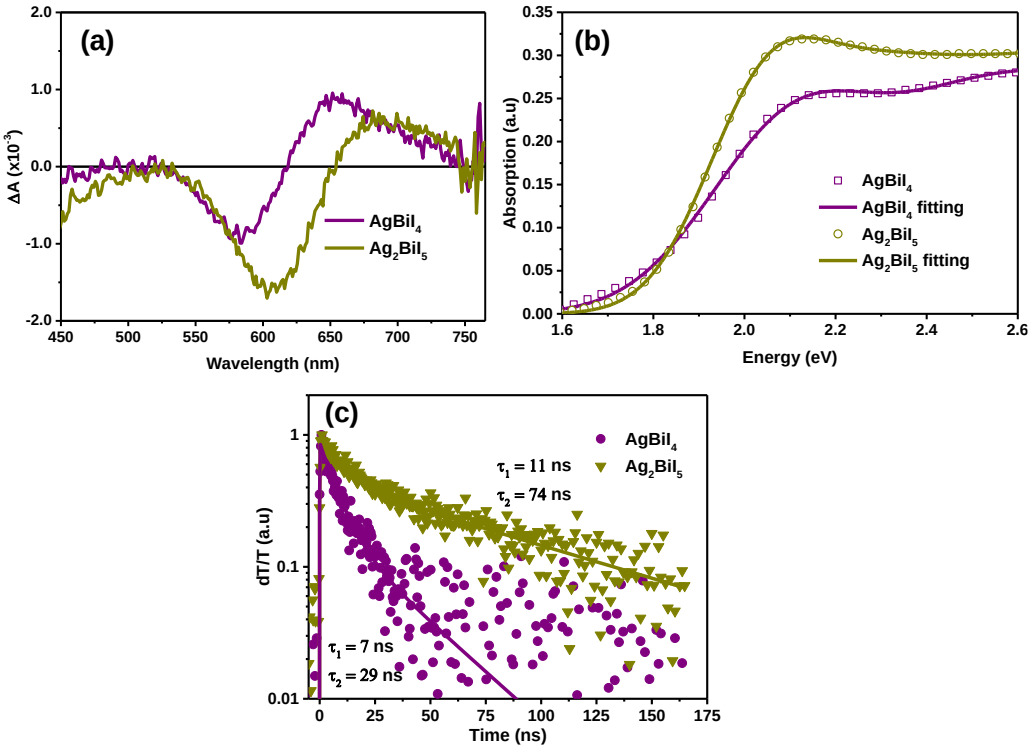

Figure 6.5: Optoelectronic characterizations of Ag_xBiI_{3+x} thin-films. (a) Transient absorption spectra, (b) absorption spectra fitted with Elliot's theory, (c) decay dynamics of the photobleached (PB) peak as shown in (a).

6.4 Transport Properties

As the excited state carrier lifetimes are moderate, a reasonable value of the carrier mobility can improve the product of $\mu\tau$ that controls the efficiency of charge extraction in PV applications. A four-point AC Hall measurement system was employed to estimate the carrier density and the mobility of silver bismuth iodide thin-films. Both $AgBiI_4$ and Ag_2BiI_5 thin films displayed moderate carrier densities (4.21×10^{14} cm^{-3} and 3.91×10^{14} cm^{-3} respectively) and good carrier mobilities (1.74 ± 0.3 cm^2 $V^{-1}s^{-1}$ and 2.26 ± 0.3 cm^2 $V^{-1}s^{-1}$ respectively) with a p-type character. Although the mobilities are smaller than $MAPbI_3$, they are comparable with other high-performing thin-films PV semiconductors such as CIGS or CZTSSe measured using similar techniques and much higher as compared to our results with $Cs_3Bi_2I_9$ [10, 13].

6.5 Energetics of Silver Bismuth Iodide

To determine the energy levels of VBM and CBM, which are one of the key parameters in designing the PSCs, Ultraviolet Photoelectron Spectroscopy (UPS) measurement was employed. The valence band maximum (VBM) of Ag_2BiI_5 (-5.7 eV) was found to be about 0.15 eV deeper as compared to $AgBiI_4$. Using indirect optical bandgap values as estimated from Tauc plot, the conduction band minimum (CBM) was found to be -4.0 eV and -3.88 eV for $AgBiI_4$ and Ag_2BiI_5 respectively. Figure 6.6(b) shows the energy levels $AgBiI_4$ and Ag_2BiI_5 along with the several HTMs that are commonly employed with Pb-based halide solar cells.

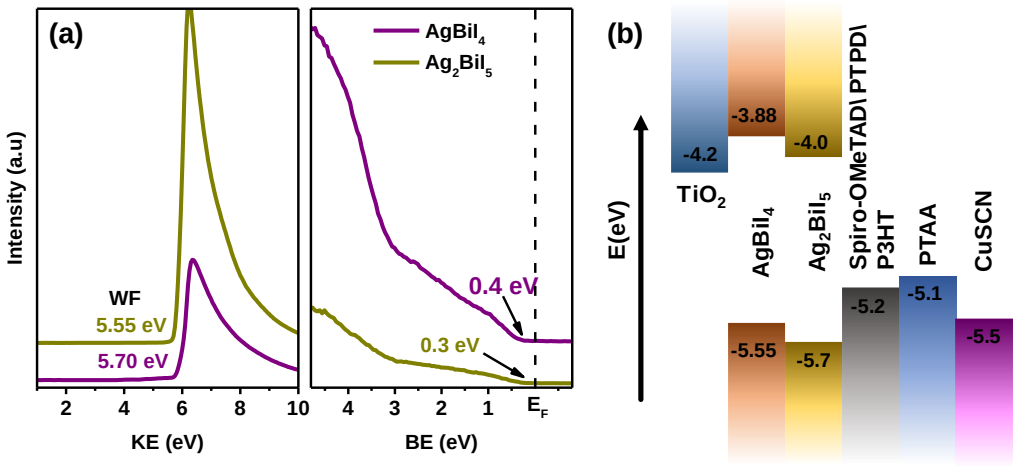

Figure 6.6: Energetics of Ag_xBiI_{3+x} system. (a) Ultraviolet Photoelectrons spectroscopy measurement of $AgBiI_4$ and Ag_2BiI_5 thin-films deposited on FTO coated glass substrate. The average film thickness was 500 nm. (b) Schematic diagram and energetics of Ag_xBiI_{3+x}-based solar cells employing different charge transport layers.

6.6 Silver Bismuth Iodide-based Solar Cell

To investigate the PV performance, we utilized the mesoscopic device architecture with TiO_2 as ETL. The optimizations of mesoporous layer thickness and screening of suitable HTM were carried out using $AgBiI_4$ as an absorber layer. The details of the solar cell fabrication process can be found in the experimental chapter. However, unlike $Cs_3Bi_2I_9$-based devices, the $AgBiI_4$-based solar cells were fabricated in the ambient atmosphere with a relative humidity of 60-75%. The solar cells were characterized at 10 mV s^{-1} scan rate under simulated AM1.5 illumination.

6.6.1 Effect of mp-TiO_2 Layer Thickness

The thickness of mesoporous TiO_2 (mp-TiO_2) layer was controlled by varying spin speed during spin coating of the mesoporous layer. For this investigation, mp-TiO_2 layer thicknesses of 330 nm, 300 nm, 250 nm, and 200 nm were used

along with Spiro-OMeTAD was used as HTM. The thicknesses of the other layers were kept identical for all the devices. The average photovoltaic parameters were provided in Table 6.1, and the statistical distribution is shown in Figure 6.7. From the data, it is evident that too thick or too thin mp-TiO_2 layer yielded poor results, and the highest performance was obtained with an mp-TiO_2 layer thickness of 250 nm. The *J-V* curves of the best devices are shown in Figure 6.8(a). The dependence of PV performance on the mp-TiO_2 layer thickness is likely to relate to the loading of the absorber layer and series resistance imparted by the mp-TiO_2 [14]. The initial improvement of PCE with decreasing mp-TiO_2 layer thickness is most likely due to a decrease in series resistance and efficient extraction. However, a very thin mp-TiO_2 (here 200 nm) also reduces the surface area for loading of absorber material, thus reducing J_{SC} and eventually PCE.

Table 6.1: PV parameters of $AgBiI_4$-based mesoscopic solar cells with different TiO_2 layer thickness

	V_{OC} (V)	J_{SC} (mA cm^{-2})	FF (%)	PCE (%)
330 nm	0.53 ± 0.02	1.48 ± 0.08	64.45 ± 5.44	0.50 ± 0.02
300 nm	0.56 ± 0.02	2.18 ± 0.15	67.13 ± 1.68	0.82 ± 0.06
250 nm	0.59 ± 0.03	2.61 ± 0.06	66.76 ± 1.72	1.02 ± 0.04
200 nm	0.56 ± 0.02	2.16 ± 0.06	67.30 ± 2.98	0.82 ± 0.03

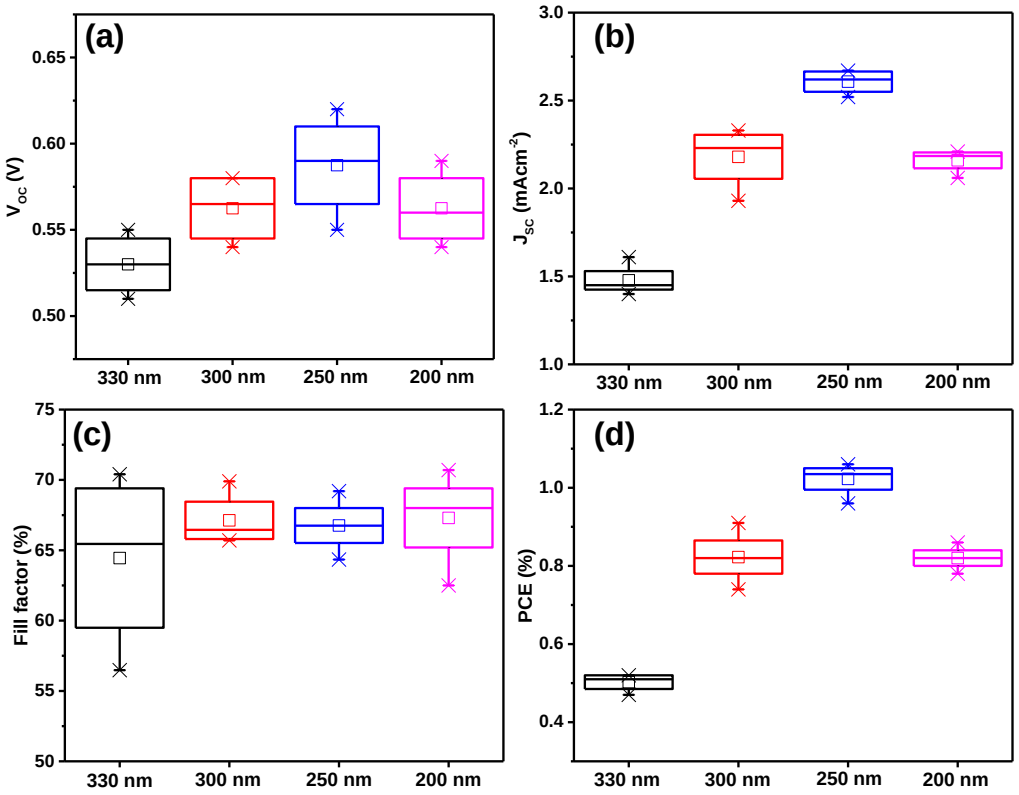

Figure 6.7: Statistical distributions of PV parameters of $AgBiI_4$-based solar cells. (a) open circuit voltage (V_{OC}), (b) short-circuit current density (J_{SC}), (c) fill factor, and (d) power conversion efficiency (PCE) as a function of mp-TiO_2 layer thickness. Data were derived from at least 4 separate devices.

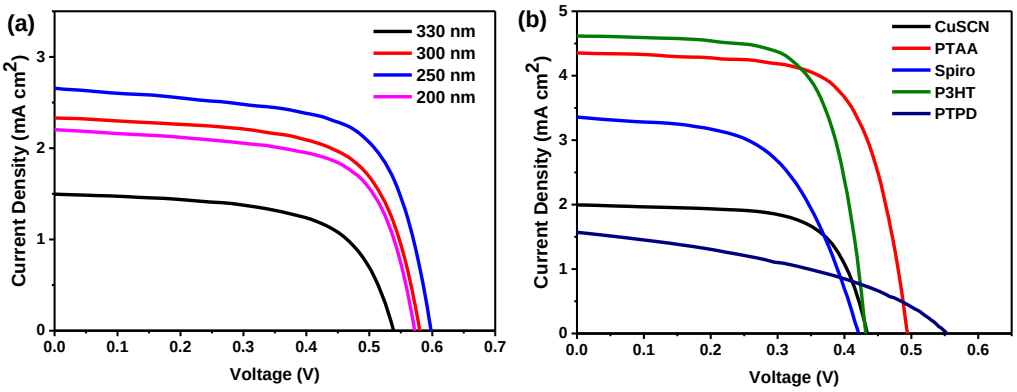

Figure 6.8: *J-V* characteristics of the best solar cell fabricated (a) with different mp-TiO_2 layer thickness with Spiro-OMeTAD as HTM, (b) employing different HTMs with TiO_2 as ETL.

6.6.2 Screening of HTMs for $AgBiI_4$-based Solar Cell

Over the years, various organic and inorganic HTMs are successfully utilized for Pb-based perovskite solar cells. Here, we chose four different organic HTMs (Spiro-OMeTAD, PTAA, P3HT, PTPD) and one inorganic HTM (CuSCN) to investigate the effect on $AgBiI_4$-based mesoscopic solar cells. The energetics of these HTMs are well-matched with $AgBiI_4$, thus expecting an efficient charge transfer at the interface (Figure 6.6). All the HTMs were deposited on top of $AgBiI_4$ layer by spin coating methods. The photovoltaic parameters of solar cells with different HTMs averaged from at least four devices are summarized in Table 6.2 and Figure 6.9. The *J-V* curves of the best solar cells are displayed in Figure 6.8(b). The maximum J_{SC} was obtained from the solar cells with PTAA as HTM. Coupled with reasonable V_{OC} and FF, the $AgBiI_4$-based solar cells exhibited the maximum PCE of 1.4%. Although similar PCE was also obtained with P3HT, the reproducibility was found to be poor. Interestingly, solar cells with PTPD as HTM, showed the maximum V_{OC} of 0.53 V amongst these HTMs, however, J_{SC} and FF were found to be poor, resulting in poor PCE.

Table 6.2: PV parameters of $AgBiI_4$-based mesoscopic solar cells with different HTM

	V_{OC} (V)	J_{SC} (mA cm^{-2})	FF (%)	PCE (%)
CuSCN	0.46 ± 0.02	1.72 ± 0.23	73.83 ± 1.13	0.58 ± 0.05
PTAA	0.48 ± 0.01	4.42 ± 0.07	67.10 ± 1.77	1.43 ± 0.04
Spiro-OMeTAD	0.40 ± 0.02	2.95 ± 0.51	55.83 ± 3.06	0.65 ± 0.10
P3HT	0.44 ± 0.01	3.92 ± 0.88	68.15 ± 3.00	1.18 ± 0.31
PTPD	0.53 ± 0.02	1.12 ± 0.35	34.08 ± 3.54	0.21 ± 0.09

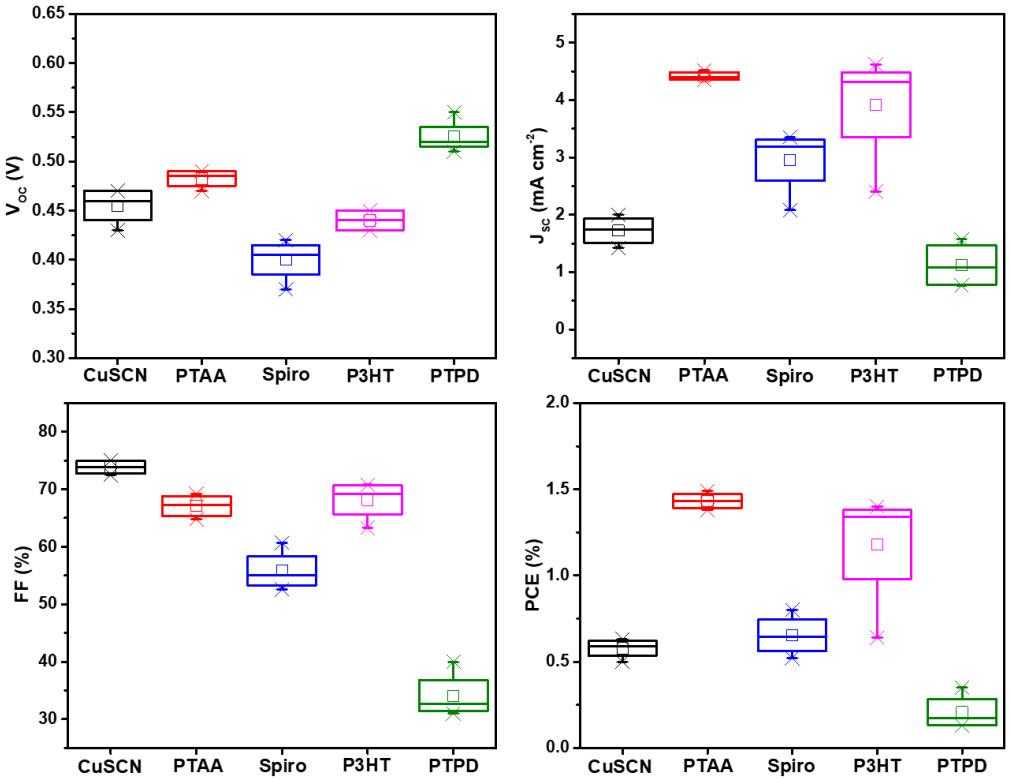

Figure 6.9: Statistical distribution of PV parameters of $AgBiI_4$-based solar cells employing different HTMs.

6.6.3 Performance Ag_xBiI_{3+x}-based Solar Cell

Based on previous screening results, we also fabricated Ag_2BiI_5-based mesoscopic solar cells. Figure 6.10(a) shows *J-V* curves of the best performing mesoscopic solar cells based on $AgBiI_4$ and Ag_2BiI_5 as an absorber layer with

250 nm thick mesoporous TiO_2 scaffold and PTAA as HTM. The corresponding incident photon to current conversion efficiency (IPCE) values are also shown in Figure 6.10(b). The integrated short-circuit density matches well with the solar cell J_{SC} for $AgBiI_4$-based solar cells, however, Ag_2BiI_5-based solar cells exhibited smaller J_{SC} as compared to the IPCE values. One of the possible reasons might be excess photo carrier generations which are discussed later.

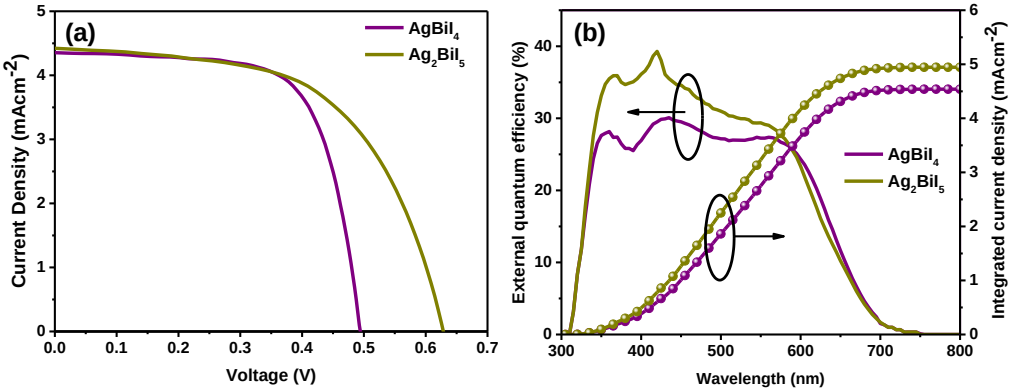

Figure 6.10: PV parameters of the best solar cells. (a) *J-V* curves of the $AgBiI_4$ and Ag_2BiI_5-based solar cells. (b) The corresponding IPCE plot of the solar cells presented in (a).

6.7 Crystallinity Engineering of Ag_xBiI_{3+x} Thin-films

The silver bismuth iodide-based mesoscopic solar cells already outperformed Bi-based iodide perovskites in terms of PCEs with high photocurrent density due to smaller bandgap and connected three-dimensional crystal structure as observed in the former. However, as illustrated in Figure 6.11(a, c), AgBiI thin-films exhibit poor surface coverage on the mesoporous TiO_2 layer which increases the recombination sites at the ETL-HTM interfaces, limiting further improvement of PCEs. Similar problems on Pb-based halide perovskite thin-films were overcome by an antisolvent treatment technique. Typically, a poor

solvent is dripped during spin coating of $MAPbI_3$ precursor solution, accomplishing faster nucleation of the intermediate phase on the substrate and subsequently controlled grain growth to achieve uniform morphology. However, the antisolvent treatment resulted in the void formation in the absorber layer as illustrated in the device cross-sectional SEM images (Figure 6.11(b, d)).

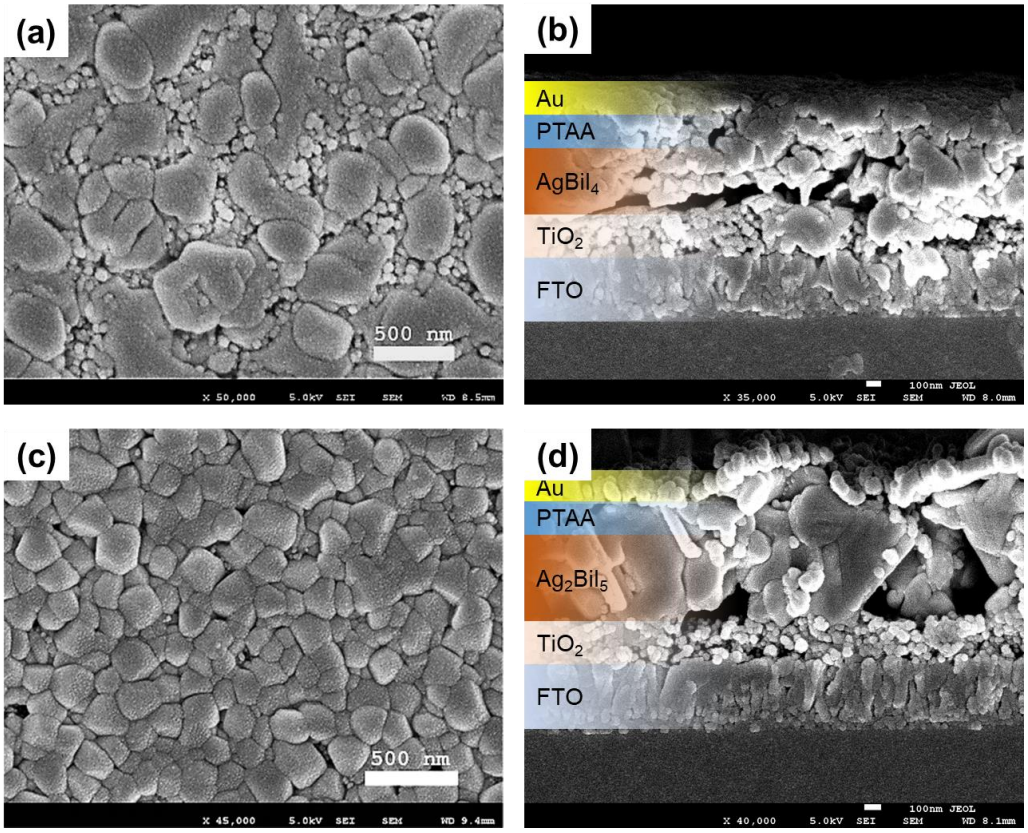

Figure 6.11: SEM images of $AgBiI_4$ (a, b) and Ag_2BiI_5 (c, d) thin-films fabricated by NSC, showing top morphology (a, c) and solar cell device cross-section (b, d).

Hence, to improve the surface morphology without having a negative impact on the absorber layer, we developed a modified spin coating technique in which the preheated precursor solution (at 100 °C) was drop-casted onto the preheated

substrates (at 100 ℃) during spinning. Later, the substrates were further annealed at 160 ℃ to complete the grain growth. We call this method as dynamic hot casting (DHC) technique. The resultant morphology of the thin-films was found to be compact, uniform and consists of micron-sized grains as shown in Figure 6.12.

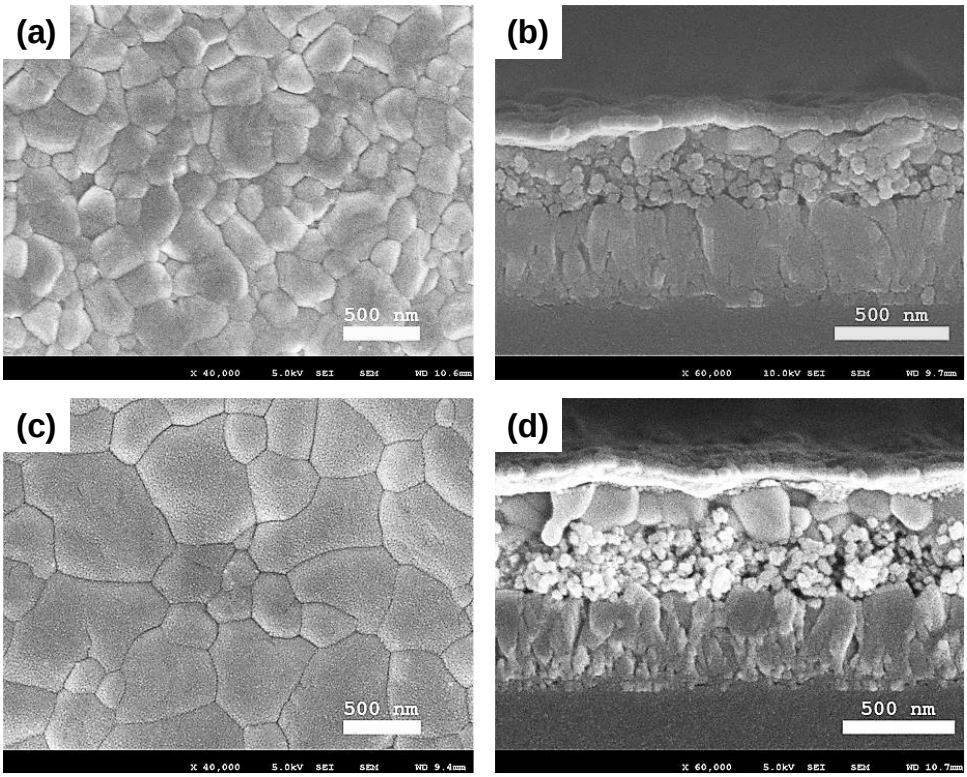

Figure 6.12: SEM images of $AgBiI_4$ (a, b) and Ag_2BiI_5 (c, d) thin-films fabricated by DHC, showing top morphology (a, c) and solar cell device cross-section (b, d). Scale bars 500 nm.

6.7.1 Photophysical Characterizations of Thin-films

The thin-films fabricated via DHC method were characterized by XRD, UV-Vis spectroscopy, and TAS for structural and optoelectronic properties. Figure 6.13(a) shows the XRD patterns of $AgBiI_4$ and Ag_2BiI_5 thin-films deposited on

mp-TiO_2 by NSC and DHC technique. As it is evident that there are no structural changes according to the XRD patterns. However, the absence of TiO_2 peak in DHC films confirms the complete coverage of $AgBiI_4$ on mp-TiO_2 which has a strong presence in the XRD patterns of NSC $AgBiI_4$ films. A similar conclusion can also be drawn from the XRD patterns of Ag_2BiI_5 thin-films on mp-TiO_2. Although there is still mp-TiO_2 peak in DHC Ag_2BiI_5 films, however, the intensity of that peak is reduced as compared to the XRD patterns of NSC Ag_2BiI_5 films. The no structural change can also be confirmed by absorption and TA spectra. There are no changes in optical bandgap according to UV-Vis spectroscopy (Figure 6.13(b)) as well as TA spectra show similar excited state carrier dynamics as we observed for NSC thin-films previously (Figure 6.13(c)). Nevertheless, the decay dynamics of the excited state carriers exhibited longer lifetime as compared to NSC thin-films for both $AgBiI_4$ and Ag_2BiI_5 phases. With DHC, a marked improvement in the slower component of the excited state carrier lifetime was observed with values of $\tau_2 \approx 75$ ns and 133 ns for $AgBiI_4$ and Ag_2BiI_5 thin-films respectively. Similar observations can be made from the optical absorption spectra of NSC and DHC thin-films. As shown in Figure 6.13(b), slope of the absorption edge of $AgBiI_4$/Ag_2BiI_5 thin-films fabricated via DHC method is steeper as compared to the thin-films fabricated via NSC technique, which is due to the reduction of structural disorder. Hence, the enhanced carrier lifetime and stronger absorption at the bandedge can be correlated with the improved grain size and passivation of trap states in the thin-films fabricated by the DHC technique.

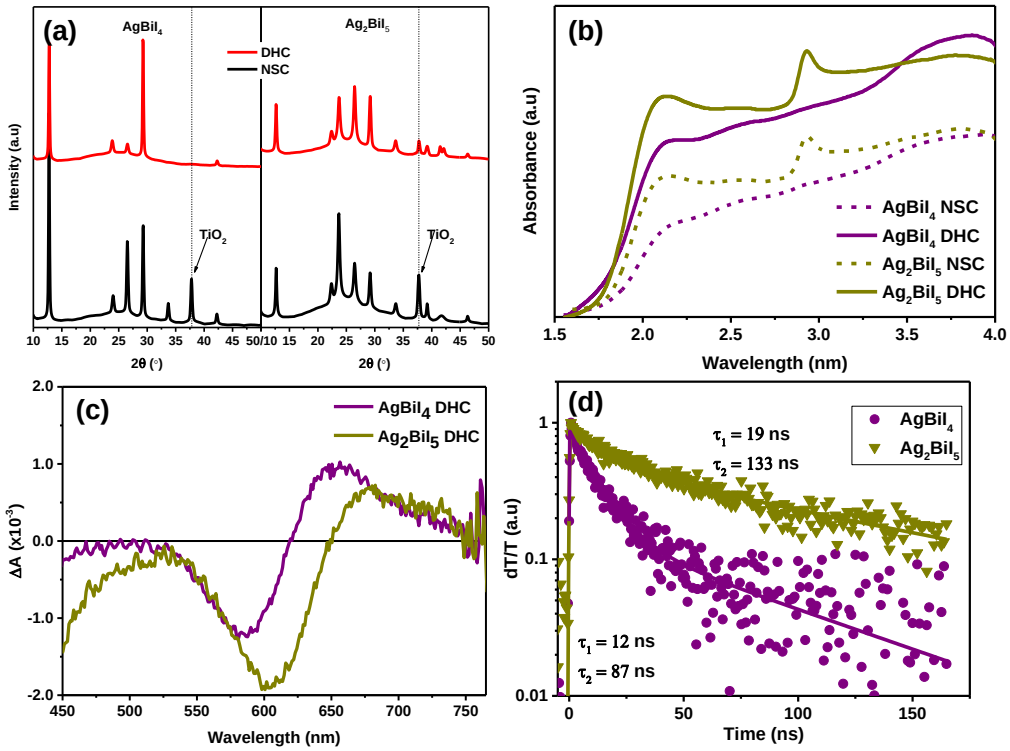

Figure 6.13: Structural and optoelectronic characterizations of Ag_xBiI_{3+x} system. (a) XRD patterns of $AgBiI_4$ and Ag_2BiI_5 thin-films deposited on mp-TiO_2 via NSC and DHC method (the mp-TiO_2 peak is illustrated). (b) Optical absorption spectra of $AgBiI_4$ and Ag_2BiI_5 thin-films deposited on flat glass substrate via NSC and DHC methods. The short dash lines and solid lines indicate the NSC and DHC method respectively. (c) The transient absorption spectra of $AgBiI_4$ and Ag_2BiI_5 thin-films deposited via NSC and DHC methods. (d) The decay dynamics of excited state carriers at the 595 nm and 605 nm for $AgBiI_4$ and Ag_2BiI_5 respectively. The films were deposited on quartz substrates

6.7.2 Possible Mechanism of DHC Technique

As evident from the structural, morphology and optoelectronic characterizations, the thin-films fabricated via DHC method exhibited better surface coverage and uniform morphology with large crystallite size as compared to the thin-films fabricated by NSC. A plausible explanation for this

observation is that the DHC method offers better control over local supersaturation of the precursor solution. In typical spin coating, the morphology and crystallite sizes of the thin-films depend on the nucleation and grain growth, which again depends on the level of precursor supersaturation [15]. Now, for Pb-based halide perovskites, the most common way to control the level of supersaturation is the use of antisolvents. In conventional antisolvent-assisted thin-film fabrication, the solubility of the precursor is high (high level of supersaturation necessary for nucleation) at the beginning of spin coating. During spinning, antisolvent is suddenly added on the film surface, which reduces the solubility of the precursor in the solvent (low level of supersaturation is sufficient for nucleation), resulting in rapid and uniform nucleation onset and therefore compact film morphology (Figure 6.14(top)). The use of antisolvents to control the supersaturation during spinning has been successfully demonstrated in fabricating lead-based halide perovskite thin-films devices with superior performances [16, 17]. However, a similar treatment on silver bismuth iodide resulted in voids and pinholes after thermal annealing (Figure 6.11(b, d)). We speculate that due to fast crystallization process during antisolvent treatment, some of the DMSO remain entrapped inside the thin films (due to the high boiling point of 189 ℃) [3]. Figure 14 schematically illustrates the crystallization process during NSC and DHC technique. During the post-annealing process, the excess solvent creates voids inside the thin-films and resulted in poor morphology. We also observed similar effects with conventional hot casting technique. On the other hand, in DHC, hot precursor solution was dripped slowly on the heated substrate during the spinning stage. We hypothesize that nucleation does not start at the initial contact with the mesoporous layer because of the high surface temperature. However, as the centrifugal force during spinning allowed the solvent to be removed simultaneously, it resulted in a supersaturated solution on top of the mesoporous TiO_2 layer. This resulted in a rapid nucleation onset with very little

solvent to be left for trapping. As the dripping process is continuous, it allowed to have layer-like precipitation on top of TiO_2, and subsequently grain growth takes place during the post-annealing process. Hence, unlike the commonly used antisolvent treatment in which the crystallization starts on the top of the films, the mesoporous TiO_2 surface acts as a nucleation site in DHC method, which resulted in uniform and compact thin-films.

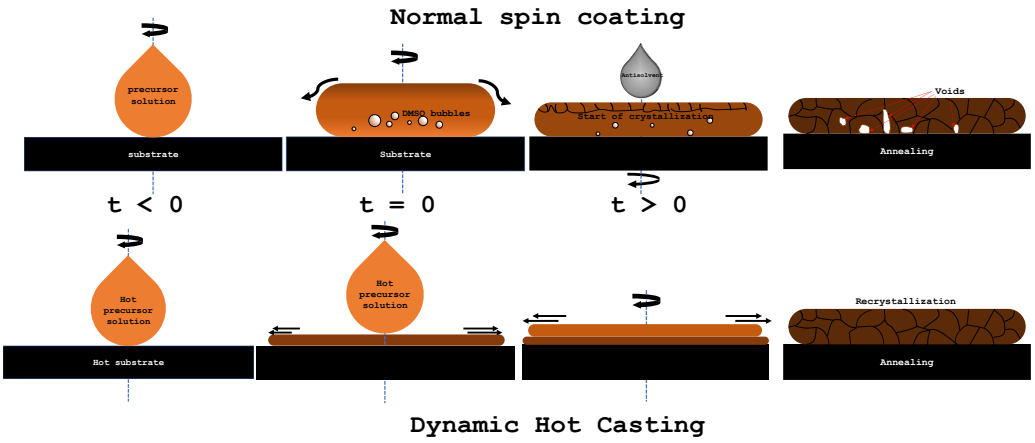

Figure 6.14: Schematic illustration of the proposed crystallization process in thin-films fabricated by normal spin coating (top) and dynamic hot casting (DHC) techniques (bottom).

6.7.3 Photovoltaic Performance of DHC Thin-films

To further illustrate the effect on photovoltaic performance, we fabricated silver bismuth iodide-based mesoporous solar cells with a device configuration of FTO/c-TiO_2/mp-TiO_2/absorber/PTAA/Au. The photovoltaic parameters are shown in Figure 6.15 and presented in Table 6.3. The most notable improvement in the PV parameters is the V_{OC} which is around 0.7 V now as compared to 0.5 V for the solar cells fabricated by NSC technique. The $AgBiI_4$-based solar cells reached a maximum PCE of 2.2% which is nearly 57% improvement over NSC treated solar cells. On the other hand, we achieved a

maximum efficiency of 2.84% with Ag_2BiI_5-based solar cell which is more than 77% improvement over NSC device. The champion devices yielded power conversion efficiencies of ~2.2% and 2.84% under 1 Sun illumination, which were the world record at the time of publication for solution processed $AgBiI_4$ and Ag_2BiI_5-based solar cells. The *J-V* curves of the champion devices are shown in Figure 6.16(a) under forward and reverse bias conditions which show negligible hysteresis. The significant improvement in the PCEs could be attributed to better surface coverage on mesoporous TiO_2 along with the reduction of trap states, resulting in improved excited-state carrier lifetime. Figure 6.16(b) illustrates the incident photon to current conversion efficiency (IPCE) over the spectral range of 300 to 750 nm for $AgBiI_4$ and Ag_2BiI_5-based solar cells fabricated by DHC. The IPCE spectra show good agreement with the absorption onset of the thin-films. However, the integrated current densities from IPCE spectra were calculated to be 6.6 mA cm^{-2} and 7.9 mA cm^{-2} as compared to 5.24 mA cm^{-2} and 5.95 mA cm^{-2}, calculated from *J-V* measurement by under illumination by simulated AM1.5 sun for $AgBiI_4$ and Ag_2BiI_5 respectively. This indicates better performance of the silver bismuth iodide based solar cells under low-intensity light (maximum PCE of 3.3% at 31.6 mW cm^{-2}). To understand the mismatch between IPCE and solar spectrum current densities, *J-V* measurements of Ag_2BiI_5-based solar cells were performed under varying light intensities, ranging from 10 mW cm^{-2} to 100 mW cm^{-2}. The *J-V* curves of Ag_2BiI_5-based solar cells at the different intensity of simulated light is shown in Figure 6.17(a). Figure 6.17(b) illustrates the dependence of J_{SC} and V_{OC} on the solar spectrum intensity. The current generation depicted a sublinear relationship with gradual saturation at higher intensities, indicating a lower charge collection efficiency at higher light intensity. This can be attributed to an imbalanced electron-hole mobility, or space-charge limited photocurrent due to the non-optimal thickness of electron/hole transport layers [18]. A semi-logarithmic plot of V_{OC} against light

intensity exhibited a slope of 1.5*kT/q*, indicating trap-assisted recombination near V_{OC}. This was also confirmed by variation of the FF at different light intensities. A maximum FF of 68.6% is achieved at 31.6 mW cm^{-2} light intensity, implying minimal charge carrier recombination at relatively lower light intensity due to low carrier generation [19].

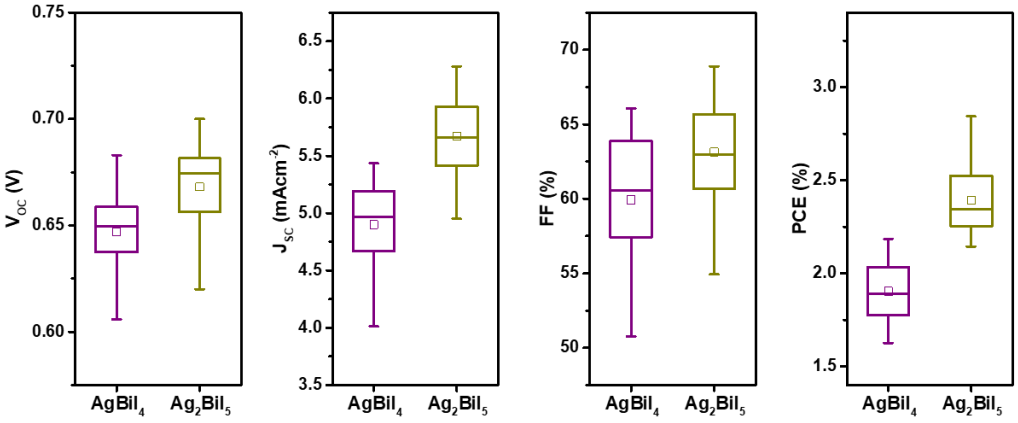

Figure 6.15: Statistical distribution of PV parameters of $AgBiI_4$ and Ag_2BiI_5-based mesoscopic solar cells fabricated via DHC method.

Table 6.3: PV parameters of Ag_xBiI_{3+x}-based mesoscopic solar cells fabricated via DHC technique

		V_{OC} (V)	J_{SC} (mA cm^{-2})	FF (%)	PCE (%)
$AgBiI_4$	Average	0.65 ± 0.02	4.90 ± 0.32	59.98 ± 4.40	1.90 ± 0.16
	Best	0.67	5.24	62.09	2.19
Ag_2BiI_5	Average	0.67 ± 0.02	5.67 ± 0.33	63.14 ± 3.37	2.39 ± 0.17
	Best	0.69	5.95	68.90	2.84

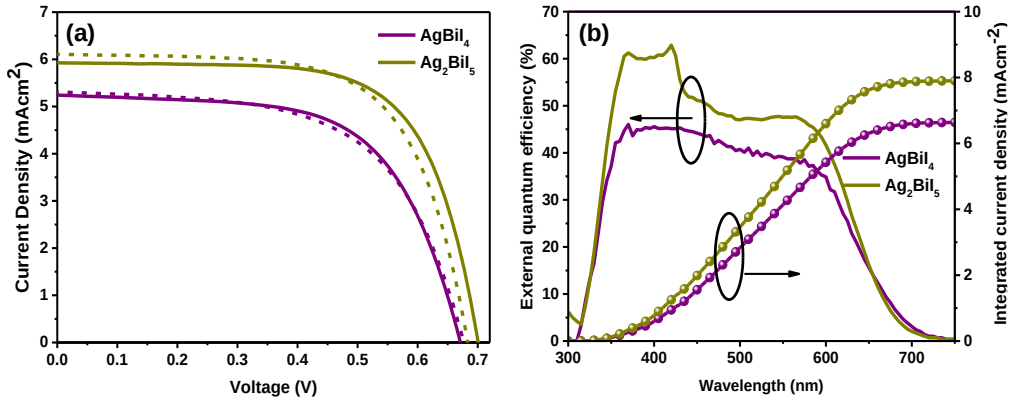

Figure 6.16: PV characterizations of $AgBiI_4$ and Ag_2BiI_5-based mesoscopic solar cells fabricated via DHC technique. (a) *J-V* characteristics of the solar cells measured under forward and reverse bias conditions. (b) IPCE of the same solar cells and the integrated short-circuit photocurrent density.

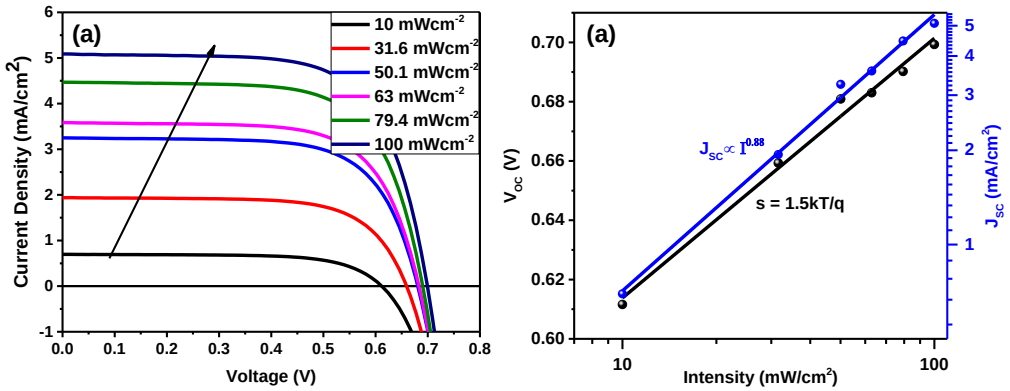

Figure 6.17: Ag_2BiI_5-based mesoscopic solar cells characterizations under different light intensity. (a) *J-V* characteristics of the solar cells under varying intensity of simulated light from 10 mW cm^{-2} to 100 mW cm^{-2}. (b) The variation of the V_{OC} and J_{SC} under different light intensity as obtained from the light intensity dependent *J-V* measurement.

6.8 Stability of Ag_2BiI_5-based Solar Cells

In addition to the PCE, the stability of the perovskite solar cells remained an important factor. Figure 6.18 shows the photostability of Ag_2BiI_5-based mesoscopic solar cells. At a constant reverse bias (0.6 V), the current density

was monitored under continuous light illumination. Our devices show no degradation in photocurrent over 200 s. We further investigated the stability of the solar cells in ambient atmosphere, and the PV parameters are shown in Figure 6.19. The devices were stored in the ambient atmosphere at ~22 ℃ and a relative humidity of 60-75% and remained stable over a month. The V_{OC} of the devices remained nearly the same within this period, but the efficiencies dropped slightly. The slow decrease in efficiency is mostly due to the decrease in current density which may be due to degradation at the HTM interface as the V_{OC} of the devices remain the same within this period.

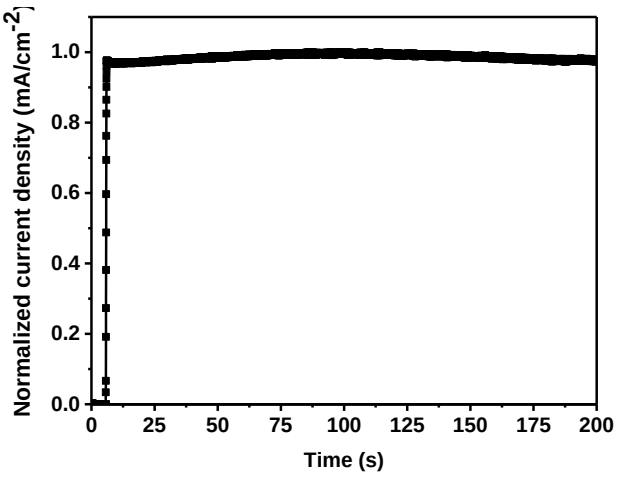

Figure 6.18: Stabilized current density (normalized) of Ag_2BiI_5-based solar cell at continuous illumination of AM1.5 G at a constant voltage bias of 0.6 V.

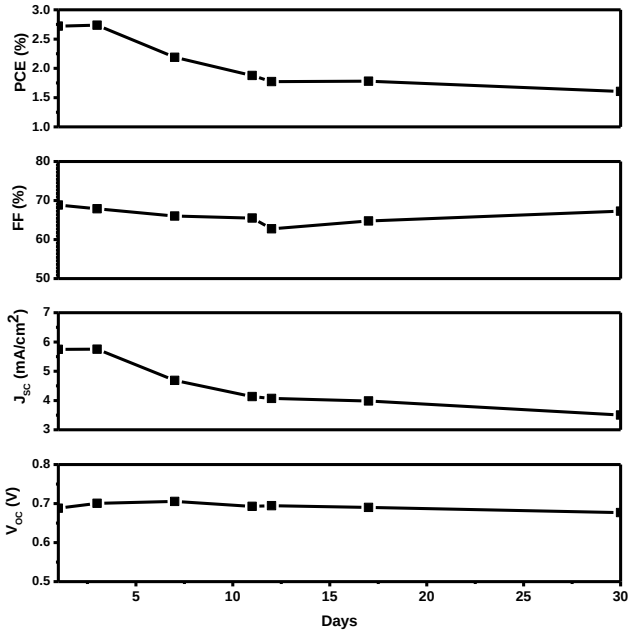

Figure 6.19: Photovoltaic parameters of Ag_2BiI_5-based mesoporous solar cells fabricated by DHC over a month (stored in ambient atmosphere under ≥65% RH at 22 °C).

6.9 Conclusions

In summary, we introduced a modified technique of spin coating for lead-free bismuth-based ternary halide solar cells. In this dynamic hot casting technique, the preheated precursor solutions were drop-cast onto preheated substrates during spinning in ambient atmosphere. With faster crystallization and rapid removal of precursor solution, micron-sized grains were observed; resulting in improved photovoltaic performance from silver bismuth iodide based mesoscopic solar cells. Interestingly, the solar cells performed better under lower intensity light that can further be explored for indoor applications. With further optimization in device fabrications, the power conversion efficiency can be improved.

References

[1] L. F. Mashadieva, Z. S. Aliev, A. V. Shevelkov, and M. B. Babanly, "Experimental investigation of the Ag–Bi–I ternary system and thermodynamic properties of the ternary phases," *J. Alloys Compd.*, vol. 551, pp. 512-520, 2013/02/25/ 2013.

[2] T. Oldag, T. Aussieker, H. Keller, C. Preitschaft, and A. Pfitzner, "Solvothermale Synthese Und Bestimmung Der Kristallstrukturen von $AgBiI_4$ Solvothermal Synthesis and Crystal Structure Determination of $AgBiI_4$.," *Z. Anorg. Allg. Chem*, vol. 631, pp. 677-682, 2005.

[3] T. Ivan, K. Said, I. Eisuke, U. Toshiyuki, Y. Koji, T. Hiroshi, *et al.*, "Photovoltaic Rudorffites: Lead-Free Silver Bismuth Halides Alternative to Hybrid Lead Halide Perovskites," *ChemSusChem*, vol. 10, pp. 3754-3759, 2017.

[4] Z. Xiao, W. Meng, D. B. Mitzi, and Y. Yan, "Crystal Structure of $AgBi_2I_7$ Thin Films," *J. Phys. Chem. Lett.*, vol. 7, pp. 3903-3907, 2016/10/06 2016.

[5] I. Turkevych, S. Kazaoui, E. Ito, T. Urano, K. Yamada, H. Tomiyasu, *et al.*, "Photovoltaic Rudorffites: Lead-Free Silver Bismuth Halides Alternative to Hybrid Lead Halide Perovskites," *ChemSusChem*, vol. 10, pp. 3754-3759, 2017.

[6] K. W. Jung, M. R. Sohn, H. M. Lee, I. S. Yang, S. D. Sung, J. Kim, *et al.*, "Silver bismuth iodides in various compositions as potential Pb-free light absorbers for hybrid solar cells," *Sustain. Energ. Fuels*, vol. 2, pp. 294-302, 2018.

[7] H. Zhu, M. Pan, M. B. Johansson, and E. M. J. Johansson, "High Photon-to-Current Conversion in Solar Cells Based on Light-Absorbing Silver Bismuth Iodide," *ChemSusChem*, vol. 10, pp. 2592-2596, 2017.

[8] M. Saba, F. Quochi, A. Mura, and G. Bongiovanni, "Excited State Properties of Hybrid Perovskites," *Acc. Chem. Res.*, vol. 49, pp. 166-173, 2016/01/19 2016.

[9] V. D'Innocenzo, A. R. Srimath Kandada, M. De Bastiani, M. Gandini, and A. Petrozza, "Tuning the Light Emission Properties by Band Gap Engineering in Hybrid Lead Halide Perovskite," *J. Am. Chem. Soc.*, vol. 136, pp. 17730-17733, 2014/12/24 2014.

[10] W. Adam, M. Rebecca, E. Giles, S. Henry, J. Michael, and H. Laura, "Band‐Tail Recombination in Hybrid Lead Iodide Perovskite," *Adv. Funct. Mater.*, vol. 27, p. 1700860, 2017.

[11] W. Bo, N. H. Tiep, K. Zhiliang, H. Guifang, G. David, M. Nripan, *et al.*, "Discerning the Surface and Bulk Recombination Kinetics of Organic–Inorganic Halide Perovskite Single Crystals," *Adv. Energy Mater.*, vol. 6, p. 1600551, 2016.

[12] S. J. Kim, J. Byun, T. Jeon, H. M. Jin, H. R. Hong, and S. O. Kim, "Perovskite Light-Emitting Diodes via Laser Crystallization: Systematic Investigation on Grain Size Effects for Device Performance," *ACS Appl. Mater. Interfaces*, vol. 10, pp. 2490-2495, 2018/01/24 2018.

[13] O. Gunawan, Y. Virgus, and K. F. Tai, "A parallel dipole line system," *Appl. Phys. Lett.*, vol. 106, p. 062407, 2015.

[14] H.-S. Kim, J.-W. Lee, N. Yantara, P. P. Boix, S. A. Kulkarni, S. Mhaisalkar, *et al.*, "High Efficiency Solid-State Sensitized Solar Cell-Based on Submicrometer Rutile TiO_2 Nanorod and $CH_3NH_3PbI_3$ Perovskite Sensitizer," *Nano Lett.*, vol. 13, pp. 2412-2417, 2013/06/12 2013.

[15] S. S. Shin, J. P. Correa Baena, R. C. Kurchin, A. Polizzotti, J. J. Yoo, S. Wieghold, *et al.*, "Solvent-Engineering Method to Deposit Compact Bismuth-Based Thin Films: Mechanism and Application to Photovoltaics," *Chem. Mater.*, vol. 30, pp. 336-343, 2018/01/23 2018.

[16] X. Manda, H. Fuzhi, H. Wenchao, D. Yasmina, Z. Ye, E. Joanne, *et al.*, "A Fast Deposition‐Crystallization Procedure for Highly Efficient Lead Iodide Perovskite Thin‐Film Solar Cells," *Angew. Chem. Int. Ed.*, vol. 53, pp. 9898-9903, 2014.

[17] N. J. Jeon, J. H. Noh, Y. C. Kim, W. S. Yang, S. Ryu, and S. I. Seok, "Solvent engineering for high-performance inorganic–organic hybrid perovskite solar cells," *Nat. Mater.*, vol. 13, p. 897, 07/06/online 2014.

[18] V. D. Mihailetchi, J. Wildeman, and P. W. M. Blom, "Space-Charge Limited Photocurrent," *Phys. Rev. Lett.*, vol. 94, p. 126602, 04/01/ 2005.

[19] D. Zhao, W. Ke, C. R. Grice, A. J. Cimaroli, X. Tan, M. Yang, *et al.*, "Annealing-free efficient vacuum-deposited planar perovskite solar cells with evaporated fullerenes as electron-selective layers," *Nano Energy*, vol. 19, pp. 88-97, 2016/01/01/ 2016.

Chapter 7

Concluding Remarks and Future Outlook

This chapter threads together all the results obtained in this study and puts them in the perspective of the current state of lead-free PV research. The results obtained are compared with the objectives initially laid out for this work and are evaluated in terms of the novel contributions. The limitations of the work are also highlighted, targeted to aid in streamlining future direction towards more efficient lead-free solar cells and a framework for the screening of lead-free perovskites for PV applications.

7.1 Conclusions

Solution-processed lead halide perovskites established themselves as the most important absorber material for PV, and are recognized as one of the biggest scientific breakthroughs of the year 2013 by *Science* [1-4]. Unfortunately, the over-reliance on highly toxic Pb^{2+} and long-term instability remain key issues for widespread commercial applications. The significant concentration of Pb^{2+} in highly-efficient halide perovskites and their water solubility make it extremely hazardous compound [5]. Another apparent issue is the inherent instability of lead-based halide perovskites in the ambient atmosphere [6]. Although the stability of Pb-based halide perovskites has been improved impressively in recent times along with the simultaneous development of passivation techniques, PSCs still do not match with current commercial benchmark. In addition, the fabrication of lead-based halide perovskites also requires stringent environmental control, further impinging their large-scale production [7-10]. To address these potential issues, the present project is conducted to explore the possible replacement of lead by non-toxic bismuth in perovskite structure. Throughout the present project, several conclusions are detailed below:

Bismuth-based ternary halides are well-known in coordination chemistry due to their rich structural diversity with varied building blocks of inorganic motifs. For PV applications, we followed the concept of $MAPbI_3$, in which the respective halide salts are dissolved together for perovskite synthesis. In addition to near-zero toxicity, good atmospheric stability, and solution processability, bismuth halide perovskites were expected to exhibit similar optoelectronic properties like $MAPbI_3$ due to similarities in bonding environment. In this essence, replacing lead with bismuth deemed to be a favorable option for fabricating lead-free perovskite solar cells. Our investigations showed that Bi-based iodide perovskites crystallize into low-

dimensional structure with the chemical formula of $A_3Bi_2I_9$ (*A* = Cs, MA, FA), which exhibited excellent absorption in the visible wavelength range. With a bandgap of 2 eV, these compounds could be easily used in tandem solar cell configurations. However, the photovoltaic performance of $Cs_3Bi_2I_9$-based mesoscopic solar cells was found to be poor as compared to Pb-based halide perovskites. Although transient absorption spectroscopy studies revealed the presence of long-lived excited-state carriers, the radiative recombination in $Cs_3Bi_2I_9$ was short-lived and limited by intrinsic defects. This contrastive phenomenon was further clarified by first principle calculations based on DFT.

To complement our experimental results, we embarked on theoretical investigations to highlights the limits and strategies to improve PV performance. Based on DFT calculations, the bandgap was confirmed to be indirect in nature along with the presence of heavy carriers. This definitely limits the PV performance of $Cs_3Bi_2I_9$ in thin-film solar cells. Further investigations on the defect properties unravel the presence of intrinsic defects that act as non-radiative recombination centers. It should be mentioned here that our selection strategy was partially based on defect tolerant semiconductor like $MAPbI_3$. Although the electronic structure of $Cs_3Bi_2I_9$ in the photoactive region is quite similar to $MAPbI_3$, the defect properties appear to be very different. The most plausible reason for the different defect chemistry would be the low-dimensional crystal structure of Bi-based iodide perovskites. Nevertheless, taking a cue from DFT results, we demonstrated that the PV performance of $Cs_3Bi_2I_9$-based mesoscopic solar cells can be improved by mitigating specific defects.

The primary role of A-site cations in perovskite structure is to donate an electron to the inorganic octahedral network and stabilize the perovskite crystal structure. For Bi-based iodide perovskites, the *A*-site cations also act as a spacer between $[Bi_2I_9]^{3-}$ bioctahedra. This leads to a zero-dimensional crystal structure,

in which the excited-state carriers localized, making the charge extraction extremely difficult as was evident from our study. Despite the poor power conversion efficiencies achieved, our study revealed that low-dimensional crystal structure of Bi-based halide perovskites remains a major bottleneck in achieving highly efficient solar cells. Considering the interesting electronic configurations of bismuth, as it offers strong relativistic effects and ns^2 electrons, we concluded that higher dimensional analogues of Bi-based ternary halides would be more suitable for PV applications.

To induce a continuous network of crystal structure, we introduce Ag^+ in place of protonated cations, which resulted in silver bismuth iodide (Ag_xBiI_{3+x}) system. The resultant PV performance was also promising, reaching a PCE value of ~3% in mesoscopic solar cell architecture. This opens a new avenue for lead-free thin-film solar cells as perovskite-inspired materials. Apart from solution processable route, the fabrication of Ag_xBiI_{3+x}-based solar cells were performed in ambient atmosphere, which is a massive advantage over Pb-based halide perovskites. Since silver bismuth iodide system does not offer the defect tolerant properties as evident from photoluminescence spectroscopy, the high photocurrent as observed in mesoscopic solar cells is most probably due to efficient extraction due to charge delocalization. Further improvement in PCE is expected by passivating the defects during solar cell fabrications.

7.2 Future Perspectives

7.2.1 Design and Discovery of Lead-free Perovskites via Machine Learning

An Edisonian experimental search for lead-free perovskites via trial-and-error approaches is unpractical considering the time, resources and uncertainties in laboratory conditions. An inverse design approach (applied in this work on a small scale) would be more suitable to rapidly screen the unknown class of

materials for photovoltaic applications. High throughput calculations based on DFT have already been utilized to predict and screen the potential non-toxic candidate for perovskite solar cell applications. However, the materials space remained limited considering the complex nature of the crystal structures and machine-time required for accurate calculations. In this context, materials discovery via machine-learning (ML) methods is likely to be in forefront due to their easy implementations, wider context, learning ability, and cost-effective approach. Traditionally, materials properties targeting specific application, are the input for ML tools, which generates a complex function to predict novel materials. Recently, ML has been used for predicting and designing novel oxide perovskites from the various simulated and experimental database [11-17]. In a similar approach, ML tools can be effectively utilized in predicting unknown class of perovskites suitable for PV applications. However, the biggest challenge remains is the feature set to describe the materials accurately. A proper study on the structure that is most influential in determining the crystal properties is still lacking.

7.2.2 Combinatorial Synthesis of Perovskites

Although property-based inverse design remained fruitful in modern scientific investigations, a combinatorial approach would also be interesting to find alternatives of lead-based perovskite. In combinatorial synthesis, massive amount of diverse materials can be synthesized in parallel, coupled with different characterization techniques. Additionally, the exploration of different stoichiometric regime for a given composition can also be examined efficiently by combinatorial route. Recent work by Wong, *et al.* [18] demonstrated the application of the evaporation-based combinatorial approach to predict several Pd- and Sn-based halide perovskites for photovoltaics. Moreover, combinatorial synthesis can also be used as newer data set for ML tool, which is often limited by theoretical calculations.

7.2.3 Non-perovskite Crystal Structure

As was discussed in this thesis, the nature of bonding and crystal structure play the most important roles in defining the optoelectronic properties of halide perovskites. Being low-dimensional structure, Bi-based $A_3Bi_2I_9$ performed poorly, whereas Ag_xBiI_{3+x} showed promising PV performance although the latter does not form perovskite structure. The higher crystal symmetry and connected network might be the most plausible reason for reasonable PV performance from silver bismuth iodide system. In this context, perovskite-related phases such as antiperovskite or spinel would be an interesting class of materials for optoelectronic applications. In contrast to conventional perovskite structure, anion and cation roles are reversed in antiperovskite structure, which also exhibits connected octahedral network and tunable optoelectronic properties. Spinels, on the other hand, can be considered as an alternating octahedral and tetrahedral network with a chemical formula of AB_2X_4 (*A*, *B* are different size cations, *X* is anion). The complementary properties of tetrahedral (such as Si) and octahedral (such as $MAPbI_3$) coordination can lead to a viable route for an emerging photovoltaic absorber.

7.2.4 Alternative Synthesis Route

The systematic approach to select bismuth as a replacement of lead was based on the similarity in electronic structure at the photoactive region of these semiconductors. Our investigations showed that the screening criterion is logical, but not sufficient to warrant discovery of high-performance semiconductor for PV applications. However, it is too early to completely rule out the Bi-based zero-dimensional perovskites for optoelectronic applications. A recent work has shown that ultra-thin $Cs_3Bi_2I_9$ layer (~5 nm) exhibits remarkable photodetector properties and can be used as flexible memristor [19]. Further optimizations on the thin-film morphology and a better control over stoichiometry could see further improvement of PCE of these low-dimensional

perovskites.

In a broader context, compact and pin-hole free thin-film formation remained a significant challenge for lead-free absorber materials. An important area of focus would be controlling defects, which have a significant impact on device functionality. Majority of synthesis procedures are based on Pb-based halide perovskites system, which may not be suitable for lead-free compounds. Complex fabrication methods (antisolvent treatment, solvent annealing, controlling the partial pressure of the precursor) further complicate the fabrication routes for lead-free compounds. For example, many of the predicted lead-free compounds are found to be challenging to synthesize via solution processable route due to their poor solubility in organic solvents. High-vacuum thermal evaporation route, which offers better control over stoichiometry, can be a viable option for fabricating lead-free solar cells. Mitzi and co-workers [20] recently utilized thermal evaporation route to deposited thin-films of InI, which is nearly insoluble in most of the organic solvents. The ability to grow high electronic quality crystals and thin-films will be the basis to achieve further improvements in the efficiency of lead-free perovskite-based optoelectronic devices.

References

[1] N. Aristidou, C. Eames, I. Sanchez-Molina, X. Bu, J. Kosco, M. S. Islam, *et al.*, "Fast oxygen diffusion and iodide defects mediate oxygen-induced degradation of perovskite solar cells," *Nat. Commun.*, vol. 8, p. 15218, 05/11/online 2017.

[2] A. J. Lehner, D. H. Fabini, H. A. Evans, C.-A. Hébert, S. R. Smock, J. Hu, *et al.*, "Crystal and Electronic Structures of Complex Bismuth Iodides $A_3Bi_2I_9$ (A = K, Rb, Cs) Related to Perovskite: Aiding the Rational Design of Photovoltaics," *Chem. Mater.*, vol. 27, pp. 7137-7148, 2015/10/27 2015.

[3] Z. Hong, M. Jian, H. Hexiang, Z. Di, Z. H. L., X. Fengxian, *et al.*, "A Smooth $CH_3NH_3PbI_3$ Film via a New Approach for Forming the PbI2 Nanostructure Together with Strategically High CH_3NH_3I Concentration for High Efficient Planar-Heterojunction Solar Cells," *Adv. Energy Mater.*, vol. 5, p. 1501354, 2015.

[4] "Newcomer Juices Up the Race to Harness Sunlight," *Science*, vol. 342, pp. 1438-1439, 2013.

[5] A. Abate, "Perovskite Solar Cells Go Lead Free," *Joule*, vol. 1, pp. 659-664, 2017/12/20/ 2017.

[6] A. Ciccioli and A. Latini, "Thermodynamics and the Intrinsic Stability of Lead Halide Perovskites $CH_3NH_3PbX_3$," *J. Phys. Chem. Lett.*, 2018/06/14 2018.

[7] A. Mei, X. Li, L. Liu, Z. Ku, T. Liu, Y. Rong, *et al.*, "A hole-conductor–free, fully printable mesoscopic perovskite solar cell with high stability," *Science*, vol. 345, pp. 295-298, 2014.

[8] L. Tomas, E. G. E., N. N. K., H. S. N., P. Annamaria, and S. H. J., "Stability of Metal Halide Perovskite Solar Cells," *Adv. Energy Mater.*, vol. 5, p. 1500963, 2015.

[9] Z. Hong, C. Jiaqi, L. Dan, L. Francis, M. Jian, L. Chunjun, *et al.*, "Toward All Room-Temperature, Solution-Processed, High-Performance Planar Perovskite Solar Cells: A New Scheme of Pyridine-Promoted Perovskite Formation," *Adv. Mater.*, vol. 29, p. 1604695, 2017.

[10] H. Zhang, X. Ren, X. Chen, J. Mao, J. Cheng, Y. Zhao, *et al.*, "Improving the stability and performance of perovskite solar cells via off-the-shelf post-device ligand treatment," *Energy Environ. Sci.*, 2018.

[11] C. Li, X. Lu, W. Ding, L. Feng, Y. Gao, and Z. Guo, "Formability of ABX_3 (X = F, Cl, Br, I) halide perovskites," *Acta Crysrallogr. B*, vol. 64, pp. 702-707, 2008.

[12] H. Zhang, N. Li, K. Li, and D. Xue, "Structural stability and formability of ABO_3-type perovskite compounds," *Acta Crysrallogr. B*, vol. 63, pp. 812-818, 2007.

[13] G. Pilania, P. V. Balachandran, C. Kim, and T. Lookman, "Finding New Perovskite Halides via Machine Learning," *Frontiers in Materials*, vol. 3, 2016-April-26 2016.

[14] P. V. Balachandran, A. A. Emery, J. E. Gubernatis, T. Lookman, C. Wolverton, and A. Zunger, "Predictions of new ABO_3 perovskite compounds by combining machine learning and density functional theory," *Physical Review Materials*, vol. 2, p. 043802, 04/11/ 2018.

[15] W. Li, R. Jacobs, and D. Morgan, "Predicting the thermodynamic stability of perovskite oxides using machine learning models," *Computational Materials Science*, vol. 150, pp. 454-463, 2018/07/01/ 2018.

[16] P. Raccuglia, K. C. Elbert, P. D. F. Adler, C. Falk, M. B. Wenny, A. Mollo, *et al.*, "Machine-learning-assisted materials discovery using failed experiments," *Nature*, vol. 533, p. 73, 05/04/online 2016.

[17] G. Hautier, C. C. Fischer, A. Jain, T. Mueller, and G. Ceder, "Finding Nature's Missing Ternary Oxide Compounds Using Machine Learning and Density Functional Theory," *Chem. Mater.*, vol. 22, pp. 3762-3767, 2010/06/22 2010.

[18] M. K. Wong, F. Liu, C. S. Kam, T. L. Leung, H. W. Tam, A. B. Djurišić, *et al.*, "Synthesis of Lead-Free Perovskite Films by Combinatorial Evaporation: Fast Processes for Screening Different Precursor Combinations," *Chem. Mater.*, vol. 29, pp. 9946-9953, 2017/12/12 2017.

[19] Y. Hu, S. Zhang, X. Miao, L. Su, F. Bai, T. Qiu, *et al.*, "Ultrathin $Cs_3Bi_2I_9$ Nanosheets as an Electronic Memory Material for Flexible Memristors," *Advanced Materials Interfaces,* vol. 4, p. 1700131, 2017.

[20] W. A. Dunlap-Shohl, I. G. Hill, Y. Yan, and D. B. Mitzi, "Photovoltaic Effect in Indium(I) Iodide Thin Films," *Chem. Mater.*, vol. 30, pp. 8226-8232, 2018/11/27 2018.

Bismuth-based Double Perovskites

To further illustrate the effect of dimensionality, we briefly studied Bi-based double perovskites for PV applications. Bismuth-based halide double perovskite was first reported by Slavney, *et al.* [1] using a combination of Ag^{+} and Bi^{3+} cations to mimic Pb^{2+} in the perovskite crystal structure. Following their lead, we studied cesium silver bismuth bromide ($Cs_2AgBiBr_6$) double perovskites as an absorber material in mesoscopic solar cell architecture. Figure A.1(a) shows the thin-films and powder XRD patterns of $Cs_2AgBiBr_6$ which show excellent agreement with the calculated XRD pattern. The thin-films of $Cs_2AgBiBr_6$ was fabricated by dissolving stoichiometric composition in DMSO, followed by conventional spin-coating and annealing at 160 ℃ inside an Ar-filled glovebox. The powders of $Cs_2AgBiBr_6$ was collected after precipitation from HBr solution having stoichiometric compositions. Figure A.1(b) shows the UV-Vis absorption spectrum of the thin-films deposited onto glass substrate. Tauc plot was used to calculate an indirect bandgap of 2.25 eV as shown in the inset.

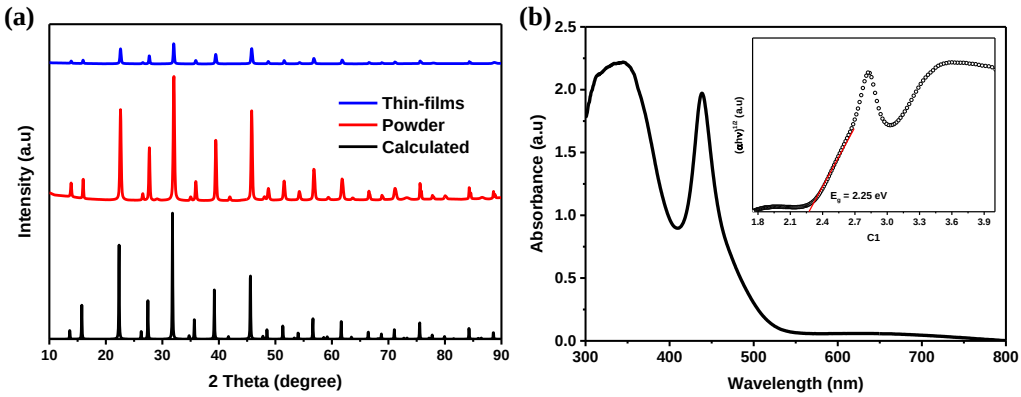

Figure A.1: Photo-physical characterizations of $Cs_2AgBiBr_6$ double perovskites. (a) XRD patterns of $Cs_2AgBiBr_6$ thin-films and powders. The bottom panel shows the calculated XRD pattern from single crystal data, (b) UV-Vis absorption spectrum of $Cs_2AgBiBr_6$ thin-films. Inset: Tauc plot showing bandgap assuming indirect bandgap.

To assess the photovoltaic performance of $Cs_2AgBiBr_6$, we fabricated solar cell devices based on mesoscopic architecture as follows: FTO/c-TiO_2/mp-TiO_2/$Cs_2AgBiBr_6$/Spiro-OMeTAD/Au. Figure A.2 shows the *J-V* responses of $Cs_2AgBiBr_6$-based solar cell measured under 1 sun illumination. Despite having a large optical bandgap, the solar cells showed excellent PCE as compared to our earlier results with $Cs_3Bi_2I_9$. The increase in photocurrent in $Cs_2AgBiBr_6$-based solar cells, even having a larger indirect bandgap, can be attributed to its continuous network of octahedral. The delocalization of charge carriers over many units of octahedral aids in efficient extraction and collection of the charges, which was absent in the zero-dimensional Bi-based perovskites.

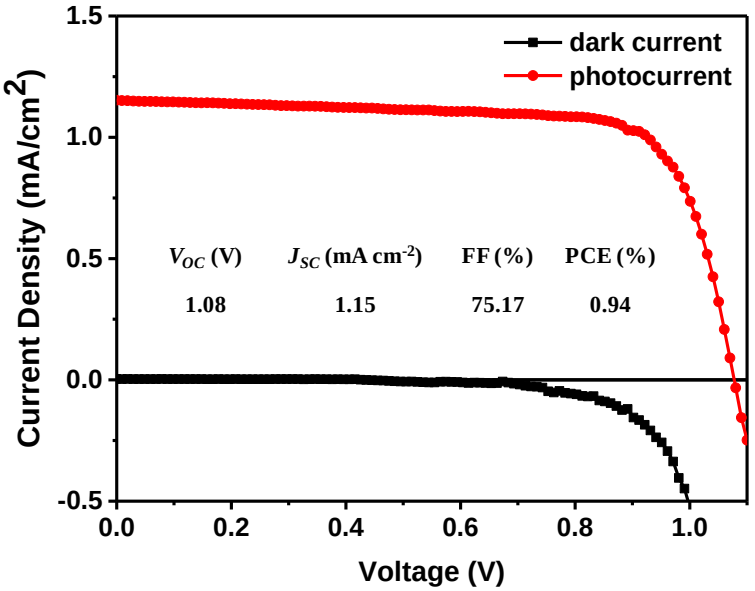

Figure A.2: *J-V* characteristics of $Cs_2AgBiBr_6$-based mesoscopic solar cells (solar cell parameters are shown in the inset).

In conclusion, the inherent charge localization due to quantum confinement effect in low-dimensional Bi-based iodide perovskites cause a major problem in achieving high PCE. Similar observations can also be made in the current literature on lead-free perovskite solar cells. To fully exploit the advantages of Bi-based halide perovskites, more emphasis should be given on the crystal structure engineering. One of the possible paths would be doping with isostructural elements to stabilize the order-disordered crystal structure (rocksalt).

References

[1] A. H. Slavney, T. Hu, A. M. Lindenberg, and H. I. Karunadasa, "A Bismuth-Halide Double Perovskite with Long Carrier Recombination Lifetime for Photovoltaic Applications," *J. Am. Chem. Soc.*, vol. 138, pp. 2138-2141, 2016/02/24 2016.